

RDTE PROJECT NO.
TECOM PROJECT NO. 8-CO-210-049244
DPG REPORT NO. DPG/JCP-97/016

**SURFACE EFFECTS ON EVAPORATION, RECIRCULATION,
AND DISPERSION IN LIGHT WINDS**

Prepared by

Christopher A. Biltoft

**Meteorology & Obscurants Division
West Desert Test Center
U.S. Army Dugway Proving Ground**

September 1997

Project Manager: Bruce Grim

Requirement: AR-191 (DO49)

19971217 085

JOINT CONTACT POINT PROGRAM MANAGEMENT OFFICE

WEST DESERT TEST CENTER

U.S. Army Dugway Proving Ground, Utah 84022-5000

DISTRIBUTION STATEMENT A

**Approved for public release;
Distribution Unlimited**

UNCLASSIFIED

Disposition Instructions

Destroy this report when no longer needed. Do not return it to the originator.

Disclaimer Statement

The views, opinions, and findings in this report are those of the author and should not be construed as an official Department of the Army position unless so designated by other official documentation.

Trade Name Statement

The use of trade names in this report does not constitute an official endorsement of the use of such commercial hardware or software. This report may not be cited for purposes of advertisement.

REPORT DOCUMENTATION PAGE			Form Approved OMB No. 0704-0188	
Public reporting burden for this collection of information is estimated to average 1 hour per response, including the time for reviewing instructions, searching existing data sources, gathering and maintaining the data needed, and completing and reviewing the collection of information. Send comments regarding this burden estimate or any other aspect of the collection of information, including suggestions for reducing this burden, to Washington Headquarters Services, Directorate for Information Operations and Reports, 1215 Jefferson Davis Highway, Suite 1204, Arlington, VA 22202-4302, and to the Office of Management and Budget, Paperwork Reduction Project (0704-0122), Washington, D.C. 20503.				
1. AGENCY USE ONLY (Leave blank)		2. REPORT DATE August 1997		3. REPORT TYPE AND DATES COVERED Final Report Final (July 1995 - August 1997)
4. TITLE AND SUBTITLE SURFACE EFFECTS ON EVAPORATION, RECIRCULATION, AND DISPERSION IN LIGHT WINDS			5. FUNDING NUMBERS 8-CO-210-049-244/K4	
6. AUTHOR(S) Christopher A. Biltoft				
7. PERFORMING ORGANIZATION NAME(S) AND ADDRESS(ES) Meteorology & Obscurants Division West Desert Test Center U.S. Army Dugway Proving Ground Dugway, UT 84022-5000			8. PERFORMING ORGANIZATION REPORT NUMBER DPG-TR-97-065	
9. SPONSORING/MONITORING AGENCY NAME(S) AND ADDRESS(ES) Joint Contact Point Division West Desert Test Center U.S. Army Dugway Proving Ground Dugway, UT 84022-5000			10. SPONSORING/MONITORING AGENCY REPORT NUMBER	
11. SUPPLEMENTARY NOTES				
12a. DISTRIBUTION/AVAILABILITY STATEMENT Distribution Unlimited			12b. DISTRIBUTION CODE	
13. ABSTRACT (Maximum 200 words) A joint U.S., UK, and Canadian Evaporation, Recirculation, and Dispersion in Light Winds trials program was conducted at U.S. Army Dugway Proving Ground in July-August 1995. Program objectives were to: (1) obtain evaporation data from chemical agent simulants on sand, concrete, and aluminum surfaces; (2) document the effects of obstacle geometry and atmospheric stability on the accumulation and retention of material entrained into obstacle wakes; and (3) examine near-surface dispersion in low winds. The program produced data sets that can be used to validate evaporation and urban dispersion models, and provided detailed descriptions of dispersion in low winds. Based on an analysis of the data, new turbulence and stability indices are proposed to characterize surface layer dispersion.				
14. SUBJECT TERMS evaporation, recirculation region, wake effects, sonic anemometer, hot-wire anemometer, boundary layer, atmospheric dispersion, diffusion, stability index, atmospheric turbulence			15. NUMBER OF PAGES	
			16. PRICE CODE	
17. SECURITY CLASSIFICATION OF REPORT UNCLASSIFIED	18. SECURITY CLASSIFICATION OF THIS PAGE UNCLASSIFIED	19. SECURITY CLASSIFICATION OF ABSTRACT UNCLASSIFIED	20. LIMITATION OF ABSTRACT UL	

FOREWORD

This report describes work accomplished under TECOM Project No. 8-CO-210-049-244 for the Joint Chemical/Biological Contact Point and Test (Project DO-49), which is managed and executed by the Joint Contact Point, U.S. Army Dugway Proving Ground, Dugway, Utah. The evaporation and recirculation field test program was a tripartite effort with active participation by the British Chemical/Biological Defence Establishment (CBDE), Porton Down, England; the Canadian Defence Research Establishment Suffield (DRES); and West Desert Test Center (WDTC), U.S. Army Dugway Proving Ground (DPG). CBDE participants included Dr. Christopher Jones and CBDE contractors Dr. Ian Roberts, Mr. Wilfred Evans, and Mr. Ilias Mavoritis. Dr. Eugene Yee led the DRES team consisting of contractors Mr. Geoff Chandler and Mr. Ray Chan. DPG participants included Christopher Biltuft (Test Director), Mr. Frederick Baney, Mr. Jimmy Calhoun, Mr. William Grayson, and Ms. Georgia Stewart of the WDTC Meteorology & Obscurants Division and Mr. David Petrie and Mr. Jim Yale of the WDTC Test Operations Division. Mr. Robert Feldman assisted with the preparation of figures and tabular data, and Mrs. Susan Gross provided word processing support.

ACKNOWLEDGEMENTS

The author thanks Dr. Eugene Yee, Dr. Joseph Klewicki, and Mr. James Bowers for the many helpful suggestions presented during their reviews of this report. Special thanks goes to Mrs. Susan Gross for skillfully and patiently preparing the many drafts and final report manuscript.

TABLE OF CONTENTS

	<u>PAGE</u>
FOREWORD	i
ACKNOWLEDGEMENTS	ii
LIST OF FIGURES	iv
LIST OF TABLES	vi
EXECUTIVE SUMMARY	vii
SECTION 1. INTRODUCTION	1
SECTION 2. THE EVAPORATION AND RECIRCULATION MEASUREMENT PROGRAM .	3
SECTION 3. ATMOSPHERIC BOUNDARY LAYER DYNAMICS	13
SECTION 4. WALL REGION STUDIES	27
SECTION 5. PLUME PROFILES AND TURBULENCE EFFECTS	35
SECTION 6. CONCLUSIONS AND RECOMMENDATIONS	61
SECTION 7. APPENDICES	A-1
A. Consolidated TIP-SJ and Micrometeorological Data	A-1
B. References	B-1
C. List of Symbols	C-1

LIST OF FIGURES

<u>FIGURE</u>		<u>PAGE</u>
1	Map of Dugway Proving Ground showing the locations of the Tower Grid and Photo Pad 11 test sites	viii
2	Schematic of the annular ring and experimental set-up used in the Evaporation Trails (from Roberts, 1996)	5
3	(a) Plan view of Recirculation Subtest source, UVICs, and 2-m cube with cube orientations of 0° (face-on, solid line) and 45° (side-on, dashed line). (b) Side view of Recirculation Subtest source, UVICs, and 2-m cube with cube orientation of 0° (following Higson, 1995).	9
4	Plan view of source and detector configuration for Experimental Session UTM ₆ conducted on 7 August 1995 with the source positioned at a height of 1.0 m in the center rear of the 2-m cube and an array of UVICs stationed within the accumulation region in the wake of the cube. (b) Side view of configuration for Experimental Session UTM	10
5	Averaged concentration time series from UVICs stationed in a crosswind array 1.5 m downwind of the 2-m cube during Trial UTE02 illustrating exponential decay following gas switch off at 1063 s into the trial sequence (from Mavoridis, 1996)	11
6	Schematic illustration of ABL evolution during a diurnal cycle over high desert terrain	14
7	Plan view schematic of the SLTEST site experimental setup, including the polyethylene slab, smoke generation system, and stand supporting the hot-wire probes and camer (from Klewicki, et al., 1995)	28
8	Vertical profiles of inner-normalized streamwise velocity statistics: (a) mean velocity, with Coles law (solid line) and upper and lower limits suggested by Blackwelder and Haritonidis (1983) (dotted lines); (b) velocity rms, with open symbols denoting results from Klewicki and Falco (1990); (c) skewness, with open symbols denoting results from Klewicki (1989); (d) kurtosis, with open symbols denoting results from Klewicki (1989) (from Metzger and Klewicki, 1996)	30
9	Plan view diagram of the 2-m cube in its face-on (solid line) and side-on (dashed line) positions with respect to the mean wind, and hot-wire probe positions	33

LIST OF FIGURES (Cont'd)

<u>FIGURE</u>		<u>PAGE</u>
10	Wake profiles of mean (a) and rms (b) axial velocities at indicated normalized spanwise (y/h) distances with cube in face-on (runs 1-6) and side-on (runs 7 and 8) orientations (from Metzger and Klewicki, 1996)	34
11	The propylene disseminator and tower-mounted sampling array (not to scale)	37
12	Vertical velocity spectra measured at the 3-m level for four successive time periods (A: 0545-0557; B: 0645-0711; C: 0745-0815; D: 0845-0917) during the transition through sunrise on 22 July 1995	46
13	Covariance quadrant analysis categories	47
14	Horizontal (u and v) 1.5-m wind components, the 3.0-m vertical wind component (w), and the 3.0-m speed of sound (c) for two successive 10-min periods illustrating quiescent conditions followed by a turbulence burst during Trial P142154	53
15	Horizontal (u and v) 1.5-m wind components, the 3.0-m vertical (w) wind component, and the 3.0-m speed of sound (c) for two successive 10-min periods illustrating fully developed nocturnal turbulence followed by a turbulence burst during Trial P150010	55
16	Vertical profiles of the probability density function $f(\chi/C)$ versus χ/C obtained from: (a) Trial P070435; (b) Trial P030745. (PDF plots provided by Dr. Eugene Yee, DRES)	57
17	Vertical profiles of the normalized probability density function $f(\chi/C)$ versus χ/C obtained from: (a) Trial P142154; (b) Trial P150010	60

LIST OF TABLES

<u>TABLE</u>		<u>PAGE</u>
1	Evaporation Site Trial Summary	4
2	Recirculation Region Subtest Trial Summary	11
3	Plume Profile Subtest Trial Summaries	36
4	Plume Profile Subtest Trial Micrometeorological Summaries . .	41
5	Cospectra, Quadrature, Phase, and Coherence for 1.5-m u and T Components During Transition Through Sunrise at Tower Grid, 22 July 1995 (35-min average, time in MDT)	44
6	Micrometeorological Summaries for Selected 10-min Time Blocks During the Morning Transition from Stable to Unstable Condi- tions	50
7	Micrometeorological Summaries for Selected 10-min Time Blocks During a Nocturnal Quiescent Period (2142205), a Turbulence Burst (2142215), Active Mechanical Turbulence (2150013), and a Turbulence Burst (2150023)	50
8	Micrometeorological Summaries for Selected 10-min Time Blocks Within Trials P030743, P070435, P142154, and P150010	59

EXECUTIVE SUMMARY

A series of open-air dispersion experiments known collectively as the Evaporation, Recirculation, and Dispersion in Light Winds trials was conducted at U.S. Army Dugway Proving Ground (DPG) in July-August 1995. The participants were scientists representing the British Chemical/Biological Defence Establishment (CBDE); the Canadian Defence Research Establishment Suffield (DRES); U.S. Army DPG West Desert Test Center (WDTC); and a consortium from the University of Utah, University of Maryland, and Michigan State University. These researchers examined several aspects of surface effects on the dispersion of windborne material within the lower portion of the atmospheric boundary layer. The objectives of the three main experimental subtests were to: (1) obtain evaporation data from neat and thickened methyl salicylate (MES) and diethyl malonate (DEM) droplets deposited on sand, concrete, and aluminum surfaces; (2) document the effects of atmospheric stability and obstacle geometry on the accumulation and dissipation of material entrained into the recirculation region within the wake of a 2-m cube; and (3) examine near-surface turbulence and its effects on dispersing plumes during low wind speed conditions. Additional methodology studies were performed to determine the efficacy of using fast-response hot-wire anemometry to measure the turbulent wind field, including turbulence production and dissipation, around obstacles and in the viscous sublayer immediately adjacent to the earth's surface. Significant results were obtained from all of the subtests and methodology studies.

The Evaporation, Recirculation, and Dispersion in Light Winds trials series was a continuation of a tripartite (U.S., U.K., and Canada) concentration fluctuation test series designed to improve our understanding of atmospheric dispersion processes. As noted above, this field test consisted of three subtests and two methodology studies. The Evaporation, Recirculation, and Plume Profile and Turbulence Effects Subtests were conducted at the DPG Tower Grid test site. The methodology studies were conducted at Tower Grid and a remote test site adjacent to the Goodyear Road causeway, which crosses the salt flats of the Great Salt Lake Desert. Figure 1 shows the locations of test sites on a DPG map. The data from the Evaporation and Recirculation Subtests were analyzed by CBDE contractors who have documented the results in reports to CBDE and a doctoral thesis. The methodology study results have been documented in University of Utah technical reports, open literature publications, and a doctoral thesis. The principal focus of this report is on the Plume Profile and Turbulence Effects Subtest, which studied near-surface plume dispersion under non-steady flow in light winds.

Table 1 in Section 2 summarizes the trials conducted during the Evaporation Subtest. Of the 34 successful trials of 30- to 120-min duration, 12 used MES as the simulant and 22 used DEM. The subtest objective, which was to document the effects of droplet size, thickener content, simulant type, surface type, and meteorological conditions on droplet evaporation rate, was met. Data from these trials in combination with data from earlier work have been used to validate a comprehensive evaporation model, satisfying a knowledge shortfall identified by Technical Panel 9 of The Technical Cooperation Program (TTCP) Subgroup E on Chemical/Biological (CB) Defense. Detailed results are provided by Roberts (1996).

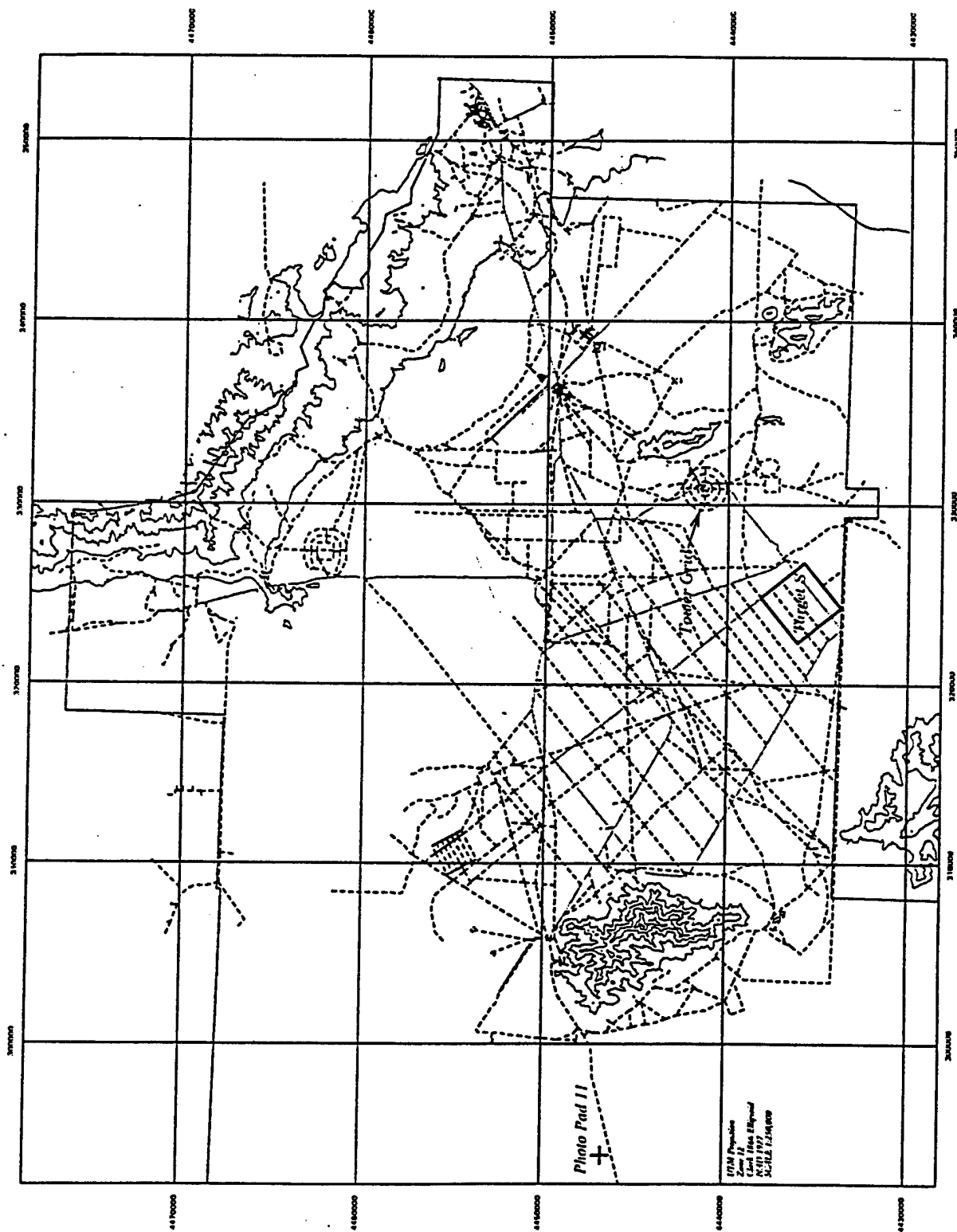


Figure 1. Map of Dugway Proving Ground showing the locations of the Tower Grid and Photo Pad 11 test sites.

Table 2 in Section 2 summarizes the 89 trials of the Recirculation Region Subtest. Forty-nine of these trials, which were typically 2 to 5 min in duration, were performed with a cube orientation of 0° (cube face normal to the wind) and 44 were performed with a cube orientation of 45°. Data acquired during the trials included infrared (IR) imagery of tracer gas (propylene) dispersion around the cube and hot-wire anemometer measurements of winds and turbulence within the cube's wake. The subtest objective, which was to document obstacle geometry and atmospheric stability effects on the retention of windborne material entrained into the accumulation region in the wake of a bluff object, was met. Flow around bluff bodies during stable atmospheric conditions produces large wakes that retain high concentrations of windborne contaminants. However, when these results are normalized by wake width and wind speed, atmospheric stability appears to have a minimal effect on contaminant residence time. Recirculation trials results are being used to develop and validate urban dispersion model algorithms. Detailed analyses of obstacle wake entrainment results are given by Mavoridis (1996, 1997).

The university consortium conducted several methodology studies using hot-wire anemometry. One study, which supported the Recirculation Region Subtest, involved turbulence measurements within the wake of the 2-m cube. This study was only partly successful because dust accumulated on the hot-wire sensor elements. The second methodology study, which investigated stability and Reynolds number effects on flow within the near-surface wall region, was performed on the salt flats immediately north of the Causeway near Photo Pad 11. Steady wind conditions and the absence of micrometer-scale windborne dust particles made high quality near-surface hot-wire anemometry possible at this location. These studies included wind velocity profile measurements around a small (0.25-m) cube and near-surface turbulence, vorticity, and stress measurements. The resulting data document surface (near-wall) effects on turbulence and momentum profiles, fluxes, and turbulent kinetic energy generation and dissipation in high Reynolds number flows and provide a database for development of near-surface high Reynolds number flow models.

The Plume Profile and Turbulence Effects Subtest was designed to provide information on the effects of near-surface turbulence on the vertical component of plume dispersion during non-steady flow in light winds. During this subtest, propylene was continuously released for periods of 15 to 35 min at heights ranging from 0.05 to 2.5 m above ground level (AGL). A vertical array of gas concentration detectors was positioned 12.5 to 100 m downwind of the source to provide detailed vertical plume concentration profile measurements. Concentration detector availability limited the vertical array to a single tower fully instrumented from 0.25 to 8.0 m. Sonic anemometer/thermometers (sonics) also mounted on this tower provided wind and turbulence measurements.

Wind meander wafted the disseminated propylene plume intermittently across the detectors during the Plume Profile and Turbulence Effects Subtest. The quantity of nonzero plume concentration measurements varied inversely with the amount of meander experienced during each trial. Of the 24 trials, 15 provided sufficient propylene concentration data to form vertical concentration profiles, six of which supported detailed statistical analyses. The

plume vertical profile and accompanying micrometeorological data provide detailed information on near-surface dispersion during light winds.

The Plume Profile and Turbulence Effects Subtest led to the development of two new indices, the Diabatic Ratio (DR) and the Total Diabatic Influence (TDI). DR represents the ratio of convectively-driven to shear-driven turbulence, and TDI is a measure of turbulence strength. Both indices are needed to describe the turbulent state of the atmosphere: DR defines whether turbulence is primarily convective or shear-driven, while TDI defines its magnitude. These indices were developed as alternatives to existing similarity-based indices to better represent the state of the atmosphere within the first few meters of the surface where the preponderance of troop exposure to windborne hazards occurs. When applied to realistic non-steady atmospheric conditions such as light winds punctuated by turbulence bursts and transition through sunrise, these indices appear to characterize the state of the surface layer better than the widely used similarity theory indices. DR and TDI also can be easily calculated in near real-time using the output of a two-axis sonic anemometer/thermometer. If these new indices are proven useful in further testing, they could find wide application in the modeling of windborne hazards.

SECTION 1. INTRODUCTION

The Surface Effects on Evaporation, Recirculation, and Dispersion in Light Winds project was designed to address issues related to troop vulnerability to high concentrations of hazardous windborne materials. The principal focus of this report is on the effects of surface characteristics (e.g., wakes, porosity, surface heating, and turbulence) on the concentrations of material dispersing near the surface during light wind conditions. Near-surface effects are important because the majority of troop exposures to hazardous materials occur within a few meters of the surface. Field measurements are needed to define these effects because near-surface velocity gradients are too strong and turbulence scales are too small for present direct numerical or large eddy simulations. Surface effects are a significant operational concern to the military because high concentrations of hazardous materials can occur near the surface, particularly during light wind situations when the turbulence driving the dispersion process is weak. A major goal of this work is to improve our understanding of near-surface dispersion, which should lead to improved hazard scenario modeling and better design and deployment of windborne hazard monitoring equipment (e.g., chemical and biological agent detectors).

The Surface Effects on Evaporation, Recirculation, and Dispersion in Light Winds experiment series was a tripartite effort with participation by the British Chemical/Biological Defence Establishment-Porton (CBDE), the Canadian Defence Research Establishment Suffield (DRES), and U.S. Army Dugway Proving Ground (DPG). Each participating nation contributed unique capabilities to address multiple aspects of near-surface dispersion. The principal CBDE focus was on evaporation and bluff body recirculation region studies, while DRES performed detailed near-surface concentration profile measurements. DPG was responsible for test program management and meteorological and infrared (IR) imagery support. A DPG contractor, the University of Utah Department of Mechanical Engineering, provided the hot-wire anemometer measurements needed to characterize near-surface velocity and turbulence profiles.

The Evaporation, Recirculation, and Dispersion trials were conducted at two locations, one near Tower Grid (40° 06'N, 112° 58'W) and one near Photo Pad 11 on the salt flats immediately north of Goodyear Road (40° 08'N, 113° 26'W). Tower Grid is typical of high desert terrain, with long periods of light winds persisting through the evening and early morning hours. The terrain is characterized by a gently sloping clay surface with a light cover of short, brushy vegetation. Drainage flows make Tower Grid a suitable location for dispersion and evaporation tests as long as measurements are not required immediately above the dusty clay surface. In contrast to the aerodynamically rough Tower Grid location, the salt crust surface on the Great Salt Lake Desert forms an aerodynamically smooth surface virtually devoid of vegetation. Velocity and turbulence profile measurements very close to the surface are more successful on the salt flats because the salt crust is free of the fine clay particles that interfere with the calibration of the fine heated wires used as sensing elements for hot-wire anemometers.

The desert floor forms an impenetrable "no-slip" boundary underlying the atmospheric boundary layer (ABL), the portion of the troposphere sufficiently

close to the earth that it responds to surface forcings. This surface is a momentum sink, a heat source during the day, and a heat sink at night. Because the constantly varying fluxes of heat and momentum keep ABL flow in a continuous state of evolution, a "steady state" condition that can be adequately treated using standard statistical methodologies is the exception rather than the rule. The structure of the ABL can be divided into an outer region, an inertial sublayer, and a near-wall region. Each region or sublayer has unique characteristics that can be described in terms of relevant scaling variables. The focus of this report is on the inertial sublayer, which encompasses the first few tens of meters above the surface, and the near-wall region, which lies within a few tens of centimeters of the surface.

The state of the ABL is usually described in terms of similarity theory relationships, with Monin-Obukhov scaling applied to the surface layer, while mixed layer or convective scaling is used when convection is present. These semi-empirical relationships are based on an apparent behavioral dependence of boundary layer characteristics on scaling variables that include the vertical fluxes of heat and momentum. Because a flux describes the passage of a quantity (heat, momentum) through a surface, it should be representative of an area. In contrast, surface-based measurements used to calculate fluxes are usually made at a point in space, which renders vertical flux calculations highly susceptible to non-stationary flows over inhomogeneous surfaces. This problem is particularly prevalent close to the surface where strong gradients and constantly changing fluxes of heat and momentum occur. Thus, while many authors (for example, Deardorff, 1985; Venkatram, 1988) have successfully applied similarity scaling at "smoke stack" heights of 10 to 100 m and through the convection-dominated boundary layer, no comparably successful methodology has emerged for the light winds and variable conditions that frequently occur at "nose height" (within 2 m) of the surface.

Persistent weak winds within the inertial sublayer present a dispersion modeling challenge because some of the greatest hazards for windborne releases of toxic materials occur during light winds when mixing is weak or intermittent and flow patterns are variable. High concentrations of toxic materials can also persist for long periods or accumulate in the wakes of obstacles under these conditions in complex terrain. Variable light winds are most common during near-surface nocturnal drainage flows, but can also extend through sunrise transition into periods of daytime convection. This report examines the limitations of present theory and presents some practical alternatives for describing the state of the inertial sublayer during variable light wind episodes.

The near-wall region of the ABL has received little attention by the meteorological community in part because of the difficulty of obtaining measurements close to the earth's surface. However, ABL turbulence is intimately coupled with surface heat and momentum fluxes. Also, fine-scale processes such as evaporation, deposition, resuspension, and the destruction of concentration gradients occur as a consequence of near-wall turbulence generation and dissipation. This report describes flow and turbulence measurements within the near-wall region and the use of the resulting data to verify near-surface physical models.

SECTION 2. THE EVAPORATION AND RECIRCULATION MEASUREMENT PROGRAM

2.1 THE EVAPORATION SUBTEST

The Evaporation Subtest was undertaken to provide a validation data base for a mass transfer model for predicting the evaporation of chemical agent droplets from various surfaces (Roberts, 1994). This model considers the effects on droplet evaporation of surface roughness, molecular diffusion within the wall region adjacent to the surface, and atmospheric stability. The development and validation of this model helps to fill a modeling shortfall identified by an expert panel of Technical Panel 9 of The Technical Cooperation Program (TTCP) Subgroup E on Chemical/Biological (CB) Defense.

The need for a new evaporation model was driven by the unsatisfactory performance of existing models. Roberts (1994) reports that available droplet evaporation results can be reproduced with existing models only through the use of unrealistic spread factors, wind velocity adjustments, and/or absorption or diffusion conditions because the model physics is inadequate. Evaporation model development has been stymied by incomplete characterization of the absorption and evaporation processes, including the lack of an adequate model of near-surface turbulence.

The specific objectives of the Evaporation Subtest were to: (a) quantify spread factors and evaporation rates for droplets deposited on various surfaces, and (b) obtain a better understanding of the relative importance of various physical factors (droplet size, surface porosity, simulant type, and thickener content) on these variables. The surfaces chosen for the trials were sand, concrete, and aluminum plate, which respectively represented porous, semi-porous, and non-porous substrates. Diethyl Malonate (DEM, a simulant for the chemical agent GD) and Methyl Salicylate (MES, a simulant for the chemical agent HD) were the selected simulants. Polymethylmethacrylate powder (co-polymer K-125) served as the thickener. The mean droplet size varied from 1.0 to 3.6 mm, depending on thickener content.

The evaporation trials were conducted at the DPG Tower Grid test site between 17 July and 11 August 1995. The site, 30 m south of the Tower Grid Command Post (CP) Building, consisted of a concrete annular ring "sidewalk" of 6-m radius and 1-m width located on flat, open terrain characterized by a surface roughness length z_0 of 1.6 cm. The interior of the annulus was filled with sand, and aluminum plates ringed its outside edge. The purpose of the annular ring design was to ensure uniform exposure of detectors stationed at the annulus centroid to the evaporated vapors from droplets deposited in a uniform pattern around the ring. Ultraviolet ion collectors were placed at the annulus center at heights of 5, 15, 30, 50, and 80 cm above ground level (AGL) to measure these evaporated vapors. Ancillary measurements obtained near the evaporation site included surface and air temperature profiles. A sonic anemometer/thermometer (sonic) mounted at 2 m AGL measured wind and turbulence. A schematic of the annular ring and experimental set-up is shown in Figure 2.

DEM or MES admixed with 0, 3, or 5 percent by weight of co-polymer K125 thickener were deposited in the trials series summarized in Table 1. The

Table 1. Evaporation Site Trial Summary.*

Trial No.	Date Day/Mo/Year	Duration (min)	Droplet Diameter (mm)	Liquid Type	Liquid Loading ^b (mg m ⁻¹)	Thickener (%)	Surface Type
u01	21/7/95	60	3.6	DEM	3358	0	concrete
u02	21/7/95	60	3.6	DEM	7750	0	concrete
u03	22/7/95	90	3.6	DEM	7750	0	concrete
u04	22/7/95	90	0.2-2.0	DEM	9376	3	concrete
u05	24/7/95	60	0.2-2.0	DEM	9055	3	aluminium
u06	24/7/95	45	0.2-2.0	DEM	6781	5	aluminium
u07	24/7/95	30	3.6	DEM	4421	0	aluminium
u08	24/7/95	30	3.6	DEM	4421	0	aluminium
u09	24/7/95	30	0.2-2.0	DEM	6781	5	aluminium
u10	24/7/95	30	0.2-2.0	DEM	7127	3	aluminium
u11	25/7/95	60	3.6	DEM	7233	0	concrete
u12	25/7/95	90	0.2-2.0	DEM	9035	3	concrete
u14	25/7/95	60	3.6	DEM	6006	0	concrete
u15	26/7/95	90	0.2-2.0	DEM	8261	3	sand
u16	26/7/95	60	0.2-2.0	DEM	4721	5	sand
u18	28/7/95	60	0.2-2.0	DEM	6119	3	sand
u19	28/7/95	60	0.2-2.0	DEM	5993	5	sand
u20	28/7/95	60	3.6	DEM	7327	0	sand
u22	29/7/95	90	0.2-2.0	DEM	5071	5	concrete
u23	29/7/95	60	0.2-2.0	DEM	5178	3	concrete
u24	29/7/95	60	0.2-2.0	DEM	5993	5	sand
u25	29/7/95	60	0.2-2.0	DEM	6884	3	sand
u26	01/8/95	90	0.2-2.0	MES	4734	3	concrete
u27	01/8/95	120	0.2-2.0	MES	4636	5	concrete
u28	01/8/95	90	3.6	MES	6928	0	concrete
u30	02/8/95	60	0.2-2.0	MES	5680	3	sand
u31	02/8/95	75	0.2-2.0	MES	6823	5	sand
u32	03/8/95	75	0.2-2.0	MES	5679	3	aluminium
u35	03/8/95	60	0.2-2.0	MES	8036	5	aluminium
u36	04/8/95	90	3.6	MES	5298	0	aluminium
u37	04/8/95	90	3.6	MES	9211	0	sand
u38	04/8/95	60	0.2-2.0	MES	10061	3	sand
u39	04/8/95	45	0.2-2.0	MES	7883	5	sand
u40	04/8/95	45	0.2-2.0	MES	6509	3	concrete

* From Roberts (1996).

^b Liquid loading is the neat chemical loading per unit length of annulus.

droplet deposition was fixed at 10 g/m^2 , with droplet diameters ranging from 0.2 to 2 mm (mean of 1.0 mm) for thickened mixtures and 3.6 mm for neat mixtures. The micro-pipette that deposited the neat simulant droplets provided greater droplet size control than the rotating-disk droplet sprayer used with the thickened mixture. A uniform evaporating (curved) line source was formed by depositing a continuous swath of droplets at a fixed rate along the arc, which provided uninterrupted detector exposure to a uniform evaporating source even with changes in wind direction. A video recorder provided time-lapsed images of deposited droplet samples as they soaked into and/or evaporated from their underlying surfaces.

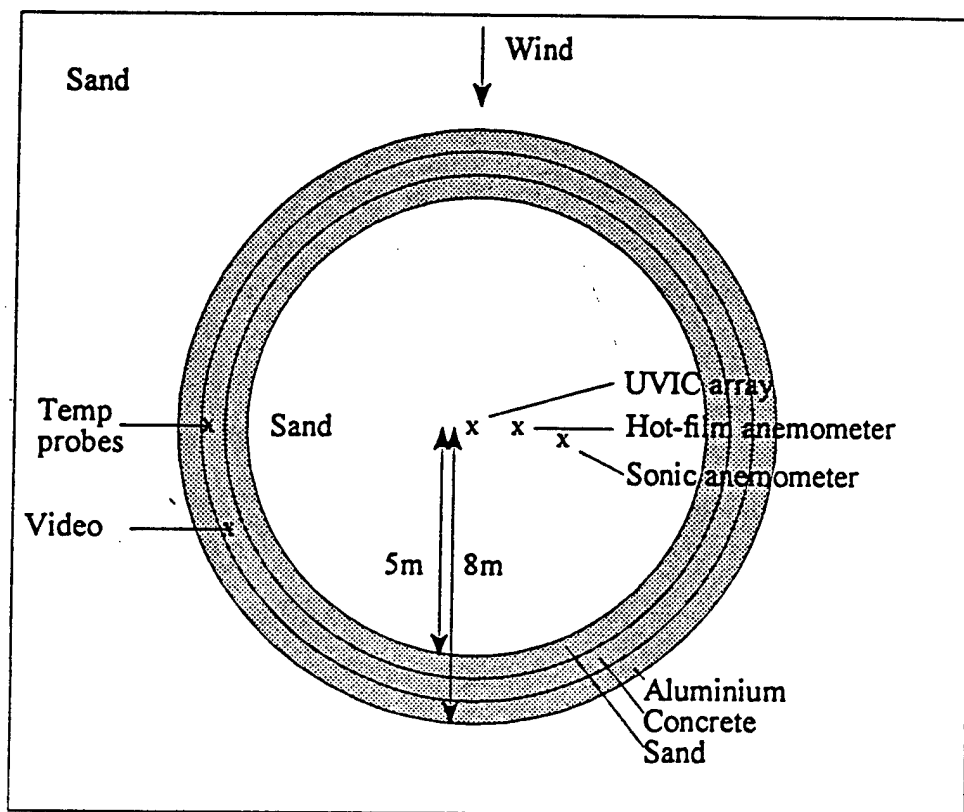


Figure 2. Schematic of the annular ring and experimental set-up used in the Evaporation Trials (from Roberts, 1996).

The concentrations of the evaporating simulants were measured by CBDE's Ultraviolet Ion Collector (UVIC) photo-ionization detectors (PIDs). As part of data analysis, the UVIC voltage readings were converted to simulant concentrations in parts per million (ppm) and the horizontal vapor flux was calculated for each trial. The vapor flux was computed by integrating the product of concentration and wind speed over the plume depth using a power-law wind profile fitted to the measured wind speeds and a reflected Gaussian distribution fitted to the measured simulant concentrations. This vapor flux represented the mass release rate per unit line source length of the evaporating droplets. Assuming that individual droplets contribute equally to the total amount of evaporating material, the calculated flux and known number of individual droplets per unit length of line source define the droplet evaporation for each trial. These calculated evaporation rates were also correlated with time-lapse droplet size video imagery.

The quality of the evaporation data was evaluated by comparing the mass of simulant initially deposited on the aluminum surfaces to the vapor mass measured throughout each trial. The average recovery for drops deposited on the aluminum surface was 96 percent, with a standard deviation of 15 percent. Roberts (1996) believes that similar recovery rates were achieved for drops deposited on the sand and concrete surfaces. The major source of uncertainty occurred toward the end of each test when the vapor concentrations were very low.

Roberts (1996) compares the Evaporation Subtest evaporation data to the predictions of the Roberts (1994) model and finds that the model reasonably replicates the early stages of evaporation, correctly distinguishing the effects of thickener and surface porosity on evaporation rates. There is a close (within ± 10 percent) correspondence between predictions and measurements in the early stages of evaporation, with perhaps a slight early stage underprediction of evaporation on concrete surfaces. However, the model tends to overpredict the evaporation rate in the later stages of evaporation regardless of the surface type or thickener content. Roberts (1996) believes that the later stages of evaporation are governed by transport processes within the surface substrate (such as capillarity, diffusion, and gravitational flow), and that the physics of these processes is not well specified. More detailed models and measurement techniques are needed to resolve this issue.

The Evaporation Subtest results also provided an opportunity to quantify droplet spread in terms of a spread factor, the ratio of the wet spot diameter on the surface to the droplet diameter prior to impact. Droplet images prior to and after impact were obtained using a video camera. Unfortunately, poor contrast over the aluminum surface precluded differentiating wet spots on that surface. However, Roberts (1996) was able to achieve the required video image pairs over sand and concrete. He reports a spread factor of 2.5 on sand regardless of droplet size or viscosity. In contrast, viscosity and droplet size appear to affect droplet size on concrete. A rough estimate of the spread factor on concrete is $0.6d + 2.5$, where d is the droplet diameter in millimeters.

2.2 THE RECIRCULATION SUBTEST

Flow around a large obstacle forms a horizontally-oriented "horseshoe" vortex that begins upwind of the obstacle front and wraps around the sides, trailing into the wake. This horseshoe vortex mixes windborne contaminants rapidly to the ground, distributing them around the obstacle and into a recirculating "accumulation region." Contaminant concentration within the accumulation region varies as a function of wake dimensions, wind speed, turbulence intensity, and the magnitude and duration of the contaminant concentration impinging upon the obstacle. Gaussian dispersion models do not presently include methodologies to account for the accumulation, retention, and dissipation of contaminants trapped within the wakes of large obstacles. To address this deficiency, Mavoridis (1996, 1997) performed a series of wind tunnel experiments and field trials, including the Recirculation Subtest. The principal purpose of the Recirculation Subtest was to investigate source geometry and atmospheric stability effects on the accumulation and dissipation of a windborne tracer (propylene) in the accumulation region within the wake of a 2-m plywood cube.

The Recirculation Subtest was conducted at the DPG Tower Grid test site between 22 July and 8 August 1995. Trials were conducted on flat, open terrain characterized by low brush and a surface roughness length of 1.6 cm. The test site was approximately 800 m south of the Evaporation Subtest site. This separation was sufficient to preclude the possibility that tracer materials released at one site would contaminate measurements made at the other.

Each Recirculation Subtest trial began with the positioning of the disseminator 4 or 5 m upwind of the cube at a height of 1 or 2 m AGL. As shown in Figure 3, the cube, which was mounted on a central pivot, could be rotated to present either a "face-on" (0° orientation) or "corner-on" (45° orientation) front to the mean wind direction. UVICs were stationed in the wake of the cube at a height of 1 m to obtain time-resolved measurements of propylene concentration. Table 2 summarizes the Recirculation Subtest trials. The last trial set, designated UTM₆ in Table 2, is distinguished by the location of the source 0.5 m behind the cube as shown in Figure 4. This configuration produced reference maximum concentrations within the accumulation region.

A recirculation trial could only be accomplished while the tracer source remained aligned upwind of the cube front. Thus, trial conduct required careful monitoring of the meandering winds. Once the wind direction came into alignment, the disseminator was turned on to begin a trial. The UVICs were then switched on to sample the propylene concentrations within the accumulation region. As this propylene concentration reached its upper plateau, the disseminator was abruptly shut off. The UVICs then measured the propylene concentration decay within the accumulation region. The multiple trials conducted within experimental sessions included several source distances, source heights, and cube orientations.

The recirculation region propylene concentration measurements were supplemented by sonic anemometer readings obtained from a CBDE-furnished tripod-

mounted sonic positioned upwind of the cube at a height of 2-m AGL. The sonic provided mean wind and turbulence statistics and the fluxes of heat and momentum required for determination of the Obukhov length L . Recirculation Subtest micrometeorological summaries are provided by Mavoridis (1996, 1997).

A total of 89 trials of 2- to 5-min duration were completed during the Recirculation Subtest. Concentration data from UVICs stationed in the cube wake were used to estimate the accumulation region residence time t_a , which is defined by Mavoridis (1996) as the time required for the accumulation region concentration to decay to $1/e$ (37 percent) of its original value. The trial results indicate that accumulation region evacuation proceeds exponentially, as predicted by Hunt and Castro (1994). Figure 5 illustrates an averaged recirculation region time series with this characteristic exponential decay rate.

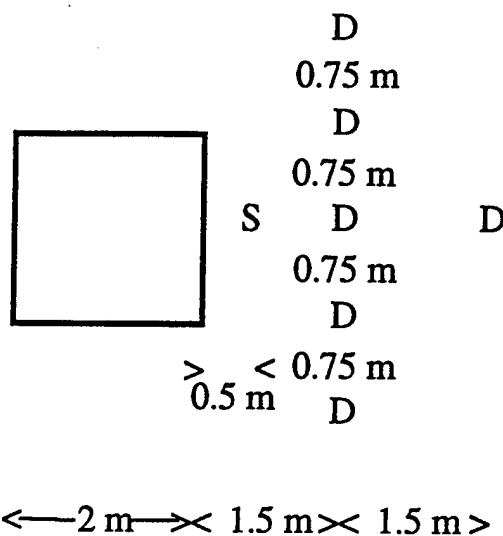
The Recirculation Subtest residence time t_a results, when normalized by the cube dimension h and mean flow u around the cube, were initially found to be inconsistent with results presented by Fackrell (1984), particularly when the cube was in a side-on orientation with respect to the wind direction. However, the hot-wire anemometer measurements described by Metzger and Klewicki (1996, see also Section 4 of this report) showed that the side-on cube orientation produced a larger wake width h' than the face-on orientation. When Mavoridis (1996) defined a non-dimensional residence time t_r as

$$t_r = t_a u / h' . \quad (2-1)$$

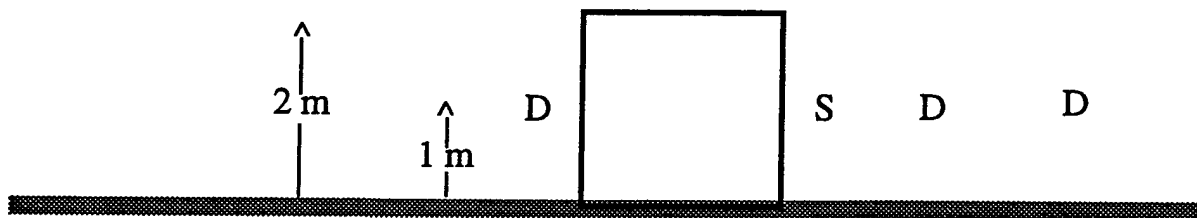
he was able to achieve results consistent with Fackrell (1984). Thus, h' appears to be a more relevant dimension than h for wake accumulation modeling.

Flow around the cube during stable atmospheric conditions produced larger wakes, higher accumulation region concentrations, and longer t_a than corresponding measurements taken when the atmosphere was unstable. However, the magnitude of t_r varied little with stability, indicating that u and h' accounted for most of the variability observed in t_a . Mavoridis (1996) concludes that stability effects are implicitly accounted for in suitably normalized accumulation region residence times.

(a)



(b)



10

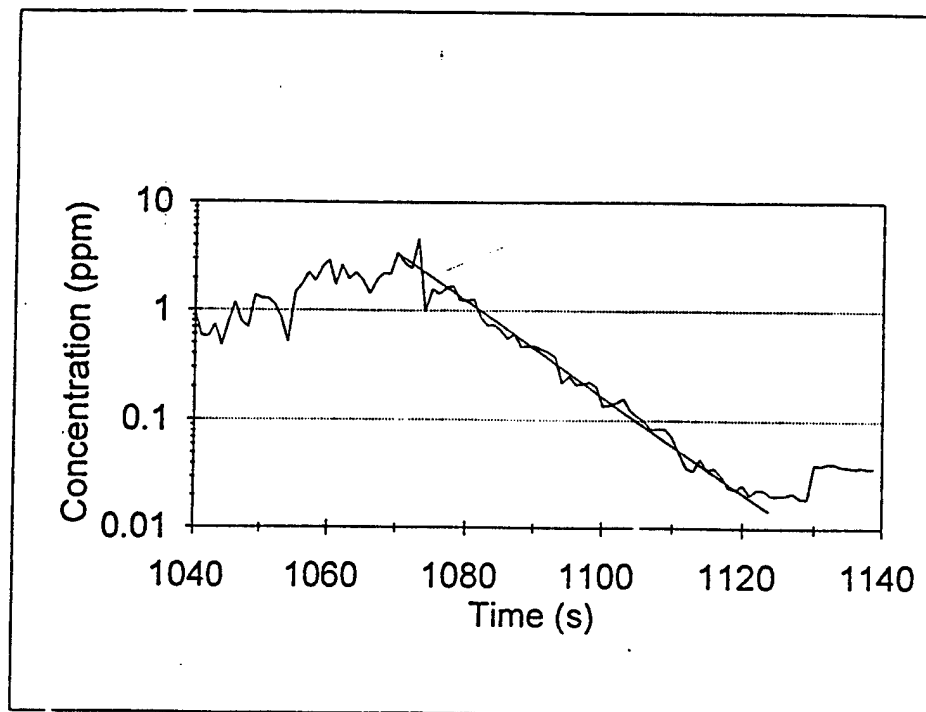


Figure 5. Averaged concentration time series from UVICs stationed in a cross-wind array 1.5 m downwind of the 2-m cube during Trial UTE02, illustrating exponential decay following gas switch off at 1063 s into the trial sequence (from Mavoridis, 1996).

Table 2. Recirculation Subtest Trial Summary.

Experimental Session (day/month)	Number of Trials	Time of Day	Cube Orientation (deg)	Source Distance (m)	Source Height (m)
UTB (22/7)	2	Daytime	0	5 upwind	2
UTC (24/7)	5	Daytime	0	5 upwind	2
UTD (25/7)	8	Daytime	0	5 upwind	2
UTE (27/7)	5	Nighttime	0	5 upwind	2
UTF (28/8)	11	Nighttime	0	5 upwind	2
UTG (29/7)	6	Daytime	45	5 upwind	2
UTH (31/7)	5	Daytime	45	5 upwind	2
UTJ (2/8)	11	Nighttime	45	5 upwind	2
UTK (3/8)	11	Nighttime	45	5 upwind	2
UTL (4/8)	14	Daytime	0	4 upwind	1
UTM _a (7/8)	5	Daytime	45	4 upwind	1
UTM _b (7/8)	6	Daytime	0	rear face	1

Blank Page

SECTION 3. ATMOSPHERIC BOUNDARY LAYER DYNAMICS

3.1 BOUNDARY LAYER THEORY AND PRACTICES

The atmospheric boundary layer (ABL) is the portion of the atmosphere characterized by the high Reynolds number flows that are produced by the diurnal heat flux cycle and other forcings originating at the earth's surface. The ABL is generally more complex than "engineering" boundary layers (found in pipe, channel, and wind tunnel flows) because it contains continuously varying heat fluxes, temperature and velocity gradients, directional shear and divergence fields, and complex surface roughness features. Perhaps the ABL's major distinguishing feature is that it is in a constant state of change, continuously adjusting to varying fluxes of heat and momentum. Also, the spatial and temporal scales parameterized by the Reynolds number relevant to ABL flow are often several orders of magnitude greater than comparable scales found in other boundary layer flows. ABL theory is further complicated by the lack of a unified treatment; the outer region and inertial sublayer are typically studied by meteorologists interested in atmospheric transport and diffusion, while the wall region remains the domain of mechanical engineers who are principally interested in momentum and turbulence exchange in highly sheared flows and viscous effects on near-surface interactions. This section summarizes salient features of existing boundary layer theories and practices, followed by a discussion of their limitations under non-steady (variable) light wind conditions.

Figure 6 is a schematic illustration of the ABL evolution during a diurnal cycle over high desert terrain. The principal ABL regions are depicted as they evolve in space and time. Wavy lines at region boundaries represent fluctuations in boundary heights due to perturbations such as gravity waves and convection. The principal ABL scaling variables (defined later in this section) are shown in brackets. The dashed and dotted lines denote boundaries between stable, unstable, and free convection zones. The depth and duration of the various regions and layers depicted in Figure 6 vary with factors such as heat flux, surface roughness, and the pressure-driven velocity field.

The state of the ABL is too complex and poorly understood to be derived from first principles. Consequently, current ABL theory is based on empirical relationships and Reynolds approximations to the Navier-Stokes equations that allow the use of certain similarity theory "scaling variables" to describe salient characteristics of the ABL. Pertinent scaling variables can be formed into dimensionless parameters that merge scattered data into "self-similar" forms (universal curves, functions, or constants) that depict ABL attributes. The principal scaling variables and dimensionless parameters for the outer region, inertial sublayer, and wall region are described below using the usual micrometeorological Cartesian convention in which downwind and crosswind direction distances are represented respectively by x and y , with z depicting height above ground level. Wind velocity components in the alongwind, crosswind, and vertical directions are represented by u , v , and w , respectively.

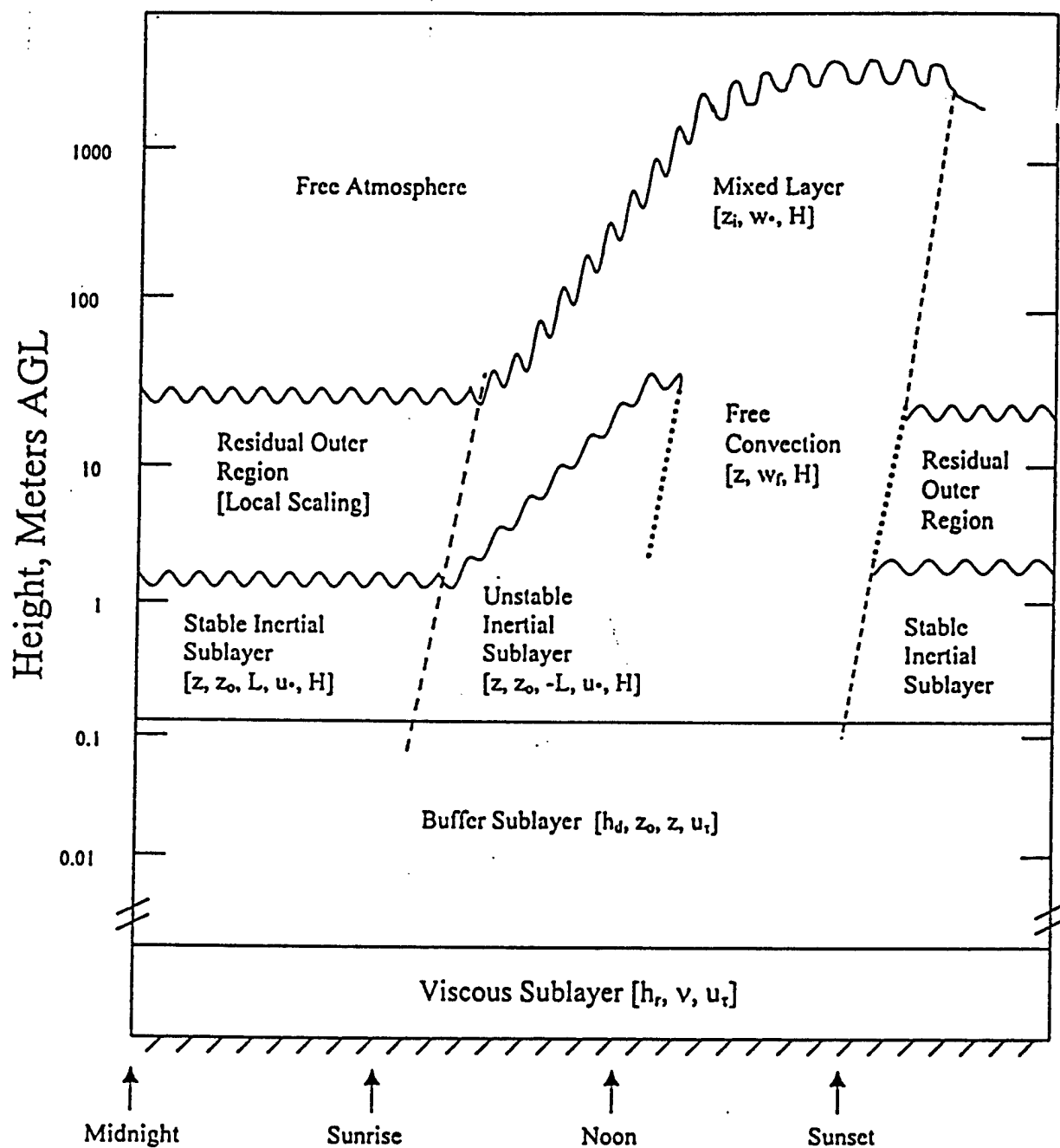


Figure 6. Schematic illustration of ABL evolution during a diurnal cycle over high desert terrain. The principal ABL scaling variables are shown in brackets. Dashes and asterisks denote boundaries between stable, unstable, and free convection zones.

Boundary layer theory is developed under the following assumptions: (1) flow can be represented as a 2-dimensional velocity field with a uniform mean vertical gradient; (2) velocity, temperature, and pressure fluctuations are statistically homogeneous; (3) all statistical quantities for meteorological variables are stationary with respect to time; and (4) viscous dissipation outside the wall region is small. The stationarity assumption, wherein all of the $\partial/\partial t$ terms of the following equations are zero, is particularly problematic in a boundary layer characterized by constant change. Given these assumptions and neglecting terms higher than second order, simplified Reynolds approximations for turbulent shear stress ($-\overline{u'w'}$) and vertical heat flux ($\overline{w'T'}$) budgets are given respectively by (Garratt, 1992)

$$\partial \overline{u'w'}/\partial t = -\overline{w'^2} \partial u/\partial z - \partial \overline{u'w'^2}/\partial z + (g/T) \overline{u'T'} - \rho^{-1} (\overline{u' \partial P'/\partial z} + \overline{w' \partial P'/\partial x}) \quad (3-1)$$

and

$$\partial \overline{w'T'}/\partial t = -\overline{w'^2} \partial \theta/\partial z - \partial \overline{w'^2 T'}/\partial z + (g/T) \overline{T'^2} - \rho^{-1} (\overline{T' \partial P'/\partial z}) \quad (3-2)$$

where θ is the potential temperature, g is gravitational acceleration, T is absolute temperature, [1] is a shear ($\partial u/\partial z$) or stratification ($\partial \theta/\partial z$) production term, [2] is the vertical turbulent flux divergence of $\overline{u'w'}$ or $\overline{w'T'}$, [3] represents buoyancy production (conversion of turbulent kinetic energy to turbulent potential energy), and [4] is a pressure interaction term which tends to dissipate shear stress and heat flux. Overbars and primes denote time averages and departures therefrom, respectively. Applying similar treatment to the three velocity variance components produces the turbulent kinetic energy $\overline{q^2} = (\overline{u'^2} + \overline{v'^2} + \overline{w'^2})/2$. The resulting conservation equation is

$$\partial \overline{q^2}/\partial t = -\overline{u'w'} \partial \overline{u}/\partial z + (g/T) \overline{w'T'} - \partial (\overline{w'q^2} + \overline{w'P'}/\rho) / \partial z - \epsilon \quad (3-3)$$

where [1] represents shear production, [2] depicts buoyant production or dissipation, [3] consists of vertical turbulent energy transport and pressure-velocity correlation terms, and [4] is the turbulent kinetic energy dissipation term ϵ . Most scaling variables and parameters used to describe the state of the ABL relate to the production, flux divergence, and buoyancy terms of Equations (3-1) through (3-3).

3.2 THE OUTER REGION

The outer region is the upper portion of the ABL. Its top extends from a few tens of meters AGL during quiescent nocturnal conditions to several kilometers AGL during strong convection. Horizontal winds in the outer region respond principally to the interaction of pressure gradient and Coriolis forces, with the surface influence mainly expressed as convection initiated by surface heating. Exchange between the outer region and other regions within

the ABL continues so long as convection is sufficiently vigorous to distribute heat, momentum, and other dispersing scalar quantities between the surface and the top of the mixed layer. The top of the mixed layer z_i is usually defined by a capping inversion. The presence of convective mixing is the principal feature that distinguishes the outer region from the free atmosphere above it. Wind velocity profiles within the outer region are independent of surface-based wind shear.

The outer region expands during the day as the heat flux H from the earth's surface produces convective motions that raise the capping inversion. The sign and magnitude of H is related to the vertical velocity-temperature covariance $\overline{w'T'}$ by

$$H = \rho C_p \overline{w'T'}, \quad (3-4)$$

where ρ is atmospheric density and C_p is the specific heat of air at constant pressure. A positive $\overline{w'T'}$ indicates an upward flux of heat from the surface. When a sufficient positive heat flux is present to maintain convection, the outer region becomes a convection-dominated "mixed layer." Mixed layer similarity relationships, which have fairly uniform vertical velocity variance profiles and minimal surface drag effects, predominate between about $0.1z_i$ and $0.8z_i$.

Heat flux and z_i are the most important scaling variables for the ABL outer region. They can be combined to form the convective velocity scale

$$w_* = \left[\frac{gz_i H}{\rho C_p T} \right]^{1/3}, \quad (3-5)$$

which characterizes the mixed layer state of the outer region. The convective velocity scale is typically zero at sunrise, increases rapidly to a mid-afternoon maximum between 1.5 and 3.0 m/s, and decreases toward zero in the evening (Stull, 1988, Figure 4.1). The significance of w_* is its relevance to the scaling of outer region velocity variables. For example, the vertical velocity variance $\overline{w'^2}$ is a measure of the vigor with which vertical mixing occurs within the ABL. Although direct measurements of $\overline{w'^2}$ in the outer region are rarely available, the convective contributions to $\overline{w'^2}$ normalized by w_*^2 fall onto a universal curve of height z normalized by z_i according to the expression (Stull, 1988)

$$\frac{\overline{w'^2}}{w_*^2} = 1.8 \left(\frac{z}{z_i} \right)^{2/3} \left[1 - 0.8 \left(\frac{z}{z_i} \right) \right]^2. \quad (3-6)$$

Thus, if z_i and $\overline{w'T'}$ are known, Equation (3-6) provides an analytical expression for the vertical variation of $\overline{w'^2}$ in the convective ABL.

When the ratio of the mean wind speed U to the convective velocity scale w_* falls within the range $2 < U/w_* < 10$, dispersion within the upper regions of the ABL can be parameterized using mixed-layer scaling. The time scale for large convective eddies is z_i/w_* , and the "travel time" for dispersing material is rendered dimensionless through multiplication by w_*/z_i . For long range dispersion, downwind travel distance x from a dissemination position scales with the product of w_*/z_i and x/U , forming a dimensionless downwind distance (Deardorff, 1985)

$$X = \frac{x w_*}{U z_i} \quad (3-7)$$

When plotted against X , plume dispersion within the convective ABL exhibits consistent universal behaviors. For example, laboratory and field studies (Kaimal et al., 1986) indicate that the centroid of dispersing material released at the surface into a convective ABL tends to rise within $X < 1.0$ of the release point, reaching a height of $0.8z/z_i$ between $1.0 < X < 2.0$. It then gradually descends toward $0.5 z/z_i$ at $X > 3.0$, becoming well mixed at greater downwind distances.

In the absence of convection, the boundary layer depth is sustained only by mechanical turbulence generated by flow over roughness elements. As surface heating and convection subside in the evening, the outer region collapses into layers isolated from each other by temperature inversions. The nocturnal mixing height is within the lowest of these inversions. Shear layers develop when turbulent mixing becomes weak. Above the nocturnal mixing height, the atmosphere slumps into a "residual layer" (Stull, 1988) characterized by multiple shear zones and inversions which sandwich layers of air that are decoupled from the surface, each other, and the free atmosphere above them. Local similarity (Wyngaard, 1973) is dominant within each residual layer. Diffusing material released within one of these layers can travel a considerable distance without mixing into the layer above or below it.

3.3 THE INERTIAL SUBLAYER

Between the convection-dominated mixed layer and the viscosity-dominated wall region lies the inertial sublayer. This layer, also known as the surface layer or the constant flux layer, is typically a few meters to a few tens of meters in depth. The inertial sublayer depth is the closest analog to the thickness of a laboratory boundary layer because it is the depth through which surface-generated shear forces affect flow within the ABL.

The inertial sublayer is so named because it supports an inertial subrange, a band of turbulent eddy scales ranging from the integral scale λ_i to the Taylor microscale λ_T . The inertial subrange includes eddy scales small enough to decay isotropically, distributing energy evenly in all dimensions, but large enough to be unaffected by viscosity. Consequently, inertial subrange eddy motions are the same order of magnitude in all directions.

The integral scale defines eddies on the large end of the inertial subrange. These eddies, with a characteristic length of tens to hundreds of

meters, extract kinetic energy from the mean flow. They contain the greatest turbulent kinetic energy and are believed to be primarily responsible for the turbulent mixing of diffusing material. The breakup of integral scale-sized eddies initiates a transfer of turbulent energy down the range of eddy scales until they are dissipated in molecular motions as heat.

Integral scale length depends on factors such as distance from the surface and atmospheric stability. A first approximation of λ_i is given by Prandtl's hypothesized characteristic eddy length scale of kz (Schlichting, 1979), where k is the von Karman constant (0.4 ± 0.02) and z is height AGL. The largest integral scales are associated with convective eddies in the upper part of the inertial sublayer.

Near the lower end of the inertial subrange lies the Taylor microscale, where eddies are small enough (on the order of centimeters) to be affected by viscosity. The Taylor microscale is defined in terms of q^2 , ϵ , and kinematic viscosity ν as

$$\lambda_T = (\nu q^2 / \epsilon)^{1/2} . \quad (3-8)$$

A continuous cascade of energy occurs between λ_i and λ_T as large eddies break up and distribute their energy isotropically over progressively smaller scales. Scales smaller than λ_T form a gradual transition from the inertial subrange to the dissipation subrange, where viscous effects predominate and the destruction of concentration gradients by molecular diffusion occurs. Similarity arguments work well in the inertial sublayer when a stationary inertial subrange extends between the integral scale and Taylor microscale.

The inertial sublayer is most often characterized using Monin-Obukhov similarity theory, which assumes that the average values of buoyancy and the fluxes of heat and momentum are constant. The principal Monin-Obukhov variables are the heat flux H , roughness length z_0 , friction velocity u_* , height z , and ratio of gravitational acceleration to absolute temperature g/T . The effects of surface roughness are parameterized by z_0 . Roughness length accounts for the effects of surface texture and roughness element spacing on the inertial sublayer wind profile. The friction velocity, which is the square root of the vertical momentum flux

$$u_* = \sqrt{-u'w'} , \quad (3-9)$$

is the most important Monin-Obukhov velocity scale.

The Obukhov length L , formed from the ratio of the buoyancy and shear-driven contributions to turbulent kinetic energy (terms [1] and [2] in Equation (3-3)), is the principal Monin-Obukhov length scale. The ratio of z to L forms the nondimensional stability parameter

The magnitude of z/L is determined primarily by the ratio of heat and momentum fluxes, while heat flux determines the sign of z/L .

$$\frac{z}{L} = \frac{-kgzH}{\rho C_p T u_*^3} \quad (3-10)$$

Monin-Obukhov similarity theory describes inertial sublayer mean flow properties as functions only of z/L . For $-z/L < 1$, inertial sublayer velocity fluctuations are on the order of u_* (typically 0.1 to 1.0 m/s) and the wind velocity increases linearly with the logarithm of height normalized by z_0 . The normalized wind speed profile is expressed as

$$\frac{u}{u_*} = \left(\frac{1}{k} \right) \left[\ln \left(\frac{z}{z_0} + \psi_m \right) \right], \quad (3-11)$$

where ψ_m is a z/L -dependent diabatic influence function. Equation (3-11) remains valid through the inertial sublayer and into the wall region until the flow is severely distorted by near-surface viscous effects.

Another useful Monin-Obukhov relationship is the ratio of the vertical velocity standard deviation σ_w to u_* . The average σ_w normalized by u_* is nearly constant, exhibiting a weak z/L dependence that becomes important only in the presence of strong convection. The normalized mean σ_w profile is given by

$$\frac{\overline{\sigma_w}}{u_*} \approx 1.3 + f(z/L) \quad (3-12)$$

It must be emphasized that Equation (3-12) represents an average condition and that any single realization of the σ_w/u_* ratio can exhibit a deviation of ± 50 percent or more due primarily to the inherent temporal variability of $\overline{-u'w'}$. An analysis performed by Wyngaard (1973) concludes that $\overline{-u'w'}$ requires sampling periods 10 to 100 times longer than those for the vertical velocity variance to achieve comparable levels of statistical stability. Consequently, Equation (3-12) is an attractive alternative to the eddy correlation method for the calculation of u_* .

The dimensionless ratio of height (either z or z_i) to L is widely used as a measure of the state of the ABL and its capacity for dispersion. When heat flux is weak, L increases towards infinity and the atmosphere approaches an adiabatic stratification in which there is no net gain or loss in buoyancy as air parcels rise or sink. Motions in an adiabatic ABL are shear-driven, being neither enhanced by convection nor suppressed by density stratification. Turbulent energy in an adiabatic atmosphere is extracted from large scale motions during flow over roughness elements. Diabatic conditions exist when the heat flux is nonzero; the magnitude of L decreases in proportion to the magnitude of H . Upward heat flux produces a negative L associated with convection-enhanced dispersion. Downward-directed heat flux produces a positive L with damped (negatively-buoyant) turbulent motions and suppressed vertical dispersion. Wyngaard and Cote' (1971) suggest that the removal of energy by damping in the stable surface layer is locally compensated by

turbulent energy generated near the surface and imported into the inertial sublayer by the turbulence transport term [3] in Equation (3-3). Conversely, the turbulence transport term transports energy toward the surface during convection.

A positive (upward) heat flux in the inertial sublayer quickly grows through the outer layer, simultaneously diminishing $-L$ and increasing z_i . Deardorff (1972) defines a $-z_i/L$ of 4.5 as the point of transition between a shear-driven ABL and a convection-driven one in which an outer region mixed layer overlies a convectively unstable inertial sublayer. When the heat flux is sufficiently strong to diminish z/L to -1 , u' and w' become decorrelated and u vanishes in free convection. Dispersing material released into free convection typically detaches quickly from the surface and diffuses aloft in vigorous mixing. A free convection velocity scale w_f , analogous to the mixed layer convective velocity scale w , is the pertinent velocity scale in an inertial sublayer dominated by free convection. Holtslag and Nieuwstadt (1986) define w_f as

$$w_f = \left[\frac{gZH}{\rho C_p T} \right]^{1/3} \quad (3-13)$$

Turbulent motions originating in the free convection layer blend seamlessly into the mixed layer above it.

Parameters independent of Monin-Obukhov similarity also describe the state of the inertial sublayer. These parameters are typically formed from ratios of fluxes, velocity and temperature variances (σ_u^2 , σ_w^2 , σ_T^2), and gradients of velocity ($\partial u/\partial z$) and potential temperature ($\partial \theta/\partial z$). The most important of these non-similarity parameters include the Flux Richardson number, eddy viscosity, turbulent thermal diffusivity, and velocity and temperature correlation terms. The Flux Richardson Number R_F , the ratio of turbulent energy production by density variations to turbulent energy production by mean shear, is given by (Tavoularis and Corrsin, 1981)

$$R_F = \left(\frac{g}{T} \right) \frac{\overline{-w'T'}}{\overline{-u'w'} \partial u / \partial z} \quad (3-14)$$

The turbulent or eddy viscosity, which represents the strength of turbulent diffusion by inertial subrange-scale eddies, is given by

$$\nu_\tau = \frac{\overline{-u'w'}}{\partial u / \partial z} \quad (3-15)$$

The most significant terms from the thermal diffusivity tensor are D_{21} and D_{22} , which represent the important horizontal and vertical components of turbulent thermal diffusivity. These are given by

$$D_{21} = \frac{\overline{-u'\theta'}}{d\theta/dz} \quad (3-16a)$$

$$D_{22} = \frac{\overline{-w'\theta'}}{d\theta/dz} \quad (3-16b)$$

The velocity and temperature correlation terms, which describe the efficiency with which the vertical exchanges of heat and momentum take place, are

$$C_{wT} = \frac{\overline{w'T'}}{\sigma_w \sigma_T} \quad (3-17a)$$

$$C_{uw} = \frac{\overline{u'w'}}{\sigma_u \sigma_w} \quad (3-17b)$$

$$C_{uT} = \frac{\overline{u'T'}}{\sigma_u \sigma_T} \quad (3-17c)$$

Neither Monin-Obukhov similarity theory nor the alternative parameterizations work well outside a limited range of conditions. In particular, the strongly stable ABL lacks a fully developed inertial subrange link between large-scale energetic motions and the Taylor microscale λ_T . Thus, the cascade of energy down the eddy scale range is interrupted in the strongly stable ABL. A critical flux Richardson number defines the conditions under which negative buoyancy is sufficient to break the inertial subrange link. When $R_f > 0.2$ there is insufficient turbulence to maintain a continuous transfer of heat and momentum, and the ABL separates into strata isolated from each other by shear zones and inversions. As this occurs, z ceases to be a relevant scaling variable and a state of "z-less stratification" (Wyngaard, 1973) arises. This condition, with vertical mixing confined to sporadic turbulence bursts, prevails near the surface during nights with light and variable winds. In quiescent periods between turbulence bursts, diffusing material released into a strongly stable layer can slump to the surface if it is sufficiently dense, or persist at high concentrations confined within the layer into which it is released.

While similarity theory descriptions of the strongly stable ABL have long been recognized as problematic, it is increasingly evident that Monin-Obukhov similarity theory assumptions are also violated during periods with the non-steady conditions associated with light winds regardless of stability. Light winds produce great uncertainty in flux computations. For example, Biltoft (1993) encountered near-zero or counter-gradient momentum fluxes near the surface during the sunrise transition and into the initial development of

convection. When $\overline{u'w'}$ is zero or positive, u cannot be computed. The problems in using eddy correlation measurements of $\overline{u'w'}$ to estimate u , were first recognized by Busch and Panofsky (1968). They consider eddy correlation determinations of $\overline{u'w'}$ to be unreliable when u is less than 0.32 m/s, a value that is rarely reached with light winds. A basic problem with both $\overline{u'w'}$ and $\overline{w'T'}$ is that they are the algebraic sums of positive and negative contributions which, in many circumstances, substantially cancel. Thus, these fluxes can be small compared to their uncertainties or to the magnitudes of natural variations arising from the lack of homogeneity and stationarity. Because the magnitude and sign of L are largely determined by the ratio of u^3 to $\overline{w'T'}$, uncertainties in the computation or estimation of those variables translate directly into uncertainties in L .

The familiar ABL parameterizations not associated with Monin-Obukhov similarity theory are also of limited use during periods with non-steady conditions. For example, velocity gradients in a real ABL can diminish to zero and change sign, rendering the ABL parameterizations that contain them mathematically intractable. Wind azimuth and elevation angle standard deviations or variances and wind velocity component variances frequently are used as direct measures of ABL turbulence. However, because these variances are subject to trends and meander, it is possible to obtain a variance of equivalent magnitude from measurements made during periods of low wind speed with high meander and measurements made during periods of high wind speed and high turbulence even though dispersion under these two regimes will be very different. Without resorting to spectrum analysis, it is not possible to determine how much each eddy scale within the flow contributes to the total variance. Likewise, a very large temperature variance can be measured when a steep trend or abrupt temperature change occurs, even when there is little eddy thermal exchange. Filtering can limit trend and meander contributions to the variance, but the results vary as a function of the technique chosen and filter length. Of all the variances, $\overline{\sigma_w^2}$ is the most reliable turbulence indicator because it is relatively free of trends and large-scale meander. Also, the surface-layer similarity relationship between σ_w and the rate of vertical dispersion from surface or near-surface sources is well established (see, for example, Briggs, 1988; Venkatram, 1988). However, vertical velocity measurements require specialized instruments that are not widely available, and vertical motions cannot be unambiguously defined in uneven or sloping terrain.

The shortcomings of the existing inertial sublayer scaling variables and their derived parameterizations suggest a need for more robust alternatives. Section 5 of this report includes a detailed examination of turbulence case studies obtained during light winds and proposes alternative methods for parameterizing near-surface stability and turbulence effects on diffusion.

3.4 THE WALL REGION

A transition to the wall region begins at the bottom of the inertial sublayer. The wall region is composed of a buffer sublayer and a viscous or interfacial layer immediately adjacent to the surface. Wind profiles remain

logarithmic with respect to height into the buffer sublayer, but the vertical dimensions of turbulent eddies become constrained by the proximity of the surface and are typically smaller than eddy horizontal dimensions. Also, the effects of individual roughness elements are felt within the buffer sublayer, creating very inhomogeneous turbulent flow. The roughness length z_0 typically lies within the buffer sublayer and is its principal length scale. Garratt (1994) observes that the transition into the wall region typically begins when $z < 100z_0$, reaching the lower limit of the logarithmic wind profile at approximately $10z_0$.

The transition from the inertial subregion to the buffer sublayer requires a change in scaling variables as viscosity effects become dominant while z_i and g/T cease to be relevant. Because little information exists on wall region diabatic effects, the relevance of the heat flux as a scaling variable remains largely unknown. The composition of stress also changes from Reynolds stress (u_r) to surface shear stress (u_τ), the product of the velocity gradient with the dynamic viscosity coefficient, due to the increased contribution from viscosity. The u_r/u_τ ratio approaches unity when going from the inertial sublayer through the buffer sublayer as the contributions to u_r from viscous stress compensate for the loss of Reynolds stress near the surface. Long and Chen (1981) suggest the existence of a u_r/u_τ maximum at a distance from the surface proportional to the square root of the Reynolds number, placing it near the boundary between the buffer sublayer and the inertial sublayer in atmospheric flows. Although the existence of such a maximum is not yet rigorously confirmed, its distance from the surface could become an important length scale. Dimensional quantities measured within the wall region are typically rendered nondimensional (inner-normalized) using u_τ and/or viscosity ν . The vertical distance from the surface can be represented by the non-dimensional height

$$z^+ = zu_\tau/\nu . \quad (3-18)$$

Using inner normalization, the buffer sublayer lies within $5 < z^+ < n$, where n ranges from 50 to 100. The viscous sublayer ($z^+ < 5$) forms the interface with the surface.

The viscosity of air ν at 20 °C is 0.000015 m²/s, which is four or five orders of magnitude smaller than the typical eddy viscosity ν_t in the inertial sublayer. Therefore, viscosity effects on inertial subrange-scale eddies are usually ignored outside the wall region. Garratt (1992) remarks that ν_t/ν is, like the Reynolds number, a ratio of inertial to viscous forces operating within the ABL. However, strong gradients within the wall region greatly diminish ν_t as ν becomes dominant. Thus, the inertial subrange terminates at the Taylor microscale (on the order of 0.1 m) in the buffer sublayer. The dominant eddies in the viscous sublayer are on the order of the Kolmogorov scale (0.001 m).

The buffer sublayer is close enough to the surface that flow within it experiences strong surface roughness effects, but far enough from the surface that it does not experience severe viscous retardation. Therefore, the

generation of the small scale turbulence responsible for the rapid breakdown of concentration gradients reaches its maximum in the buffer sublayer.

The viscous sublayer lies immediately above the surface. Logarithmic mean wind profiling fails in the viscous sublayer because of the effects of viscosity and the presence of extreme gradients above an impermeable surface. Motion in the viscous sublayer only occurs when the momentum is sufficient to overcome the resistance threshold of retarding viscous forces. Thus, the most prevalent motions within the viscous sublayer tend to be intermittent bursts aligned along the axial velocity.

A primary consideration for near-wall flow is whether the wall is aerodynamically rough or smooth. The aerodynamic nature of the surface is determined by surface roughness, as represented by texture or grain size (h_r) in a ratio with the surface shear stress u_τ and viscosity ν . If $u_\tau h_r / \nu > 75$, which is the usual case along the ground surface, the flow is aerodynamically rough with turbulence penetrating to the surface (Garratt, 1992). In this case, both small scale eddy motions and molecular diffusion play major roles in surface-to-air heat and momentum exchanges, driving processes such as deposition and evaporation. The Tower Grid site is aerodynamically rough, but the Salt Flats site with a grain size of 1 mm or less is aerodynamically smooth ($u_\tau h_r / \nu < 5$) under most conditions.

Models of the wall region (for example, Falco, 1991) are based on studies performed using fast-response hot-wire anemometers in shear-driven wind tunnel flows (see, Willmarth and Lu, 1972). The primary mechanism for energy exchange is the turbulent "burst" in which "streaks" of low-speed fluid near the surface are violently "ejected" into the lower part of the buffer layer, to be displaced by downward "sweeps" of higher momentum fluid. The downward moving fluid diverges into "pockets" upon contact with the surface. Pocket formation forces the surrounding low-momentum air to converge and stretch into thin, elongated "streaks" with vertical acceleration, re-initiating the ejection process. Reynolds stress formation occurs along the upstream boundaries of the ejected low speed fluid packets as they enter the buffer sublayer, mix with higher speed fluid, and turn into the direction of the mean flow. Falco (1991) also states that the sweep/ejection process is responsible for a majority of the mechanical turbulent kinetic energy production within the wall region.

The momentum deficit thickness Reynolds number R_θ describes the ratio of inertial forces contributing to turbulent motions within the ABL to retarding viscous forces. This Reynolds number is given by

$$R_\theta = U_\infty h_\theta / \nu \quad , \quad (3-19)$$

where U_∞ is the free-stream velocity at the top of the surface layer and h_θ is the momentum deficit thickness. Momentum deficit thickness is an "equivalent zero velocity distance" used as an indicator of the amount of momentum lost with respect to the free stream velocity due to the presence of the boundary layer. The momentum deficit thickness is roughly equal to one-tenth of the

shear-driven boundary layer thickness (Klewicki et al., 1995). Using this approximation, R_0 for the surface layer is on the order of 10^6 .

Blank Page

SECTION 4. WALL REGION STUDIES

4.1 TEST SITE DESCRIPTION

A series of preliminary near-surface flow studies were performed by a University Consortium (principally members of the University of Utah, University of Maryland, and Michigan State University Mechanical Engineering Departments) at DPG's Surface Layer and Environmental Sciences Test (SLTEST) site, which is 1300 m west of Photo Pad 11 and 30 m north of Goodyear Road (see Figure 1). This site on the bottom of a dry lake bed was selected for surface layer studies because of its flat, undisturbed, vegetation-free surface and an upwind fetch that is unobstructed by wake-generating obstacles for many tens of kilometers. Flow over the dry lake bed is nearly homogeneous, and the absence of wake-generating obstacles upwind of the SLTEST site minimizes terrain-induced meander experienced at more complex sites. Composed of a sand/clay/salt mixture capped by a thin salt crust, the lake bed surface has a roughness length z_0 of less than 0.001 m and is relatively free of micrometer-size dust particles which can impinge upon and alter the calibration of micrometer-scale hot-wire probes. A rise of 1 m over a distance of 10 km to the south also produces a negligible (1/10000) slope, thereby minimizing localized gravity-driven flows.

In addition to a low slope angle, minimal roughness, and steady winds, the SLTEST site is characterized by large R_θ , estimated by Metzger and Klewicki (1996) to be on the order of several million. An R_θ of this magnitude is representative of flows within the ABL. The large R_θ is principally a consequence of the large h_d (on the order of tens of meters), which is several orders of magnitude greater than the centimeter-scale boundary layers generated within typical engineering wind tunnels. Because of its smooth surface and unobstructed flow, the SLTEST site is an open air equivalent of a large wind tunnel where high R_θ flows of geophysical interest can be measured without the need for extremely high velocities or resorting to other unrealistic flow scaling criteria.

4.2 SLTEST STUDIES

The University Consortium conducted measurement campaigns at the SLTEST site on 24-26 May and 8 August 1994 and on 21 July-9 August and 13 September 1995. Five distinct sets of experiments were conducted during these campaigns: (1) viscous sublayer velocity and pressure measurements, (2) axial and vertical velocity profile and gradient measurements within the near-wall region, (3) velocity and pressure measurements around a cube, (4) flow visualization of coherent structures within the viscous sublayer, and (5) studies of near-surface turbulence generation and dissipation.

The hot-wire sensors were copper-plated tungsten wires with a total length of 3 mm and an unplated "active region" of 5- μ m diameter and 1-mm length maintained at a constant overheat ratio set between 1.3 to 1.7. Each probe consisted of one or more wires, with multi-wire probes designed to sample multiple velocity components and/or velocity gradients and vorticity. When velocity profiles were needed, the hot-wire probes were mounted on stands in "rakes" at heights ranging from 0.5 mm to 2.0 m AGL. The hot-wire systems

were operated at sampling rates varying between 500 and 10,000 Hz for trial durations of 2 to 20 min. Klewicki et al. (1995) and Folz (1997) provide a more detailed discussion of the instrumentation and data collection. On-site hot-wire calibrations were performed immediately before and after each trial using a pitot-static tube velocity standard and differential pressure transducer housed in a portable planar jet facility. The planar jet facility was built by the University of Utah Department of Mechanical Engineering specifically for operational use in the open atmosphere.

The flow visualization measurement station, which is shown in plan view in Figure 7, consisted of a polyethylene slab (1.3 x 2.0 x 0.025 m) mounted flush with the salt flat surface. The slab contained an injection slit through which theatrical fog can be disseminated to form a uniform curtain immediately above the slab surface. A video camera recorded the behavior of this thin smoke curtain while pressure measurements were taken with Larson-Davis Model 2250 0.25-in microphones embedded within the polyethylene slab. These microphones respond to pressure fluctuations at frequencies in the range of 23 Hz to 100 kHz. Thus, the flow visualization measurement station provides the capability to characterize activity within the viscous sublayer.

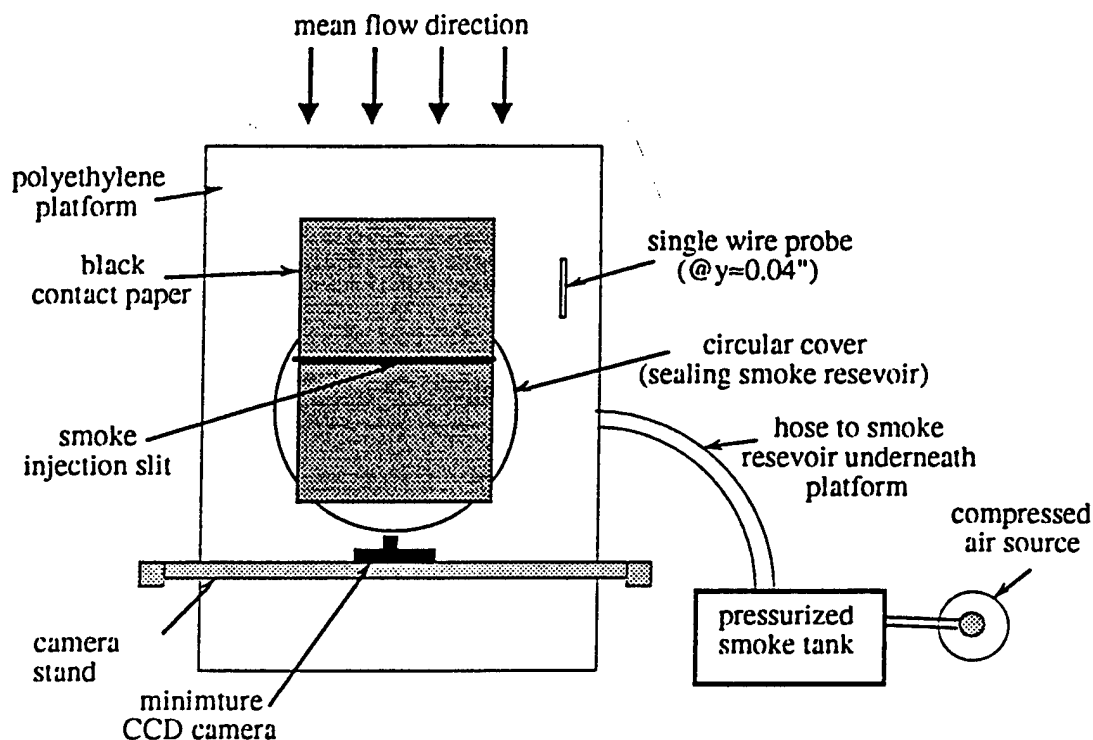


Figure 7. Plan view schematic of the SLTEST site experimental setup, including the polyethylene slab, smoke generation system, and stand supporting the hot-wire probes and camera (from Klewicki, et al., 1995).

4.3 WALL REGION TRIAL RESULTS

Direct axial velocity gradient and shear stress measurements were made by aligning hot-wire probe arrays into the mean flow direction within the viscous sublayer and buffer layer. The acquired data were compiled into statistical summaries that included trial means, root-mean-square (rms) deviations about the mean, skewness, and kurtosis. All results were presented as a function of z^* , and compared with previous results obtained in lower R_θ wind tunnel flows.

The inner-normalized mean axial velocity ($u^* = u/u_\tau$) within the viscous sublayer was found to increase linearly with height, followed by a transition to a logarithmic profile beginning at $z^* \approx 10$ (see Figure 8). Also shown in Figure 8 is a solid line representing Coles "law of the wall" for logarithmic wind profiles in the buffer sublayer, which is given by (Murlis et al., 1982) as

$$u^* = \frac{u}{u_\tau} = 5.61 \ln z^* + f(R_\theta) \quad (4-1)$$

where $f(R_\theta)$ is weakly dependent on the Reynolds number (≈ 5.0 according to Klewicki and Falco, 1990). The data from this study (Folz, 1997; Metzger and Klewicki, 1996) depart significantly from this velocity profile model, but are in reasonable agreement with the dotted lines in Figure 8, which represent the results presented by Blackwelder and Haritonidis (1983).

The rms velocity variations found within the viscous sublayer in this study are virtually equivalent to those found in previous measurements, but the buffer layer rms values (see Figure 8b), are nearly 33 percent larger than those measured previously in lower R_θ flows. Likewise, the skewness and kurtosis are proportionally larger, particularly within the viscous sublayer, than previously measured (see Figures 8c and d). Klewicki et al. (1995) postulate that the increased buffer layer rms velocity (u') may indicate an R_θ dependence in inner-normalized axial velocity rms ($u'^* = u'/u_\tau$) and/or improved probe spatial resolution and surface shear stress definition. They also suggest that the strong positive skewness in u' is a consequence of the no-slip condition existing at the surface.

Klewicki et al. (1995) describe how the ejection slit smoke curtain was used to produce visual images of "streaks" and "pockets" forming within the viscous sublayer flow. The smoke released in a continuous, uniform thin curtain at the surface quickly converged into long, stretched filaments (streaks) of low speed fluid bordered by U-shaped clear pockets of clear fluid recently swept into the viscous sublayer from above. The video records were analyzed for lateral (spanwise) streak spacing, pocket width, and time between pocket events, with the streak spacing and pocket width normalized by u_τ/ν and time normalized by u_τ^2/ν . Their results support the proposition by Smith and Metzler (1983) that the normalized spanwise streak spacing is a universal number ≈ 100 and that the spanwise pocket scale ($y^* = yu_\tau/\nu$) is related to R_θ by

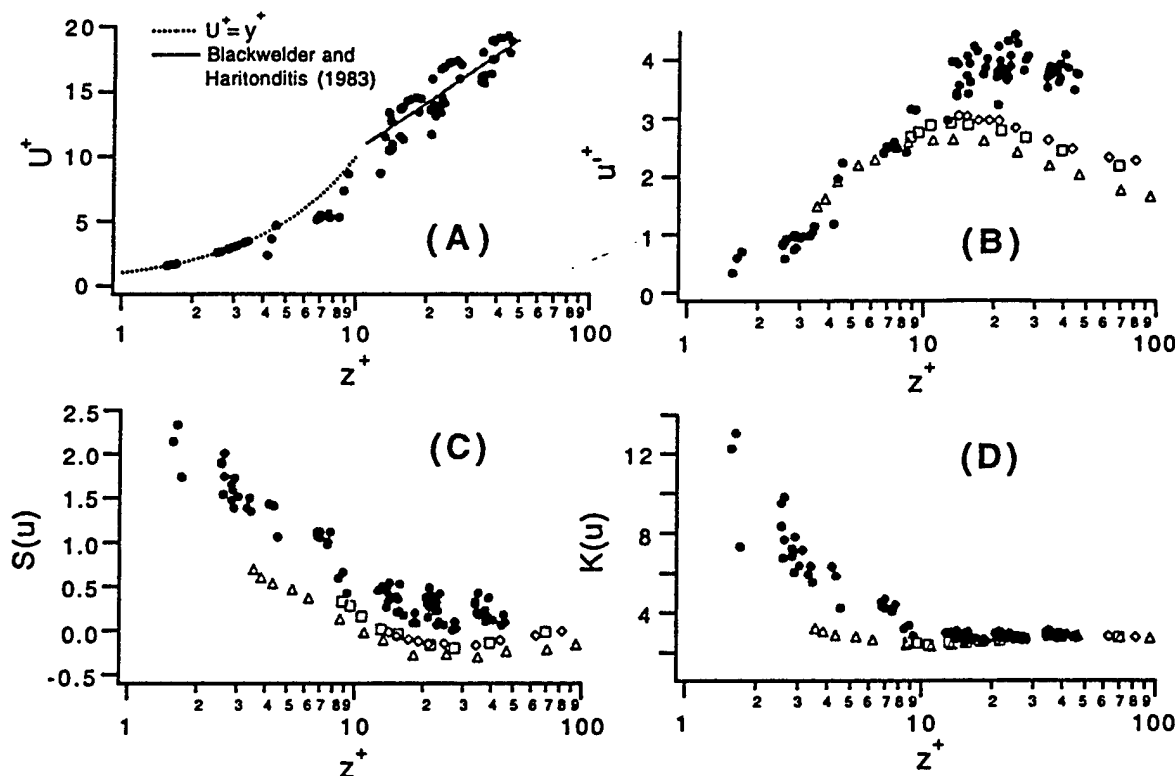


Figure 8. Vertical profiles of inner-normalized streamwise velocity statistics: (a) mean velocity, with Coles law (solid line) and upper and lower limits suggested by Blackwelder and Haritonidis (1983) (dotted lines); (b) velocity rms, with open symbols denoting results from Klewicky and Falco (1990); (c) skewness, with open symbols denoting results from Klewicky (1989); (d) kurtosis, with open symbols denoting results from Klewicky (1989) (from Metzger and Klewicky, 1996).

$$y^+ = A \log R_0 + B, \quad (4-2)$$

where A and B are constants.

Metzger and Klewicky (1996) obtained measurements of axial and vertical velocities and velocity gradients within the buffer region and the lower portion of the inertial sublayer using a six-element x-array probe. This probe was positioned successively at 0.5, 1.0, 1.5, and 2.0 m AGL, with 10-min time series collected at each level. The fast sampling rate provided sufficient data to calculate the first four statistical moments of axial and vertical velocity and their gradients. These measurements revealed several wall region characteristics: (1) an increase in velocity variances with increasing proximity to the surface, a result consistent with the Falco (1991) and Willmarth and Lu (1972) models which describe increased q^2 generation near the surface; (2) an axial velocity skewness increase with proximity to the

surface, indicating a near-surface increase in intermittent large excursions from the mean; (3) a decrease in vertical velocity skewness with proximity to the surface, reaching a value near zero at 0.5 m; (4) a near-surface increase in axial and vertical velocity gradients with proximity to the surface, with even greater increases in the kurtosis of the velocity gradient; and (5) a $-u'w'$ maximum at 0.5 m, suggesting a buffer sublayer origin for surface-generated Reynolds stress. The increased near-surface vertical velocity skewness and kurtosis are consistent with the presence of weak downward "sweeps" spreading into elongated shear layers as downward motion is blocked and interrupted by a smaller number of energetic upward-moving fluid "ejections." Also, the vertical flux of Reynolds stress is greatest at the lowest measurement level, indicating a mean transport of turbulent energy away from the surface. These preliminary results suggest to Klewicki et al. (1995) that normalized stream-wise turbulence intensity and Reynolds stress profiles may fall on universal curves depicting the characteristics of near-wall motions. Further investigations will be required to verify this hypothesis.

In another SLTEST site experiment, Folz (1997) deployed arrays of up to 24 parallel straight hot-wire sensors and a modular 12-sensor probe designed for direct velocity gradient tensor and shear measurements within the viscous sublayer. His major findings include the stability and R_θ dependence of several viscous sublayer flow and turbulence characteristics: (1) the turbulence intensity and, to a lesser extent skewness, increase with R_θ and instability, but kurtosis is relatively unaffected by these variables; (2) the mean velocity profile is independent of R_θ , but the logarithmic profile slope is stability-dependent; (3) the rms streamwise and vertical velocity gradients are independent of R_θ , but the gradient kurtosis increases with R_θ ; (4) turbulent kinetic energy production and dissipation rates and vorticity production are independent of R_θ ; (5) turbulent kinetic energy q^2 dissipation is highly correlated with strong positive vertical and axial velocity gradients at high R_θ , but the vertical velocity contributes little to q^2 at low R_θ .

4.4 MEASUREMENTS AROUND ISOLATED CUBES

Metzger and Klewicki (1996) provide a detailed description of a series of measurements made around a 0.25-m cube positioned on the salt flat surface at the SLTEST site. They also discuss measurements made in the wake of the 2-m cube while it was positioned on the ground near Tower Grid for the recirculation region studies (refer to Section 2.2 for details of the Recirculation Subtest trials). The purpose of the SLTEST 0.25-m cube experiment was to explore whether the flow field around a surface-mounted cube is independent of R_θ , while the 2-m cube wake measurements were made to determine wake width for the Recirculation Subtest trials. Figure 9 shows the coordinate system adopted at both sites. The origin is at the center of the bottom cube face with x representing downwind distance (into the wake), y representing spanwise (crosswind) distance, and z representing vertical distance. All distances were normalized by cube face length h, the characteristic dimension of the cube.

The SLTEST cube trials included axial velocity and surface pressure measurements designed to characterize surface pressure and axial velocity

statistics in the proximity of the 0.25-m cube. Several sets of pressure time series measurements were taken at normalized spanwise distances ranging from 0.75 to 2.0. The results show a turbulent kinetic energy gain of an order of magnitude or more in the disturbed flow region, increasing with proximity to the side of the cube. Metzger and Klewicki (1996) conclude that large flow obstacles such as the cube enhance the high frequency content of the turbulent boundary layer through the stretching and reorientation of vorticity. They also note that the skewness of the pressure fluctuations very near the cube ($y/h = 0.75$, or 6.25 cm spanwise from the cube surface) is positive due to relatively infrequent energetic high pressure excursions, but becomes slightly negative at $y/h > 1$ and remains so in the free atmosphere beyond this distance.

Axial velocity measurements were also made at five positions defined by $z/h = 0.125$ and $x/h = 0$, with y/h ranging from 0.6 to 1.24. Metzger and Klewicki (1996) report that the axial velocity fluctuation probability distribution functions (PDFs) at $y/h < 1.0$ feature positive skewness and sharp peaks, while at $y/h \geq 1.0$ the flow begins to relax back to that of the undisturbed boundary layer with a nearly Gaussian axial velocity PDF. Test results suggest that the shape, stability, and structure of the horseshoe vortex which wraps around the cube is Reynolds number dependent. Additional measurements are required to verify this hypothesis.

Half-wake widths behind the 2-m cube were determined from measurements by six single-element hot-wire probes positioned at $z/h = 0.5$ and $x/h = 1.25$, as shown in Figure 9. The purpose of these measurements was to define the wake width, which is defined by Hunt and Castro (1984) as the distance between shear layer centers. The velocity profile shear layer center is located midway between the maximum and minimum velocity positions where the rms axial velocity peaks. A total of eight successful 10-min runs were accomplished consisting of six with the front face of the cube oriented normal to the wind (face-on) and two with the cube oriented 45° relative to the mean wind (corner-on). Because fine dust particles from the clay surface interfered with the hot-wire measurements in the Tower Grid area, fewer wake width measurements are available than were planned.

The hot-wire anemometer measurements in the wake of the 2-m cube were analyzed for mean and rms axial velocity. Figure 10 shows the spanwise mean and rms axial velocity profiles for the six face-on and two side-on cube orientation trials. Metzger and Klewicki (1996) use normalized distance to the peak rms axial velocity from run #6 and assume a symmetric flow to estimate a cube wake width of $y/h = 1.3 \pm 0.1$ for the face-on orientation, which is consistent with results from earlier studies at low Reynolds numbers. The side-on results (Figures 10c, 10d) were insufficient to draw definitive conclusions.

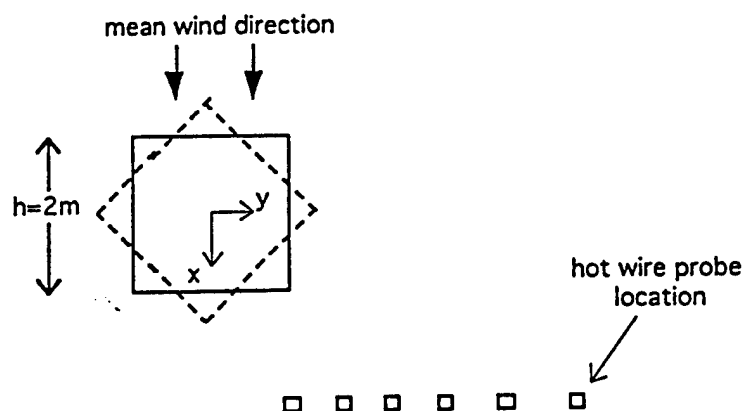


Figure 9. Plan view diagram of the 2-m cube in its face-on (solid line) and side-on (dashed line) positions with respect to the mean wind, and hot-wire probe positions. Hot-wires are positioned at a height of 1 m AGL, a distance of $5h/4$ downwind of the cube center, and spanwise distances y/h of 0.5, 0.75, 1.0, 1.3, 1.7, and 2.0 (after Metzger and Klewicki, 1996).

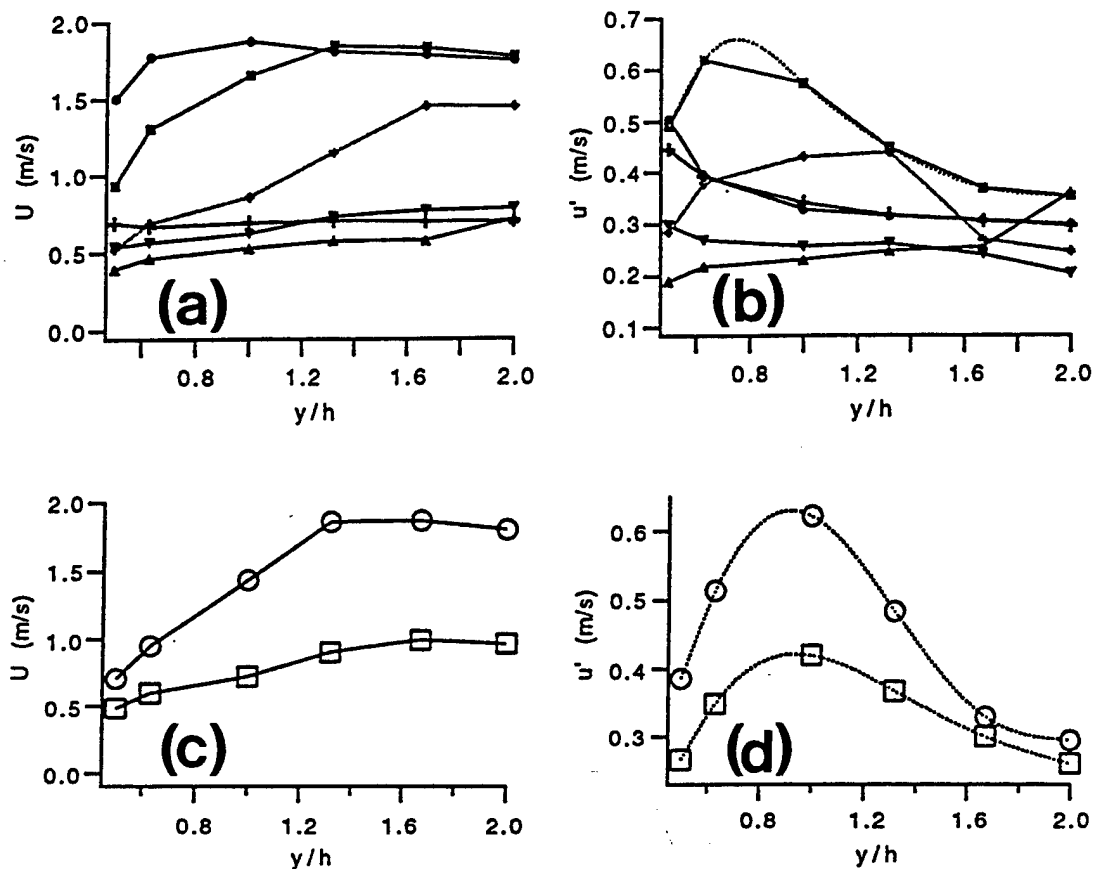


Figure 10. Wake profiles of mean (a) and rms (b) axial velocities at indicated normalized spanwise (y/h) distances with cube in a face-on orientation, and profiles of mean (c) and rms (d) axial velocities for side-on orientations (from Metzger and Klewicki, 1996).

SECTION 5. PLUME PROFILES AND TURBULENCE EFFECTS

5.1 NEAR SURFACE PLUME PROFILE CHARACTERISTICS

Vertical profiles of plume concentrations were obtained during the Plume Profile and Turbulence Effects Subtest conducted from 21 July (Julian date JJJ = 202) to 3 August 1995 (JJJ = 215) at the Tower Grid test site. Figure 11 illustrates the experimental configuration. Each trial began with the release of a known quantity of a tracer gas (propylene) at distances ranging from 12.5 to 100 m upwind of a tower decorated with TIP-SJ2 photoionization detectors (PIDs). The gas was released through a 5-cm diameter PVC pipe, producing a continuous propylene plume for trial durations ranging from 16 to 35 min. Gas release heights were at 0.05, 1.0, or 2.5 m, respectively representing releases in the near-wall, lower, and mid regions of the inertial sublayer. A triangular open-mesh galvanized metal 9-m tower with a dimension of 46 cm on each side supported the detectors. The PIDs were mounted at heights ranging from 0.25 to 9.0 m, with 0.5-m spacing from 0.5 to 3.0 m and 1-m spacing from 3.0 to 9.0 m. Trial summaries, with trial names defined by the two-digit Julian date (JJ) and start times (nnnn in Mountain Daylight Time) are given in Table 3. Detailed plume profile information is available in Appendix A.

TIPSJ2 PIDs have sufficiently fine temporal and spatial response to resolve the details of a plume's internal concentration time history. Each PID contains an orifice, an illumination chamber with an ultraviolet lamp, a set of electrically biased collector plates, a fan which draws air through the detector, and supporting electronics. Air drawn through the detector is illuminated by the ultraviolet lamp. Gases passing through the illumination chamber that have ionization potentials of 10.6 electron-volts (eV) or less (propylene's ionization potential is 9.73 eV) are ionized, producing charged particles. Electric currents generated as the charged particles impinge upon plates biased with the opposite charge produce voltages. These voltages are related through calibration curves to airborne gas concentrations. The TIPSJ2 frequency response is about 0.0037 s (6 dB fall-off at 270 Hz). The TIP-SJ2 output was logged at 4000 Hz using a fast sample-and-hold analog-to-digital (A/D) converter with 16-bit resolution. Further details on the TIP-SJ2s, the data collection system, and procedures used to generate propylene concentration statistics can be found in Yee et al. (1993).

The plume profile summaries in Table 3 contain the plume release height z_s , plume centroid height z_c , height of the plume profile peak concentration z_p , peak-to-mean concentration ratio P/M, and unconditional concentration fluctuation intensity i . The plume centroid height is defined as the height of the detector with the maximum mean concentration. The peak concentration C_{pk} at each detector is the concentration exceeded 1 percent of the time, and P/M is the ratio of the profile-maximum C_{pk} to the mean concentration at the plume centroid. The unconditional fluctuation intensity i is the standard deviation of the measured concentrations (zero concentrations included) at the plume centroid divided by the mean plume centroid concentration.

Table 3. Plume Profile Subtest Trial Summaries.

Trial Name	Start Time (UTC)	Trial Duration (min)	Source Strength (l/min)	Downwind Distance (m)	Source Height (m)	Centroid Height (m)	Peak X Height (m)	Peak/ Mean Ratio	Fluctuation Intensity
P020550	1152	35	100	25	1.00	0.25	0.50	6.69	1.65
P020635	1244	35	200	50	1.00	0.50	0.50	15.79	3.02
P020720	1325	35	200	50	1.00	1.50	0.50	16.83	2.77
P030545	1146	13	200	50	1.00	M ^a	M	M	M
P030646	1245	35	50	50	1.00	0.50	0.50	6.04	1.57
P030745	1343	35	120	50	0.05	0.50	1.50	7.94	1.82
P030845	1519	35	75	25	0.05	1.50	1.50	20.66	4.28
P060530	1128:30	35	25	25	0.05	M	M	M	M
P060805	1408:30	35	50	25	1.00	1.50	1.50	16.09	3.27
P070435	1032:30	35	60	25	1.00	1.00	1.00	9.94	2.08
P070515	1123	35	20	12.5	1.00	1.00	1.50	10.00	1.96
P070605	1200	35	20	20	0.05	M	M	M	M
P070640	1254	35	5	12.5	0.05	0.25	0.25	9.95	2.09
P100405	1006	35	40	25	1.00	1.00	1.00	11.12	2.39
P100550	1149:20	35	70	75	1.00	0.25	0.50	7.29	1.36
P100630	1226:30	35	110	75	0.05	M	M	M	M
P100705	1308:30	35	110	75	2.50	1.50	1.50	8.05	1.87
P122325	0521	35	40	75	2.50	2.00	2.50	12.01	2.45
P132250	0446	35	200	100	2.50	M	M	M	M
P132340	0534	35	200	100	2.50	M	M	M	M
P140030	0625	35	200	100	0.05	0.50	1.00	12.31	2.57
P142154	0355	35	250	100	2.50	M	M	M	M
P142245	0458	35	250	100	0.05	M	M	M	M
P150010	0608:45	35	250	100	2.50	1.50	1.50	6.18	1.58
P150050	0649	24	250	100	0.05	0.50	1.50	13.46	2.57

^a M = Insufficient data available for concentration statistics calculations.

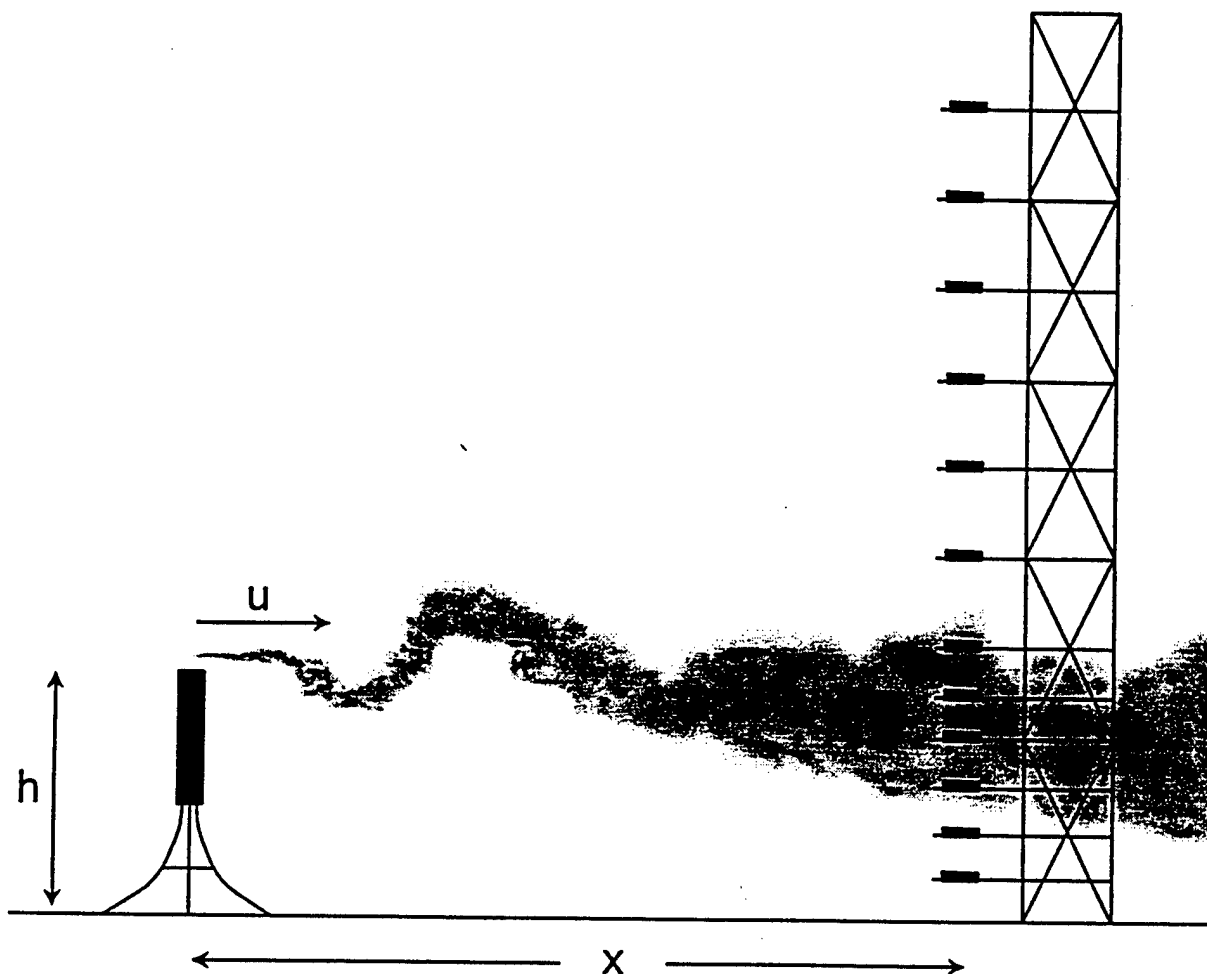


Figure 11. The propylene disseminator and tower-mounted sampling array (not to scale).

An understanding of the physical mechanisms which cause changes in plume centroid height is important for modeling near-surface dispersion because model predictions are based on the premise that the plume centroid location is known. In particular, z_c and z_p are assumed to be consistent with z_s , with changes in centroid height accounted for by reflection arguments. Differences between z_s , z_p , and z_c attributable to physical mechanisms other than surface reflection are apparent in the Table 3 data. In qualitative terms, the centroids of plumes released above the surface into an adiabatic atmosphere tend to descend toward the surface, while the centroids of plumes from surface releases tend to rise. Also, z_p is typically found above z_c . The physical mechanisms affecting the plume centroid height include initial conditions such as plume momentum and buoyancy and "far field" effects such as flux divergence and turbulence skewness.

Biltoft (1995) analyzed the initial conditions for propylene released from the dissemination system used in these trials. He concluded that the momentum effect is negligible, but that density-driven slumping occurs during light winds. The plume Richardson number, defined by Chatwin (1985) as

$$R_p = g'b/u_*^2 \quad (5-1)$$

where g' is a density-weighted gravitational acceleration and b is a characteristic cloud length, determines whether or not material released into the atmosphere will slump toward the surface. Chatwin's criterion for a gravity-dominated dense gas is $R_p \gg 0.2$; neutrally-buoyant behavior is expected for $R_p \ll 0.2$, and a transitional condition exists for R_p on the order of 0.2. Using these criteria, propylene typically exits the disseminator as a dense gas, but entrainment of ambient air into the plume rapidly reduces R_p below the slumping threshold unless the release occurs during quiescent nocturnal conditions ($u_* \leq 0.1$ m/s). Under quiescent conditions, denser-than-air gases such as propylene slump toward the surface and fan out in a shallow pool until sufficient mixing occurs to overcome gravitational effects. Slumping likely lowered the centroid heights for Trials P030545, P100550, P100705, P122325, P132250, P132340, P140030, P142154, and P142245 of this series.

In addition to the initial conditions, the plume centroid position is determined by characteristics of the turbulent wind field into which it is released. Raupach (1983) considers the dispersion of a neutrally-buoyant tracer into an idealized adiabatic turbulent flow and derives an analytic expression for the mean tracer particle vertical drift velocity v as a function of u_* . This equation is

$$v(t) = bu_*(1 - e^{-t}(1 + t)) , \quad (5-2)$$

where b is a constant on the order of 0.4 and t is travel time non-dimensionalized by the Lagrangian time scale. Thus, the vertical plume centroid position is related to measureable ABL quantities such as u_* and, through Equation (3-12), to σ_w . Superimposed on this idealized relationship are non-Gaussian effects such as skewed turbulence, which enhances plume centroid rise during convection (see Wyngaard and Weil, 1991), and stable thermal stratification, which suppresses plume centroid rise.

The plume centroid height also influences the magnitude of the concentration fluctuation intensity i and peak-to-mean ratio P/M . The fluctuation intensities presented in Table 3 are those found at the plume centroid. These are "total" or "unconditional" statistics, which include the zero concentrations readings that occurred when the plume meandered away from the detector array. Yee et al. (1993) suggest that i at the plume centroid can be represented as a power law function of downwind travel distance normalized by z_* ,

$$i = 26.6 (x/z_s)^{-0.55} . \quad (5-3)$$

Implicit in Equation (5-3) is the assumption that the plume's height above the surface largely determines the intensity of small-scale turbulence acting on the plume. For example, a plume released near the surface will be subjected to more intense small scale mixing (reducing i) than a plume released above the surface. However, measured fluctuation intensities exhibit considerable scatter about the fluctuation intensities calculated using Equation (5-3). The fluctuation intensity is often not well defined using the x/z_s normalization because the centroid of a plume released into the atmosphere does not necessarily remain at the release height, and the plume is subjected to decreased (or increased) internal mixing depending on whether the centroid rises (or sinks). A considerable decrease in scatter was obtained with Equation (5-3) using an x/z_c normalization, suggesting that the plume centroid vertical position time history must be known to accurately estimate i .

The assumption that the plume peak concentration is found at the plume centroid is frequently violated, particularly when z_c originates near the surface. The intensity of fine scale turbulence is at a maximum near the surface (see Stull, 1988). Thus, the concentration gradients within the near-surface portion of the plume are rapidly destroyed by intense mixing. This mixing reduces both the concentration peaks and adjacent pockets of clear air, while leaving the mean concentration relatively unchanged. Near surface mixing operates on a timescale shorter than the timescale of the turbulent fluxes that elevate the plume centroid. The result is that z_p often remains at or rises above z_s , particularly when the plume centroid sinks toward the surface.

In spite of its importance to dispersion modeling, only a rudimentary understanding of near-surface plume profile behavior exists. While studies like those performed by Raupach (1983) and Wyngaard and Weil (1991) provide useful insights into plume centroid behavior, the development of a physically valid plume centroid vertical displacement model will require improved understanding of scalar variance vertical transport and its relationship to quantities such as the fluxes of heat and momentum. Specifically, the contributions of the velocity-concentration correlation and correlation gradient terms in the scalar variance transport equation must be better understood, which will require the development of instrumentation capable of providing velocity-concentration correlation measurements.

5.2 NEAR SURFACE WIND AND TURBULENCE ANALYSES

The vertical array of PIDs at the Tower Grid test site was accompanied on the 9-m tower by Applied Technologies, Inc. sonic anemometer/thermometers (sonics), each consisting of an ultrasonic sensor array and an electronics module. The sonic arrays were mounted with an orientation toward 240° with respect to true North. Two-axis sonic arrays (Model RSWS-201/2A) were located at the 1.5- and 6.0-m levels, and tri-axis sonics (Model RSWS-201/3A) were located at the 3.0- and 9.0-m levels. The two-axis sonics provided measurements of the horizontal wind components which were rotated into the mean alongwind u and crosswind v components during data processing. The tri-axis

sonics provided measurements of all three components of the wind vector (u , v , and vertical w) which were subjected to an identical horizontal coordinate rotation into the mean wind. All of the sonics also measured the speed of sound, which was subsequently converted into sonic temperature (nearly identical to virtual temperature). The sonic data collected at a rate of 10 Hz provided sufficient temporal and spatial resolution to characterize the surface boundary layer turbulence in the vicinity of the tower. Statistical summaries of the sonic data collected during dissemination periods are presented in Appendix A.

Disseminations for the Plume Profile and Turbulence Effects Subtest were planned for wind speeds ranging from 1 to 6 m/s and wind directions within $\pm 60^\circ$ of 180° . Most of the trials occurred with wind speed less than 3 m/s. An attempt was made to select dissemination time periods when the wind direction was steady, but abrupt changes in wind direction due to turbulence bursts or terrain-induced meander often carried the plume away from the array. Attempts were made during some trials to realign the source to increase plume passage through the detector array, but most data sets contain large blocks of zero concentrations due to persistent meander.

Table 4 gives the Plume Profile and Turbulence Effects Subtest trial micrometeorological summaries. These summaries include wind and temperature statistics, friction velocity, and the Obukhov length as a stability parameterization. Because none of the eddy correlation-derived friction velocities met the Busch and Panofsky (1968) quality criterion ($u_* > 0.32$ m/s), Equation (3-12) was used to estimate u_* . Table 4 also provides $\overline{u'T'}$ computed from sonic measurements at the 1.5- and 6-m levels, and the Diabatic Ratio, which was derived from covariance quadrant contributions to $\overline{u'T'}$ (discussed below).

An interesting observation from this trials series is that, although detailed meteorological measurements were made near the times of transition through sunrise and sunset, conventional "neutral" stability was not observed. Both the Obukhov length and Diabatic Ratio (defined later) indicate that, during the transition from a very unstable to a very stable ABL, both stabilities exist simultaneously within different layers. For example, measurements from the 1.5- and 6.0-m levels during Trial P122325 (Table 4) indicate a very stable layer within a few meters of the surface with an unstable layer persisting above it well into the night. It appears that the nocturnal stable layer develops near the surface and gradually progresses through successively deeper ABL layers after sunset. Thus, transition in the desert ABL consists of a superposition of diabatic layers rather than a true adiabatic ABL. The extreme stability conditions indicated by the small Obukhov lengths calculated for many of the trials are artifacts of very light winds, which produce near-zero (and statistically unstable) fluxes.

Another characteristic of the Table 4 trial summaries is the extreme stability conditions, as indicated by the small Obukhov lengths calculated for many of the trials. These small Obukhov lengths are artifacts of the light winds which produce small values of σ_w and u , which, when cubed, produce a small L . The abrupt change between similarity-based stability extremes that

Table 4. Plume Profile Subtest Trial Micrometeorological Summaries.

Trial Name	Temperature		Surface Pressure (mb)	Wind Speed (m/s)	Friction Velocity (m/s)	wT' (mK/s)	Obukhov Length (m)	u'T' (mK/s)			Diabatic Ratio Nondimensional	
	Surface (°C)	2.0 m (°C)						1.5 m	6.0 m	1.5 m		
P020550	19.5	19.6	866.6	ND*	ND	ND	ND	ND	ND	ND	ND	ND
P020635	16.5	16.9	866.5	2.2	0.14	-0.049	+53.	+1549	+1028	0.03	0.10	0.10
P020720	23.1	20.2	866.7	1.0	0.12	+0.172	-8.	-1005	-0873	3.84	3.30	3.30
P030545	12.6	13.6	866.2	1.0	0.05	-0.072	+2.	+0402	+0882	0.09	0.07	0.07
P030646	12.4	13.8	866.3	1.3	0.13	+0.183	-8.	+0876	+0574	0.31	0.54	0.54
P030745	15.7	19.2	866.4	2.3	0.16	+0.327	-9.	+2289	+3198	0.24	0.14	0.14
P030845	32.6	24.0	866.6	1.0	0.18	+0.686	-6.	-0831	-0662	1.86	1.95	1.95
P060530	10.8	11.8	865.7	1.7	0.03	-0.210	+0.1	+3080	+0042	0.02	0.91	0.91
P060805	23.5	21.9	866.7	0.8	0.13	+0.221	-7.	-0272	-0301	2.65	3.15	3.15
P070435	16.4	20.5	862.3	1.8	0.15	-0.225	+12.	+1522	+1425	0.17	0.15	0.15
P070515	15.1	20.6	863.0	2.7	0.21	-0.427	+16.	+2235	+1898	0.09	0.13	0.13
P070605	13.9	17.6	863.4	1.3	0.09	-0.049	+10.	+1617	+3573	0.04	0.16	0.16
P070640	13.3	18.9	864.0	1.8	0.07	-0.068	+3.	+0137	+0733	0.83	0.17	0.17
P100405	16.8	19.8	866.5	1.2	0.07	-0.078	+3.	+2075	+1745	0.07	0.06	0.06
P100550	14.0	15.0	866.7	1.4	0.05	-0.109	+1.	+0187	+4762	0.87	0.06	0.06
P100630	14.5	16.5	866.8	1.8	0.04	-0.046	+1.	-1427	-0284	5.28	1.17	1.17
P100705	15.0	19.3	866.9	1.7	0.05	+0.106	-1.	-0884	-2346	1.49	6.75	6.75
P122325	14.2	16.4	865.8	1.3	0.04	+0.043	-1.	+1749	-1197	0.03	8.30	8.30
P132250	21.5	23.6	865.7	2.0	0.05	-0.220	+0.6	+1886	+1394	0.33	0.25	0.25
P132340	21.3	22.6	865.5	1.6	0.06	-0.136	+1.	+3040	+1195	0.11	0.33	0.33
P140030	19.3	20.5	865.4	1.7	0.08	-0.127	+3.	+0197	+0512	0.69	0.68	0.68
P142154	24.2	25.2	865.5	1.7	0.08	-0.070	+5.	-0163	+0446	1.07	0.78	0.78
P142245	22.2	22.4	865.4	1.6	0.08	-0.043	+8.	+2899	-0682	0.20	1.43	1.43
P150010	21.4	22.5	865.5	2.3	0.13	-0.287	+6.	+4336	+3325	0.15	0.25	0.25
P150050	21.5	23.0	865.5	2.4	0.11	-0.169	+6.	+0531	+0825	0.33	0.30	0.30

* ND = No data available.

occurs during the high desert boundary layer transition through sunrise and sunset in light winds is not accompanied by comparable changes in turbulence levels, and hence by extreme differences in the rate of diffusion. This situation calls into question the adequacy of similarity-based boundary layer representations, particularly at non-ideal sites and during non-steady conditions where adequate vertical velocity measurements or reliable u estimates are unlikely to be available.

The limitations of similarity-based boundary layer representations suggest a need for a more robust method for describing the turbulent state of the atmosphere, particularly during non-ideal conditions. Desirable characteristics for an improved stability and turbulence parameter include: (1) ease of calculation in near real-time from near-surface measurements using a single robust instrument, (2) sensitivity to changes in stability and turbulence levels, (3) statistical stability during non-ideal conditions, and (4) a mathematically tractable and physically meaningful scale range. In this study, the search for a new stability parameterization focused on the $\overline{u'T'}$ covariance term in the stress budget equation (see term [3] of Equation (3-1)) because indices based on velocity-temperature covariance measurements from a two-axis sonic anemometer/thermometer appear to most nearly satisfy these criteria.

The $\overline{u'T'}$ covariance offers several practical advantages over the $\overline{u'w'}$ and $\overline{w'T'}$ covariances as a turbulence indicator: (1) the absence of a vertical velocity measurement requirement relieves the need for research-grade instrument (such as a tri-axis sonic) and precise sensor leveling and alignment (for a discussion of these effects, see Haugen and Kaimal, 1969); (2) measurements made only in the horizontal plane can be obtained from two-axis sonic arrays positioned close (within a meter, depending on z_0) to the surface, while tri-axis sonics should be mounted at higher levels; (3) $\overline{u'T'}$ is statistically more stable than $\overline{u'w'}$ (a 10-min sampling period appears to provide a reasonable $\overline{u'T'}$ estimate); and (4) because u' is usually larger than w' , $\overline{u'T'}$ is typically larger than the $\overline{u'w'}$ or $\overline{w'T'}$ obtained during the same sampling period.

The $\overline{u'T'}$ covariance is typically considered a horizontal temperature flux term (see, for example, Wyngaard et al., 1971), but its magnitude and sign appear to vary with stability and with day-night transitions in ways that are similar to the variations in $\overline{w'T'}$. Also, except in the presence of dynamic frontal boundaries, the horizontal temperature gradient does not support the observed magnitude of $\overline{u'T'}$ (i.e., horizontal temperature advection is usually weak). Because vertical momentum and temperature gradients usually exceed their horizontal gradients by several orders of magnitude, the fluctuating velocity and temperature components that make the predominant contribution to $\overline{u'T'}$ most likely originate with vertical eddy exchanges. That is, the vertical flux of the temperature-momentum covariance is likely to contribute more than the horizontal temperature flux to the magnitude of $\overline{u'T'}$. The remainder of this section examines the relationship of $\overline{u'T'}$ to non-steady boundary layer processes using Fourier spectrum analysis and covariance quadrant analysis.

Fourier spectrum analysis involves the conversion of time series data from the time domain into the frequency domain. Fourier analysis is based on the premise that any continuous time series can be represented by a finite number of sinusoidal components summed over a finite frequency range. It offers the advantage of describing the distribution of the variance or covariance of time-varying quantities among the range of frequency scales that form the time series. That is, Fourier analysis partitions energy by frequency rather than by time. The Fourier transformation partitions power (change in a variable per unit time) of a time series into harmonic frequency components. An advantage offered by this power spectrum partition is that the power (or turbulent energy) within one harmonic is independent of the amplitudes, phases, and frequencies of other harmonics present within the time series. Thus, spectrum analysis displays the distribution of turbulent energy content within a time series as a function of turbulence scale. Additional information on time series analysis for boundary layer phenomena is given by Stull (1988) and Kaimal and Finnigan (1994).

Relationships between two time series can be evaluated by examination of the complex products of their spectra such as the cross spectrum, phase, and coherence. The cross spectrum includes the cospectrum (the in- or out-of-phase portion of two spectral frequencies) and the quadrature (that portion of the paired frequencies shifted by $\frac{1}{4}$ wavelength, or 90°). The phase and coherence provide the same information in a normalized polar coordinate system, with the angular phase relationship defined by

$$\text{Phase} = \text{ATAN2}(\text{quadrature}/\text{cospectra}) \quad (5-4)$$

where ATAN2 is an arctangent function expanded to the range $-\pi$ to π . Phase information is presented in degrees, with 0° indicating an in-phase and 180° representing an out-of-phase relationship. The coefficient of coherence is a measure of the correlation between two time series presented as a function of frequency. It is given by

$$\text{Coherence} = (\text{COS}^2 + \text{QUAD}^2)/(\text{Spctr1}) * (\text{Spctr2}), \quad (5-5)$$

where Spctr1 and Spctr2 are the spectral component magnitudes of time series 1 and 2 and COS and QUAD respectively denote the cospectrum and quadrature spectrum. Kaimal and Gaynor (1983) describe the fast Fourier transform (FFT) spectrum analysis program used to process the sonic 10-Hz u and T data. The spectra produced by this FFT program are smoothed through block averaging, tapered, scaled to meter-kilogram-second (mks) units, and normalized by multiplying each harmonic component by its frequency. Fourier analysis of $\overline{u'T'}$ provides information on how the surface layer responds to the influx of energy during a transition through sunrise, as shown in the Figure 12 and summarized in Table 5. The details of Figure 12 and Table 5 are discussed as part of the case study analysis in Section 5.3.

Table 5. Cospectra, Quadrature, Phase, and Coherence for 1.5-m u and T Components During Transition Through Sunrise at Tower Grid on 22 July 1995.*

Frequency (Hz)	Cospectra (m K/s)			Quadrature (m K/s)			Phase (Degrees)			Coherence (ND)		
	0645	0743	0845	0645	0743	0845	0645	0743	0845	0645	0743	0845
0.0017	-.00541	.06674	-.03354	-.00384	-.05588	.05868	215.	040.	120.	.463	.629	.556
0.0031	.01087	.00107	-.03764	.00467	.00907	-.00096	023.	083.	181.	.360	.039	.346
0.0055	.00402	-.00998	-.01397	-.00004	.01576	-.00898	359.	122.	213.	.188	.095	.218
0.0099	.00087	-.02707	.00510	-.00141	-.00448	-.00029	302.	189.	357.	.036	.305	.005
0.0180	.00818	-.01362	-.02309	.00343	.01152	.01664	023.	140.	144.	.282	.327	.219
0.0586	.00206	-.00267	-.00745	-.00022	-.00001	.00917	354.	180.	129.	.343	.234	.118
0.0977	.00334	-.01384	-.00635	-.00053	.00256	.00881	351.	170.	126.	.392	.655	.302
0.1658	.00254	-.00720	.00024	-.00000	-.00006	.00101	360.	180.	077.	.337	.487	.005
0.2728	.00100	-.00513	-.00144	-.00000	.00068	.00012	360.	172.	175.	.110	.371	.015
0.4280	.00121	-.00433	-.00069	-.00011	.00028	.00061	355.	176.	138.	.176	.337	.013
0.6901	.00042	-.00290	-.00055	-.00004	.00086	.00033	355.	178.	149.	.059	.180	.010
1.1072	.00020	-.00133	-.00048	-.00008	.00005	.00005	338.	178.	174.	.030	.077	.012
1.7667	.00006	-.00073	-.00002	-.00006	-.00016	.00025	314.	192.	094.	.010	.049	.008
2.7952	.00004	-.00020	-.00010	-.00003	-.00006	.00005	327.	198.	154.	.012	.011	.006
4.4439	.00002	-.00014	-.00001	-.00001	-.00005	-.00002	348.	199.	121.	.008	.015	.001

* Times are in Mountain Daylight Time (MDT).

Another technique applicable to $\overline{u'T'}$ studies is covariance quadrant analysis. The covariance of any quantities A and B, where A' and B' represent fluctuations about the means \bar{A} and \bar{B} , include positive (greater than the mean) and negative (smaller than the mean) A' and B' values. Thus, there are four possible combinations of A' and B': (1) A' > 0, B' > 0; (2) A' > 0, B' < 0; (3) A' < 0, B' < 0; and (4) A' < 0, B' > 0. If either A' or B' is near-zero, the contribution of the A'B' product to the flux is near-zero. Thus, the covariance can be divided into four quadrants which contribute to the flux plus a fifth no-flux region near the zero axes (see Figure 13). Because the velocity resolution threshold for ATI sonics is near 0.03 m/s, this threshold was defined as the boundary of the no-flux region. As noted by Raupach (1981), the sum of the covariance fraction contributions from all of the quadrants is the total covariance. Covariance quadrants and the no-flux region for $\overline{u'T'}$ are depicted in Figure 13.

The similarities in the diurnal variations of $\overline{u'T'}$ and $\overline{w'T'}$ can be explained by a simple model of the boundary layer. Consider a horizontally homogeneous boundary layer in which discrete eddies move through a horizontal plane in response to a Gaussian vertical velocity distribution with zero mean. Because wind speed increases with height in this idealized boundary layer, eddies descending from above the horizontal plane produce wind speed fluctuations u' above the mean wind speed in the plane, while eddies rising from below produce wind speed fluctuations below the mean wind speed. Thus, $u'+$ is associated with a negative vertical velocity fluctuation $w'-$ and $u'-$ is associated with a positive vertical velocity fluctuation $w'+$. Quadrant Q1 ($u'+, T'+$) and quadrant Q3 ($u'-, T'-$) eddies moving through the horizontal plane both make positive contributions to $\overline{u'T'}$. Following the reasoning given above, the signs on the horizontal velocity fluctuations indicate that the Q1 eddies are associated with the downward flux of air that is warmer than the air at the height of the horizontal plane and the Q3 eddies are associated with the upward flux of cooler air. The stable thermal stratification implied by the Q1 and Q3 eddies suggests that they are driven by shear-induced turbulence rather than convection. Similar reasoning suggests that the Q2 ($u'+, T'-$) and Q4 ($u'-, T'+$) eddies, which make negative contributions to $\overline{u'T'}$, are respectively associated with the downward flux of cooler air and upward flux of warmer air. The unstable stratification implied by the Q2 and Q4 eddies is consistent with convection.

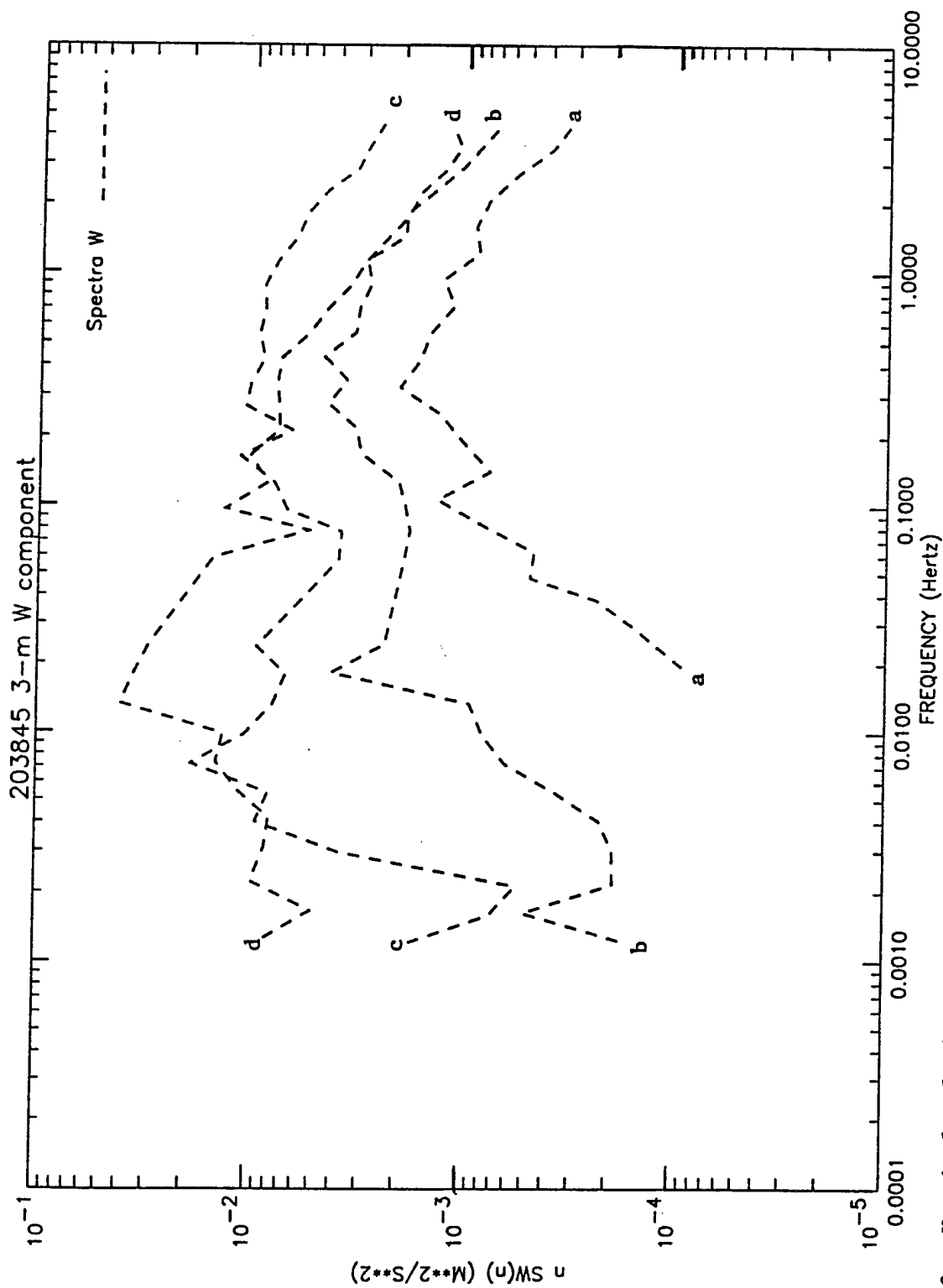


Figure 12. Vertical velocity spectra measured at the 3-m level for four successive time periods (A: 0545-0557; B: 0645-0711; C: 0745-0815; D: 0845-0917) during the transition through sunrise on 22 July 1995.

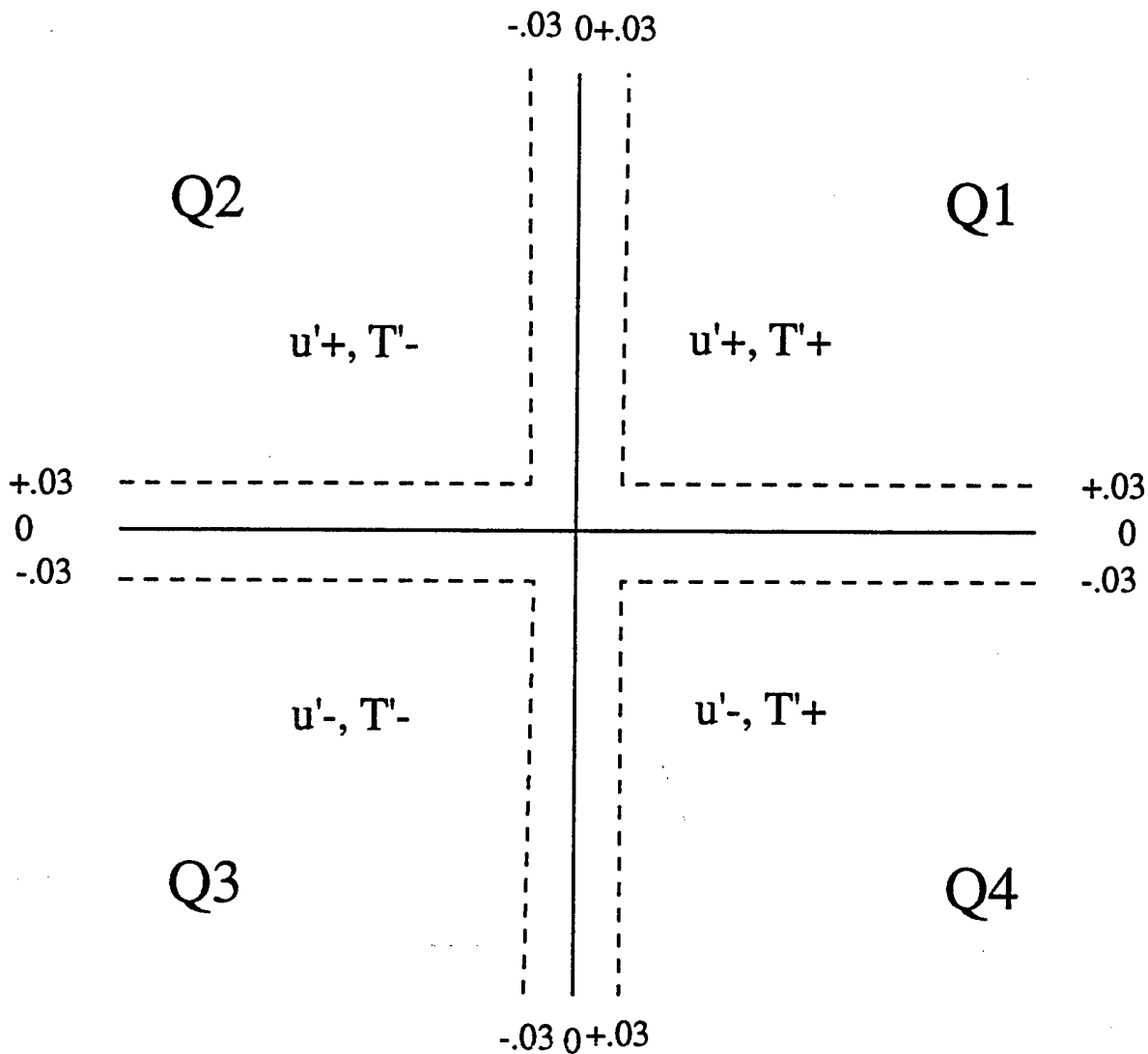


Figure 13. Covariance quadrant analysis categories for $\overline{u'T'}$: (1) Q1: $u' > 0$, $T' > 0$; (2) Q2: $u' > 0$, $T' < 0$; (3) Q3: $u' < 0$, $T' < 0$; (4) Q4: $u' < 0$, $T' > 0$; and (5) the no-flux region where the departures of u' or T' from their means do not exceed ± 0.03 m/s or 0.03 °C, respectively.

The simple boundary layer model discussed above leads to the hypothesis that the magnitudes of the positive (Quadrants Q1 and Q3) and negative (Quadrants Q2 and Q4) contributions to the total $\overline{u'T'}$ can be used to estimate the relative contributions of shear-driven and convection-driven turbulence. A new stability parameter, the "Diabatic Ratio," is then given by

$$DR = |Q2 + Q4| / (Q1 + Q3) \quad (5-6)$$

where Q1, Q2, Q3, and Q4 are the contributions from the four quadrants to $\overline{u'T'}$. (Note that the numerator of Equation (5-6) is the absolute value of the sum of the quadrants with negative contributions to $\overline{u'T'}$.) DR serves as a simple stability indicator with $DR < 1$ indicating shear-dominated turbulence and $DR > 1$ indicating convection-dominated turbulence. If $DR = 1$, neither shear nor convection dominates, which is consistent with an adiabatic boundary layer.

The simple boundary layer model also suggests that the magnitude of the $\overline{u'T'}$ contribution in each quadrant is directly proportional to the vertical velocity fluctuations that move eddies through the horizontal measurement plane. Thus, the "Total Diabatic Influence" given by

$$TDI = \sum_{i=1}^4 |Q_i| \quad (5-7)$$

should be proportional to the mean vertical velocity variance σ_w^2 . This hypothesis was independently tested using 36 tri-axis sonic anemometer data sets. Part of the data sets came from sonics mounted at 2.0 m AGL over salt flats in the Great Salt Lake Desert (Biltoft, 1997) and part came from sonics mounted at 4.0 m AGL in the San Joaquin Valley in California. Wind speeds on the salt flats were light to moderate (2.1 to 8.4 m/s), while the San Joaquin Valley winds were very light (0.6 to 1.6 m/s). Stabilities ranging from very stable to very unstable were represented in this integrated data set. Trial durations varied, but were typically 60 min or longer. No trend removal filter was applied to these data. The linear correlation between TDI and the measured $\overline{\sigma_w^2}$ was 0.835, indicating that 70 percent of the vertical velocity variance was explained by its relationship to TDI. This result is significant based on an F test at the 1-percent level. Section 5.3 below demonstrates the utility of DR and TDI for characterizing stability and boundary layer turbulence during non-steady conditions.

Several refinements to the DR and TDI are possible. The present method gives equal weights to the contributions from all four quadrants without consideration of the number of occurrences in each quadrant. Weighting each covariance contribution by the percent of occurrences within that quadrant could improve the relationship of TDI to σ_w^2 . Also, the contribution from the no-flux region has been ignored because its contribution to the flux is minimal except during very light wind conditions. A proportionality constant of 4 (i.e., $\sigma_w^2 \approx TDI/4$) appears to apply in strongly diabatic boundary layers

where transitions through neutral are rapid, but may not work well in situations where the atmosphere has had sufficient time to become well mixed, as in the persistent cloudy conditions of Northern Europe. Further examination of DR and TDI applicability as stability and turbulence indicators, including covariance quadrant contributions to the Reynolds equations, is beyond the scope of this report, but should be undertaken as follow-on tasks.

5.3 CASE STUDIES OF SUNRISE TRANSITION AND NOCTURNAL TURBULENCE INTERMITTENCY

A series of four trials on 22 July 1995 were selected for a case study analysis of the transition through sunrise. This day was selected because it is representative of a high desert sunrise transition from quiescent nocturnal conditions with wind speeds on the order of 1 m/s to a period of strong convection in light winds. Representative 10-min periods were selected from sequential trials to document conditions during this transition. The 10-min time blocks represent a compromise between the need for a sample that is sufficiently long for second-order statistics to be statistically stable, but sufficiently short to be free of trends and meander. The micrometeorological summaries for each of these 10-min trial segments are given in Table 6.

The micrometeorological summaries (Table 6) of wind and temperature measurements made within the first 2 m of the surface illustrate changes in the wind and temperature fields during a morning sunrise transition. Temperature readings were obtained from the fiberoptic-quartz thermometer with probes at the surface and 2.0 m AGL. A 2-axis sonic provided horizontal wind component and sonic temperature fluctuation measurements at 1.5 m, while a 3-axis sonic supplied vertical velocity measurements at 3.0 m AGL. The mean wind speed remained light, in the range of 1 to 2.5 m/s, with the wind direction from the southwest for the entire transition period. The surface and 2.0-m temperatures remained fairly constant prior to sunrise, and then increased rapidly after 0709 MDT when direct sunlight first reached the ground surface on the grid (sun on the grid is delayed by the shadow of Camel Back Ridge). The rate of surface temperature increase initially lagged that of the air immediately above the surface, possibly due to heat absorption by the cool underlying surface acting as a thermal sink. By the last time period (0901 MDT), the surface thermal lag had been overcome and the ground temperature had rapidly increased to 33.5 °C. It remained 10 to 15 °C above that of the overlying air for the remainder of the trial period.

The arrival of sunlight on the grid at 0709 MDT produced an immediate increase in σ_u , σ_w , σ_T , and $\overline{u'T'}$, but the DR for the 0700-0710 time period remained at 0.08 due to a relatively weak contribution from the second and third quadrant covariance terms. The weak contributions from these quadrants indicates the absence of convection, even though the heating produced enough energy to increase the general level of turbulence by a factor of two to three. The onset of convection, as indicated by a sign change in $\overline{u'T'}$ and an increase in the DR to 2.22, had occurred by the 0750 MDT time period. Convection became well established between 0750 and 0901, with the DR contributions from the second and third quadrants exceeding those of the first and fourth quadrants by a factor of two.

Table 6. Micrometeorological Summaries for Selected 10-min Time Blocks During the Morning Transition From Stable to Unstable Conditions.

Date/Time JJJHHMM (MDT)	WS (m/s)	HD 1.5-m (deg)	Temperature (°C)		σ_v 1.5-m (m/s)	σ_w 3.0-m (m/s)	σ_T 1.5-m (Deg K)	$\overline{u/T}$ 1.5-m (K m/s)	Total Diabatic Influence at 1.5-m	Diabatic Ratio at 1.5-m
			Sfc	2.0 m						
			(°C)	(°C)						
2030548	1.1	204	12.8	13.4	0.145	0.005	0.251	+0.0201	0.0277	0.15
2030647	1.0	224	12.5	13.6	0.140	0.007	0.273	+0.0228	0.0297	0.10
2030700	1.7	210	12.8	13.3	0.310	0.024	0.375	+0.0717	0.0845	0.08
2030750	2.5	210	16.2	18.0	0.447	0.042	0.412	-0.0455	0.1186	2.22
2030901	0.8	199	33.5	23.6	0.523	0.049	0.578	-0.0675	0.2196	1.99

*Note: Sun on the test area at 0709 MDT (delayed by Camel Back Mountain shadow)

Table 7. Micrometeorological Summaries for Selected 10-min Time Blocks During a Nocturnal Quiescent Period (2142205), a Turbulence Burst (2142215), Active Mechanical Turbulence (2150013), and a Turbulence Burst (2150023).

Date/Time JJJHHMM (MDT)	WS (m/s)	HD 1.5-m (deg)	Temperature (°C)		σ_v 1.5-m (m/s)	σ_w 3.0-m (m/s)	σ_T 1.5-m (Deg K)	$\overline{u/T}$ 1.5-m (K m/s)	Total Diabatic Influence at 1.5-m	Diabatic Ratio at 1.5-m
			Sfc	2.0 m						
			(°C)	(°C)						
2142205	1.9	169	23.7	24.6	0.497	0.046	0.982	+0.3623	0.4007	0.05
2142215	1.4	166	23.1	25.5	1.027	0.149	1.427	+0.8957	1.1411	0.12
2150013	2.0	202	21.5	22.6	0.451	0.157	0.398	+0.1178	0.1344	0.07
2150023	2.8	219	21.8	24.5	0.579	0.229	1.530	+0.2022	0.5514	0.46

A detailed picture of turbulence development through the sunrise transition is available through analysis of the temperature-velocity cospectra measured at 1.5 m AGL, as presented in Table 5. Thirty-minute time periods beginning at 0645, 0743, and 0845 MDT were selected for spectrum analysis. The 30-min periods were selected to obtain statistically stable samples. The pre-sunrise period beginning at 0645 MDT featured positive velocity-temperature cospectra with phase angles in the range of $360 \pm 60^\circ$ (indicating a strong in-phase relationship between u' and T' over most of the spectrum). A phase change, with negative cospectra and phase angles shifted to $180 \pm 60^\circ$ is shown in Table 5 for the 0743 MDT period. This out-of-phase relationship between u' and T' (consistent with the increase in covariance Quadrants Q2 and Q3) is characteristic of incipient convective layer development. Also evident from the phase angle time sequence is that convective layer development begins at the higher frequencies and gradually expands into the lower frequencies with a transition through quadrature. This transition is apparent in the 0743 MDT data set which contains a significant portion of low frequency spectral energy in quadrature with phase angles of $090 \pm 60^\circ$. The transition stage is followed by full convection represented by the 0845 MDT period, where phase angle scatter has become more random, but remains centered in the southeast quadrant.

Comparable covariance and spectrum analyses performed at the 3- and 6-m levels (not shown) reveal the sunrise transition beginning in the buffer sublayer and progressively expanding upward through the boundary layer. The 0743 MDT time interval represents a mid-transition period, with the lowest 3 m of the boundary layer experiencing the effects of convection while the layers above remain stable. The result is a DR of 2.22 at 1.5 m and 0.46 at 6-m during this time period, indicating a diabatic superposition (stable over unstable). This suggests that stable and unstable regimes coexist within a few meters of each other in a diabatic boundary layer undergoing sunrise transition. In this scenario, a true adiabatic condition exists only momentarily at the level within the ABL where the stability transition is occurring; an adiabatic state is not representative of the entire ABL at any time during the transition.

The effects of sunrise on vertical velocity spectra at 3-m AGL, as shown in Figure 12, provide additional insights into a boundary layer in transition. The 0545 MDT spectrum (A--A in Figure 12) is typical of nighttime conditions with a distinct low energy "spectral gap" at frequencies below 0.1 Hz. The increased energy present at sunrise (0645 MDT, B--B) is observed across all spectral bands and is particularly pronounced in the spectral gap. The greatest energy increase occurs within the hour after the sun reaches the grid (0745, C--C). A familiar convective boundary layer spectrum with a fully developed energy-containing region and inertial sublayer is present by 0845 MDT (D--D). An interesting feature of this sequence of spectrum plots is the presence of a high frequency energy "overshoot" rather than an inertial subrange in the 0745 MDT spectra. One hypothesis is that this high frequency energy overshoot is a consequence of the restriction on convective motions by the inversion "lid." Just as a lid increases the intensity of boiling in a pot, the inversion lid on a developing convective layer prevents convection from achieving its full vertical development. The result is increased energy available for convective mixing at the higher frequencies within the confines

of the inversion lid. This confined band of highly energetic turbulence should enhance dispersion within the developing convective layer, producing a well mixed plume within a shallow layer just above the surface. Therefore, sunrise transition can produce transient episodes of very high concentrations near the surface if the growing convective layer penetrates through stable layers above the surface which contain a trapped plume.

In contrast to the sunrise transition, the turbulence burst is an intermittent nocturnal event that occurs as a consequence of hydrodynamic instability within a stably-stratified atmosphere. Businger (1973) offers the following qualitative description of the process in which sporadic turbulence events occur within an otherwise quiescent nocturnal boundary layer. When the Flux Richardson number (Equation (3-14)) exceeds its critical value ($R_f > 0.2$), turbulence is suppressed and laminar layers develop. This stratification interrupts the downward flux of heat and momentum. Near the surface, the winds become calm while winds aloft accelerate because their momentum is not being dissipated toward the surface. The acceleration of wind accompanied by weak heat flux eventually drives R_f below its critical value, whereupon the laminar layers burst into turbulence, creating a sudden exchange of heat and momentum. Quiescent conditions return with the dissipation of this energy and the process repeats itself.

Measurements at DPG during periods with light winds indicate that the nocturnal boundary layer in a high desert environment is more complicated than a series of stratified layers intermittently disturbed by turbulence bursts tripped by a R_f switch. For example, the 20-min time series plots of wind components and speed of sound shown in Figure 14 for Trial P142154 illustrate a quiescent nocturnal light wind period followed by a turbulence burst. The time series show a gradual decay in turbulence level for the first 10 min, followed by a second 10-min period that begins with abrupt perturbations in velocity components and the speed of sound. Statistical summaries for these two successive 10-min time blocks (identified by Julian date and start times 2142205 and 2142215) are presented in Table 7. The turbulence burst is characterized by large increases in the velocity component and temperature variances. This event also caused the TDI to increase by a factor of 3, while the DR remained small due to weak contributions from $\overline{u'T'}$ Quadrants Q2 and Q3. A high TDI combined with a low DR characterizes this turbulence burst as an energetic, shear-driven event.

The turbulence burst that occurred during Trial P142154 had a dramatic effect on propylene gas concentrations measured on the 9-m tower sampling array. High gas concentrations were measured at all tower levels between 2205 and 2215 MDT. The concentration signal abruptly disappeared as the turbulence event began, with the subsequent appearance of only weak, intermittent concentrations for the remainder of the trial. Concentration statistics for Trial P142154 are based primarily on concentrations measurements prior to 2215 MDT. Insufficient concentration measurements were available beyond 2215 MDT to evaluate the turbulence burst effects on the distribution of in-plume concentrations.

x:\p142205d.datU, V, W, and Speed of Sound, M/S

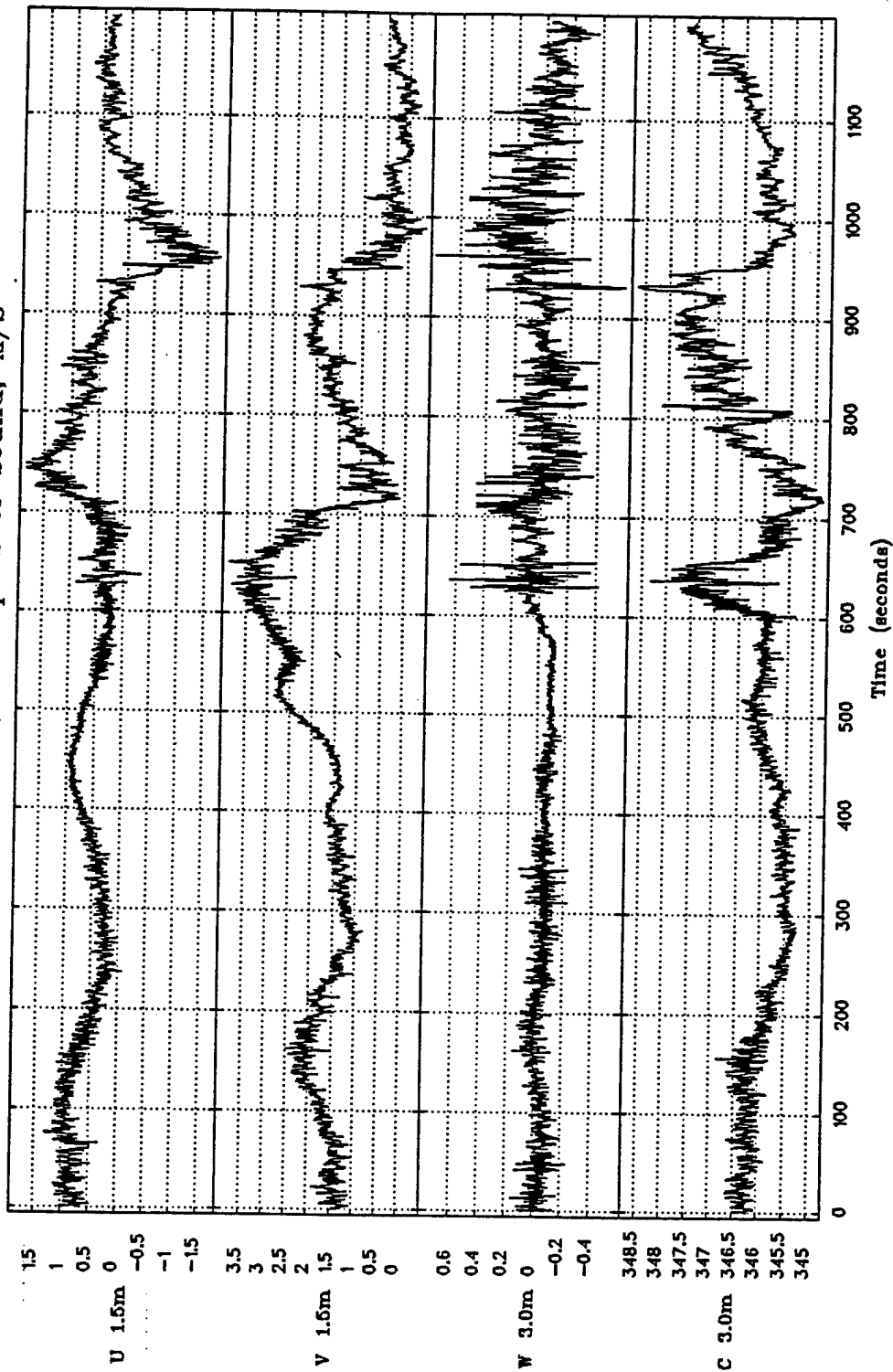


Figure 14. Horizontal (u and v) 1.5-m wind components, the 3.0-m vertical wind component (w), and the 3.0-m speed of sound (C) for two successive 10-min periods illustrating quiescent conditions followed by a turbulence burst during Trial P142154.

The velocity and concentration data taken during Trial P142154 are inconsistent with the intermittent nocturnal turbulence event model described by Businger (1973). An R_f -triggered turbulence event in a vertically stratified, horizontally homogeneous atmosphere would have produced a well-mixed plume concentration field at the tower beginning at 2215 MDT. The large horizontal velocity component perturbations accompanying the disappearance of propylene at the tower suggests a bulk horizontal and/or vertical displacement of the plume rather than a uniform mixing event.

Figure 15 shows a second set of time series plots of wind components and speed of sound for two consecutive 10-min time blocks which illustrate a turbulence burst observed during Trial P150010. Table 7 also gives the statistical summaries for time blocks 2150013 and 2150023. The initial turbulence levels during Trial P150010 were much higher than those observed during Trial P142154, and the stratification was not sufficient to reach the critical R_f . Nevertheless, a turbulence burst characterized by sudden wind field perturbations and large changes in speed of sound occurred, as shown in the second 10-min time block of Figure 15. This event triggered a DR increase from 0.07, indicating virtually no contribution from convection-dominated quadrants, to a value of 0.46. The turbulence level, as indicated by the TDI, also increased by a factor of four. The Businger (1973) turbulence burst model once again fails to fit the observed scenario.

An alternate explanation of the sporadic nocturnal turbulence events observed over the high desert is the collision between pools of air within the nocturnal inversion layer. The high desert nocturnal boundary layer contains shallow pools of air with varying densities that form over source regions with non-uniform cooling characteristics. These pools drift downslope or are advected by the synoptic flow and eventually collide with one another; the distinguishing characteristics of these collisions are the abrupt temperature and velocity component perturbations that occur during the lateral and vertical displacements of the warmer pool by the cooler one. The principal effect of these collisions on nocturnal dispersion is the bulk shearing and/or displacement of any puff or plume material located at pool boundaries. Also, the turbulence generated during collisions dissipates in an intermittent cascade that temporarily accelerates in-plume diffusion.

5.4 TURBULENT MIXING AND CONCENTRATION PDFS

The effects of turbulent mixing on a diffusing cloud are conveniently illustrated by PDF plots. A plot of an instantaneous point-source concentration PDF displays the salient time-independent attributes of the concentration time series. PDF plots from measurements obtained under a range of meteorological conditions at several different positions within dispersing plumes illustrate the height- and stability-dependent effects of turbulent dispersion on the distribution of plume concentrations. Yee et al. (1994) discuss the various shapes that PDF curves can take, depending on the exposure of a dispersing plume to the different turbulence scales and intensities. For example, exponential decay from a prominent peak at zero concentration and an extended tail indicate a poorly-mixed plume exposed to weak small-scale turbulence. Conversely, strong mixing produces a non-zero "shoulder" or secondary peak around χ/C of one (where χ is the instantaneous concentration

x:\p150013.datU, V, W, and Speed of Sound, M/S

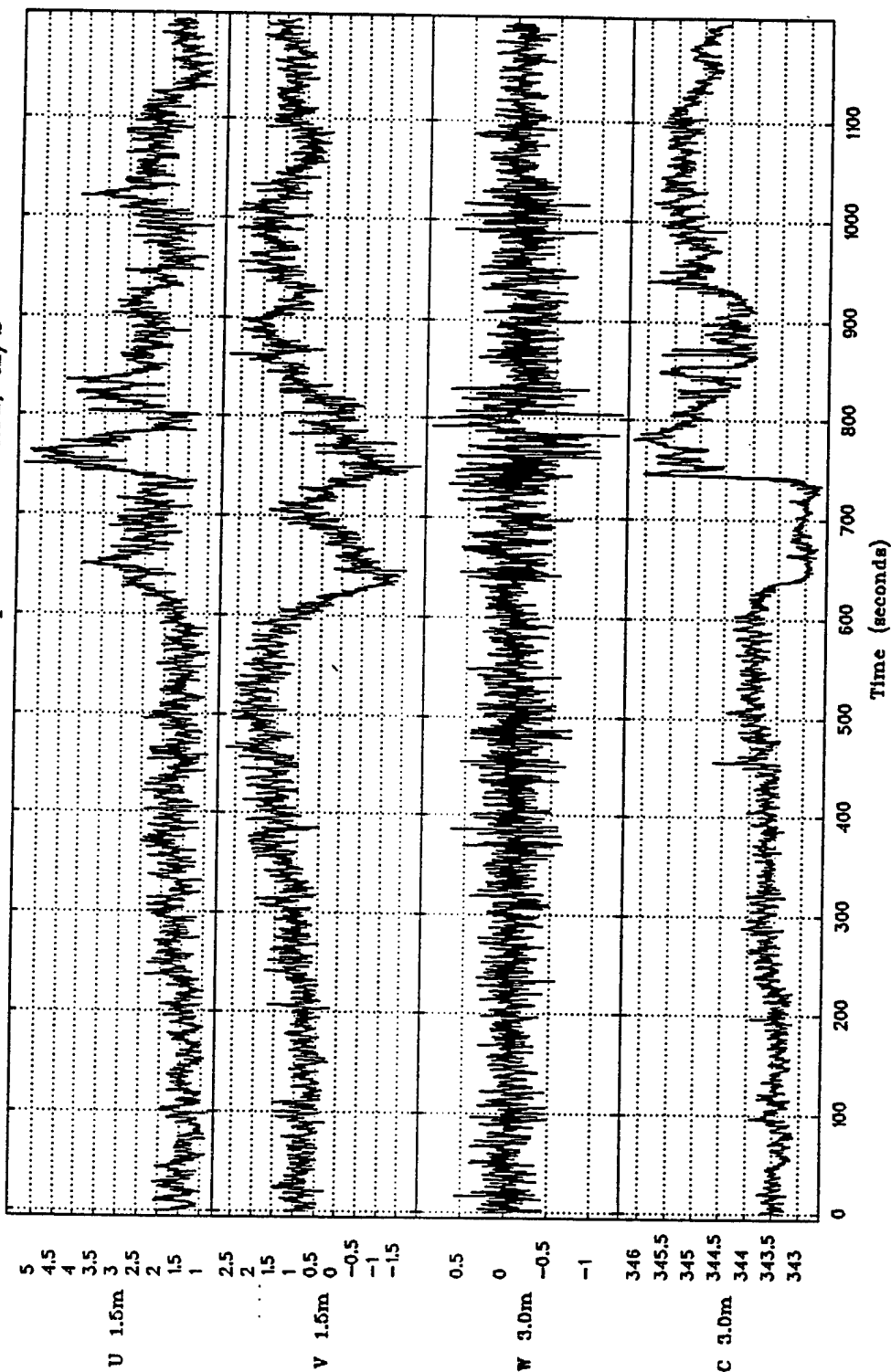


Figure 15. Horizontal (u and v) 1.5-m wind components, the 3.0-m vertical (w) wind components, and the 3.0-m speed of sound (C) for two successive 10-min periods illustrating fully developed nocturnal turbulence followed by a turbulence burst during Trial P150010.

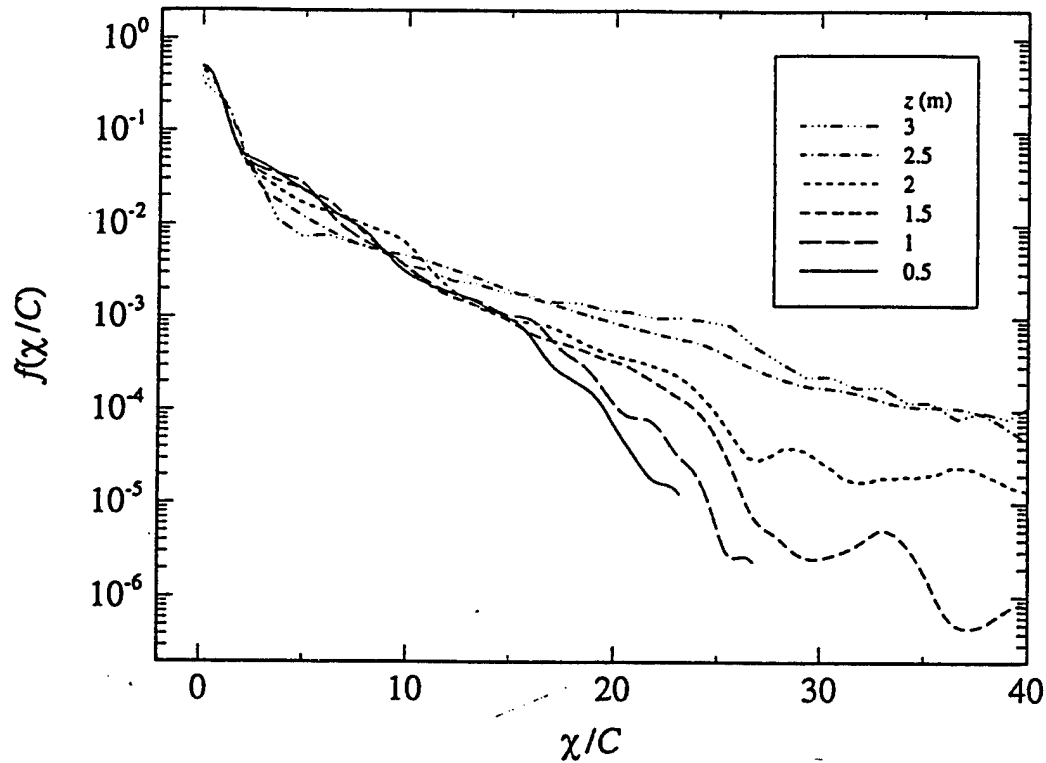
and C is the mean concentration), with a truncated tail due to elimination of high internal plume concentrations. As dispersing material becomes thoroughly mixed, the PDF assumes the shape of a Gaussian distribution centered on a χ/C of one.

The PDFs presented below were derived using a procedure described by Yee et al. (1994). This procedure involves sorting the normalized concentrations, χ/C into histogram bins. Bin counts are then normalized by bin interval and sample size. The result is a PDF of normalized concentration frequency $f(\chi/C)$ plotted against χ/C , as in Figure 16. Each plot contains a set of PDFs from TIP-SJ2 detector measurements made at the indicated heights (0.5 to 3.0 m AGL). Unfortunately, the number of PDF plots available for analysis is small. Four of the available plots plus accompanying wind and turbulence data are discussed below as case studies.

The PDF plots presented in Figure 16 are from Trials P070435 (Figure 16a) and P030745 (Figure 16b). Figure 16a shows an exponential decrease in concentration at all levels, with the long "tails" of high concentrations characteristic of a relatively unmixed plume. The tails are shortest at the lowest level (0.5 m) and increase monotonically with height, reflecting the effect of near-surface mixing, even though the measurements were made at a short (25-m) travel distance from the source. Table 8 provides micrometeorological summaries from two adjacent 10-min time blocks (2070437 and 2070447) within Trial P070435. Turbulence levels within these time blocks, as indicated by the variances and TDI, are fairly typical for the high desert nocturnal boundary layer. The Obukhov length (calculated using σ_w rather than u_*) and DR indicate stable nocturnal conditions with little change from one time block to the other.

In contrast to Figure 16a, the PDFs obtained from concentration detectors nearest the surface on Trial P030743 (Figure 16b) show a "shoulder" developing in the concentration PDFs for the lower measurement levels. This shoulder has a χ/C secondary maximum in the range of 1 to 6, with rapidly diminishing frequency at higher χ/C . PDFs from detectors positioned at higher levels have longer tails and lack the shoulder. This distribution of PDFs occurred during diffusion over a distance of 50 m in a boundary layer in transition, with surface heating inducing incipient convective turbulence at the lowest levels and the higher levels remaining stable. The corresponding micrometeorological summaries in Table 8 include a preconvective 10-min block (2030743) followed by a 10-min block during which convection penetrated to the 1.5-m level (2030753). The change in 1.5-m DR from 0.35 (stable, but approaching neutral) in the first 10-min block to 2.29 (convection-dominated) in the next 10-min block clearly defines a rapid stability progression during the transition. The stability transition at the 6-m level is delayed in time, with a DR of 0.02 (strongly stable) in the first time block increasing to 0.41 (approaching neutral) in the second. Although PDFs from detectors mounted at 6 m are not available, it is evident from the 2.5- and 3.0-m PDF plots in Figure 16b that surface-based convection was not penetrating above the first 2 m. The 3-m Obukhov length L is negative for both time blocks, indicating that the L -derived transition from stable to unstable occurred somewhat earlier than the DR-derived transition.

P070435 [DC13]



P030745 [DC06]

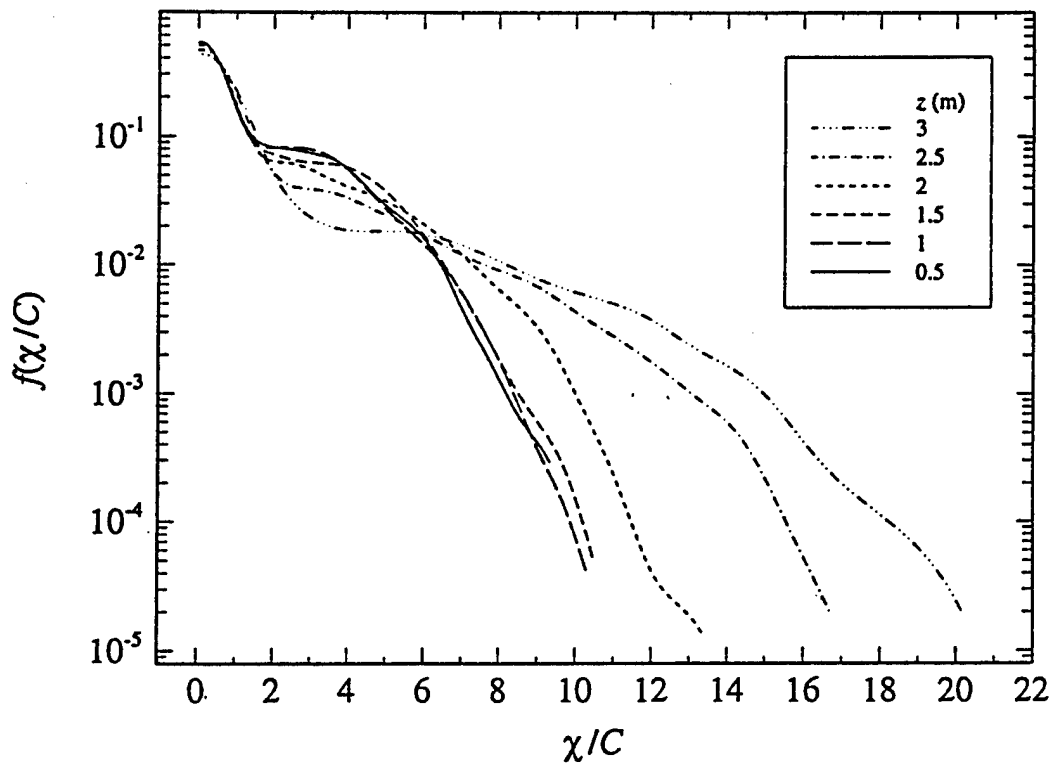


Figure 16. Vertical profiles of the probability density function $f(\chi/C)$ versus χ/C obtained from: (a) Trial P070435; (b) Trial P030745. (PDF plots provided by Dr. Eugene Yee, DRES).

Figure 17 shows a second set of concentration PDFs. These PDFs are for concentration profiles taken during Trials P142154 (Figure 17a) and P150010 (Figure 17b). Trial P142154 is representative of diffusion over a distance of 100 m into a quiescent nocturnal flow that was interrupted by a turbulence burst in mid-trial (see Figure 14). The PDFs in Figure 17a, with their exponential slope and long tail to high χ/C , are similar in appearance to the nocturnal case presented in Figure 16a except for the flatness of the PDF at the 4.0-m level in Figure 17a. The flatness of the 4.0-m PDF for χ/C of 7 to 30 indicates very little internal mixing, which is characteristic of a plume trapped within a quiescent layer. Plume material was present on the tower mainly during the first part of the trial (represented by the 2142205 time period block in Table 7), prior to the turbulence burst. The air pool collision that produced the turbulence also displaced the plume, with only very intermittent weak concentrations occurring at the tower for the remainder of the trial. Consequently, the PDFs in Figure 17a are representative only of diffusion within the quiescent, pre-burst turbulence field.

The micrometeorological summaries shown in Table 7 for the 2142205 and 2142215 time blocks document changes that occurred within a quiescent nocturnal ABL during a turbulence burst. The velocity and temperature variances increase dramatically, reflected by a proportionate TDI increase. The 1.5-m level DR indicates a slight trend from stable (0.10) toward neutral (0.33) during this time. In contrast, the change in Obukhov length at 3.0-m from -0.6 to +1.8 does not accurately reflect stability conditions or the occurrence of a stable case turbulence burst. Again, it is not possible to compare PDFs from pre- and post-turbulence burst conditions because the plume was displaced away from the tower as a consequence of this event.

In contrast to Figure 17a, Figure 17b (Trial P150010) shows PDFs for diffusion over a 100 m distance into a stable boundary layer with initial turbulence levels similar to those of Trial P070435. Turbulence levels for Trial P150010 are represented by the initial 10-min period beginning at 2150013, followed by an abrupt turbulence increase at 2150023 (see Table 7 and Figure 15). As in Trial P142154, the turbulence event displaced the plume away from the tower. Consequently, the available PDFs are most representative of diffusion into the pre-event nocturnal ABL. Turbulence levels during this trial were relatively high from the beginning, as indicated by the well mixed PDFs at the 0.5-, 1.0-, and 2.0-m levels. Surface-generated turbulence apparently diminished rapidly with height, leaving a 4-m PDF indicative of a relatively poorly mixed plume.

The Trial P150010 turbulence event beginning at 2150023 produced turbulence statistics comparable to the statistics obtained for the turbulence event of Trial P142154. The Trial P150010 1.5-m DR responded in a similar fashion to that of Trial P142154 by increasing from 0.02 to 0.44 as a consequence of the turbulence event. The Obukhov length again provided no useful indication of the increase in turbulence between the 2150013 and 2150023 time periods.

Table 8. Micrometeorological Summaries for Selected 10-min Time Blocks Within Trials P030743, P070435, P142154, and P150010.

Ht	Variable	Units	Date/Time, JJJHHMM											
			P030743				P070435				P142154			
			2030743	2030753	2070437	2070447	2142205	2142215	2150013	2150023	2150010			
1.5-m	WS	m/s	1.8	2.7	2.2	1.6	1.9	1.4	2.0	2.8				
6.0-m	WS	m/s	2.0	3.1	3.2	2.3	2.1	1.5	3.0	3.4				
1.5-m	HD	Deg	200	213	220	201	169	166	202	219				
6.0-m	HD	Deg	203	216	228	219	179	155	200	224				
1.5-m	σ_u	m/s	0.413	0.432	0.535	0.408	0.497	1.027	0.451	0.572				
6.0-m	σ_u	m/s	0.473	0.387	0.570	0.545	0.165	0.696	0.499	0.642				
1.5-m	σ_v	m/s	0.353	0.501	0.369	0.323	0.310	0.579	0.362	0.900				
6.0-m	σ_v	m/s	0.313	0.443	0.389	0.293	0.238	0.825	0.462	1.052				
3.0-m	σ_w	m/s	0.178	0.206	0.231	0.157	0.046	0.149	0.157	0.228				
9.0-m	σ_w	m/s	M*	M	0.274	0.197	0.071	0.257	0.153	0.374				
1.5-m	σ_T	Deg K	0.362	0.459	0.405	0.424	0.535	1.281	0.407	1.484				
6.0-m	σ_T	Deg K	0.266	0.384	0.308	0.323	0.231	0.972	0.474	1.630				
3.0-m	w'T'	K m/s	+0.235	+0.281	-0.273	-0.178	+0.048	-0.0616	-0.160	-0.0501				
9.0-m	w'T'	K m/s	M	M	-0.320	-0.117	-0.042	-0.0778	-0.150	-0.1649				
3.0-m	L	m	-8.2	-10.7	+15.4	+22.1	-0.6	+1.8	+8.3	+8.2				
9.0-m	L	m	M	M	+7.4	+22.5	+2.9	+7.6	+8.3	+11.0				
1.5-m	DR	ND	0.35	2.29	0.08	0.13	0.10	0.33	0.02	0.44				
6.0-m	DR	ND	0.02	0.41	0.16	0.06	0.36	0.36	0.05	0.56				
1.5-m	TDI	K m/s	.0847	.1228	.1682	.1295	.1915	.9211	.1535	.5377				
6.0-m	TDI	K m/s	.0888	.0907	.1273	.1456	.0266	.4061	.1918	.6316				

*M = Missing Data

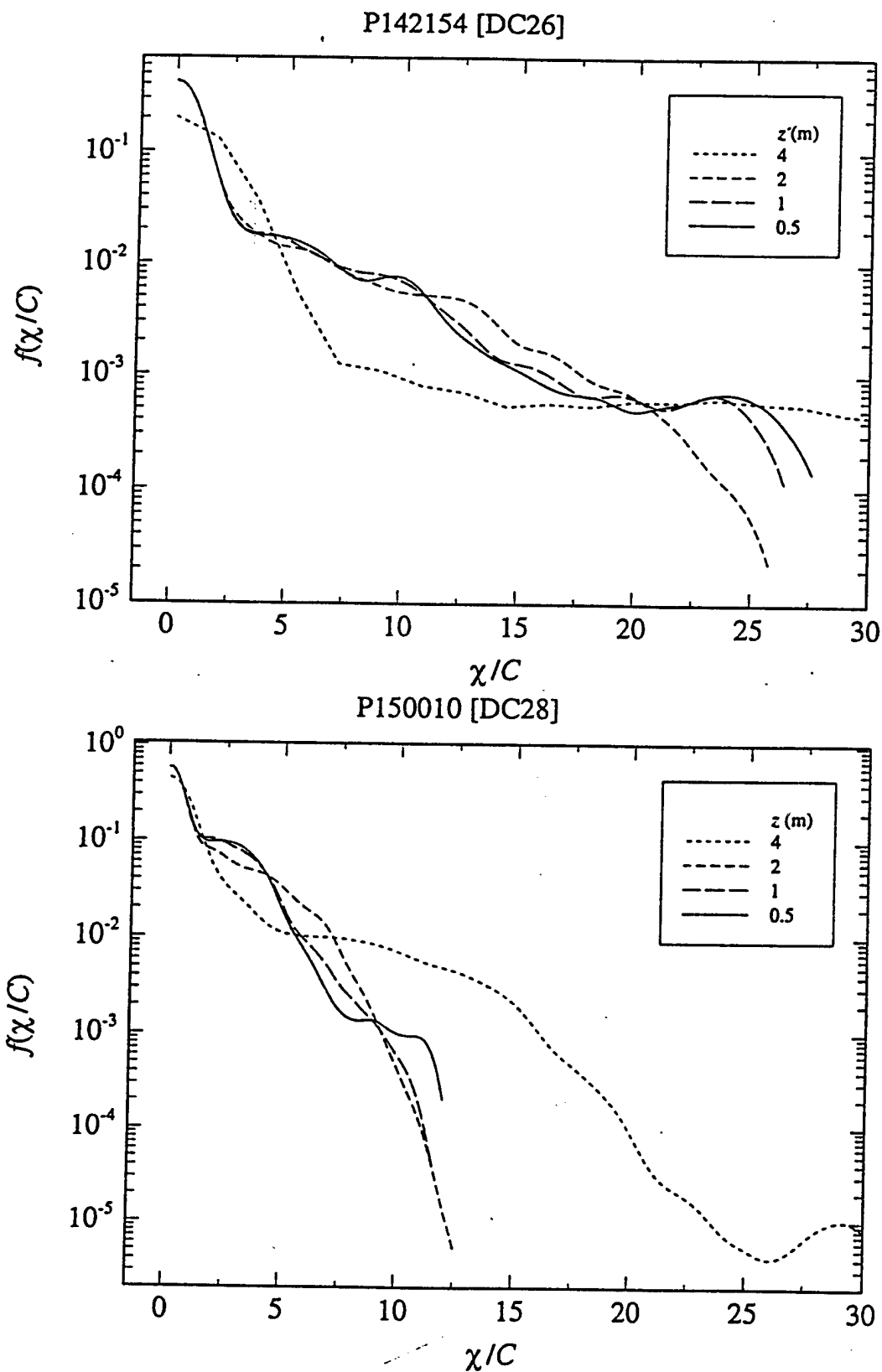


Figure 17. Vertical profiles of the normalized probability density function $f(\chi/C)$ versus χ/C obtained from (a) Trial P142154; (b) Trial P150010. (PDF plots provided by Dr. Eugene Yee, DRES).

SECTION 6. CONCLUSIONS AND RECOMMENDATIONS

Improved measurement and analysis techniques are beginning to reveal the detailed physics of atmospheric dispersion processes that heretofore have been subject to guesswork and gross parameterizations. In particular, the study of dispersion near surfaces has been hindered by the absence of measurement techniques able to resolve small-scale processes in an environment characterized by strong gradients and non-steady fluxes of heat and momentum. This region is currently beyond the reach of numerical modeling techniques that are successfully resolving larger scale atmospheric motions. The Evaporation, Recirculation, and Dispersion in Light Winds Dispersion test: (1) generated data bases for validating evaporation and recirculation models, and (2) provided a first look into the physics of some near-surface high Reynolds number processes. Much work remains to achieve a clear understanding of these processes.

The Evaporation Subtest provided a valuable data set detailing the effects of droplet size, thickener concentration, and surface porosity on the evaporation of the chemical agent simulants DEM and MES. A detailed description of the Evaporation Subtest and an evaluation of subsequent modeling results is provided by Roberts (1996). Roberts' evaluation of an analytical droplet evaporation prediction model found good initial results, but a general evaporation rate overprediction with increasing evaporation time.

The Recirculation Subtest characterized flow around a simple bluff body and the dissipation of windborne tracer gas in its wake. Existing recirculation region contaminant accumulation models were evaluated. Principal conclusions are: (1) wake width is a more pertinent dimension than obstacle width, and (2) stability has minimal effect on the properly non-dimensionalized residence time. Mavoridis (1997) uses these and related study results to develop improved urban dispersion model algorithms.

Analyses of turbulence and dispersing gas concentration profiles within the buffer and inertial sublayers have revealed some of the physics of important non-steady processes such as the transition through sunrise and the nocturnal turbulence burst. Fourier and $\overline{u'T'}$ covariance quadrant analyses were found to provide useful insights into these non-steady processes. The transition through sunrise was examined in detail to determine how the atmosphere evolves from a stable nocturnal state to a state of convection. The adiabatic condition, with no vertical exchange of heat, often has been presumed to exist during this transition. However, rather than existing in a true adiabatic state, the desert atmosphere in transition occurs when there is a net balance between eddies transporting heat to and from the surface. An intense near-surface convective layer develops after sunrise and works against the trapping inversion lid. This depiction of boundary layer transition differs profoundly from the well mixed adiabatic model that pertains to regions like Northern Europe. The desert transition pattern implies that vigorous mixing can occur within confined layers, creating transient episodes of high ground-level pollutant concentrations from plumes trapped in elevated stable layers. Similar analyses of the sunset transition are needed to complete the description of these non-steady processes.

The lack of satisfactory similarity characterization of the non-steady lower portion of the surface boundary layer led to the development of two new indices, the Diabatic Ratio (DR) and the Total Diabatic Influence (TDI). DR, the ratio of convective to shear-driven turbulence, is a stability indicator, while TDI provides an estimate of the magnitude of vertical turbulent motions. Both indices are needed to adequately describe the turbulent state of the surface boundary layer.

DR and TDI appear to be more robust indicators than Obukhov length L , particularly with light winds and non-steady conditions within the lower portion of the surface boundary layer. An advantage offered by the methods used to compute DR and TDI is that they do not involve the summing of positive and negative quantities required for flux computations. The result of algebraically summing positive and negative covariance contributions is a flux that is often small in comparison with its uncertainty. Using a ratio (the DR) or an absolute sum (the TDI) of covariance quadrant contributions creates indices that are relatively large and tractable, while remaining physically relevant. These indices offer the added advantage that they can be easily computed in an operational setting using near-surface measurements of the horizontal wind and temperature components from a 2-axis sonic anemometer/thermometer. DR and TDI appear to be statistically stable when computed over averaging periods on the order of 10 min. Thus, they could provide near real-time estimates of the turbulent state of the surface boundary layer in an operational setting. These proposed indices are not presently supported by boundary layer theory, and they have not been subject to independent testing. Further investigations, to include development of a supporting theory and applications testing, are needed to determine their overall usefulness as surface layer stability and turbulence indicators.

SECTION 7. APPENDICES

APPENDIX A. CONSOLIDATED TIP-SJ AND MICROMETEOROLOGICAL DATA

The statistical summaries presented in Appendix A were obtained from sonic anemometer/thermometers and TIPSJ2 photoionization detectors mounted on a 9-m tower at the indicated distances downwind from a continuous point source of propylene. The trial name convention is JJJHHMM, where JJJ is the Julian date and HHMM is the nominal trial start time (MDT). The actual trial start and end times are given in Universal Coordinated Time (UTC). Wind component, sonic temperature statistics, and temperature profiles are presented in the top half of each summary page. The covariance quadrant table includes $\overline{u'T'}$ covariance components for the 1.5- and 6-m levels, and $\overline{w'T'}$ covariance components for the 3- and 9-m levels. With the exception of skewness and kurtosis, all of the u and v statistics were computed after coordinate rotation into the mean wind. Below the micrometeorological summary is a profile plot of peak and mean concentrations, normalized by the highest profile mean concentration. Concentration profile data are tabulated to the right of the plot. Trial concentration data were provided by Dr. Eugene Yee of DRES.

Trial: P020550 Micrometeorological and Concentration Data Summary Date: 21 July 1995

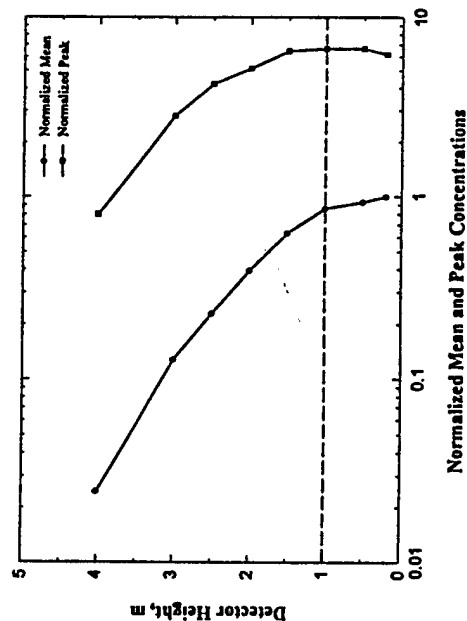
Source Distance: 25 m Source Height: 1.0 m Peak Concentration Ratio: 6.69

Time (UTC): 0552 to 0627 Obukhov Length (m): ND Temperature (°C) 0-m: 19.5* 0.5-m: 19.6* 2.0-m: 19.6*

Means				Variances				Skewness			
Height (m)	WS (m/s)	HD (Deg)	σ_θ (Deg)	w (m/s)	$u'u'$ (m^2/s^2)	$v'v'$ (m^2/s^2)	$w'w'$ (m^2/s^2)	$T'T'$ (Deg K) ²	S_u	S_v	S_e
1.5	ND	ND	ND	---	ND	ND	---	ND	ND	ND	ND
3.0	ND	ND	ND	ND	ND	ND	ND	ND	ND	ND	ND
6.0	ND	ND	ND	---	ND	ND	---	ND	ND	ND	ND
9.0	ND	ND	ND	ND	ND	ND	ND	ND	ND	ND	ND

Kurtosis				Covariances Correlations				Covariance Quadrants			
Height (m)	K_u	K_v	K_w	K_e	$w'T'$	$u'T'$	$w'w'$ (m^2/s^2)	$u'u' > 0$ $T' > 0$	$w'u' > 0$ $T' < 0$	$w'u' < 0$ $T' > 0$	$w'u' < 0$ $T' < 0$
1.5	ND	ND	---	ND	---	ND	---	ND	ND	ND	ND
3.0	ND	ND	ND	ND	ND	ND	ND	ND	ND	ND	ND
6.0	ND	ND	---	ND	---	ND	---	ND	ND	ND	ND
9.0	ND	ND	ND	ND	ND	ND	ND	ND	ND	ND	ND

*Single point estimate
ND = No Data



z	C	i	C_{pk}
4.0	1.02	8.87	33.20
3.0	5.28	4.41	115.54
2.5	9.482	3.43	174.25
2.0	16.42	2.66	213.35
1.5	26.18	2.22	268.81
1.0	35.64	1.88	276.65
0.5	38.74	1.71	276.84
0.25	41.37	1.65	256.53

Trial: P020635

Micrometeorological and Concentration Data Summary

Date: 21 July 1995

Source Distance: 50 m Source Height: 1.0 m Peak Concentration Ratio: 15.79

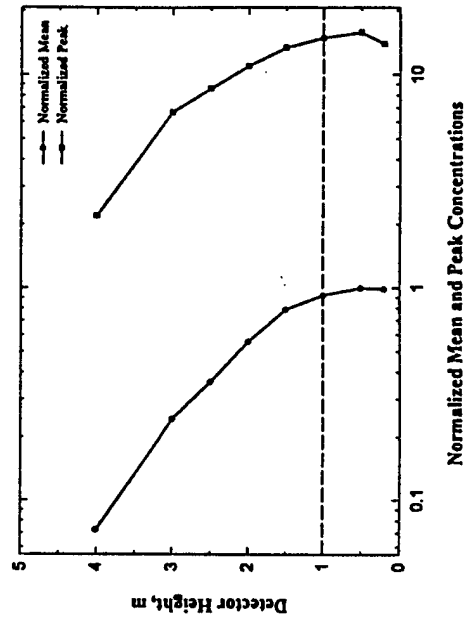
Time (UTC): 1244 to 1319 Obukhov Length (m): +53 Temperature (°C) 0-m: 16.5* 0.5-m: 16.7* 2.0-m: 16.9*

Height (m)	Means				Variances				Skewness			
	WS (m/s)	HD (Deg)	$\sigma\theta$ (Deg)	w (m/s)	u'u' (m ² /s ²)	v'v' (m ² /s ²)	w'w' (m ² /s ²)	T'T' (Deg K) ²	S _u	S _v	S _w	S _{θ}
1.5	2.2	206	19.6	---	0.398	0.613	---	0.109	0.53	-0.45	---	-0.22
3.0	ND	ND	ND	-0.04	ND	ND	0.033	---	ND	ND	-0.17	-0.38
6.0	2.9	208	18.3	---	0.471	0.875	---	0.064	0.30	-0.52	---	-0.64
9.0	ND	ND	ND	ND	ND	ND	ND	ND	ND	ND	0.23	-0.72

Height (m)	Kurtosis				Covariances Correlations				Covariance Quadrants			
	K _u	K _v	K _w	K _{θ}	w'T' $\sigma_w\sigma_T$	u'T' $\sigma_u\sigma_T$	w'T' $\sigma_w\sigma_T$	u'T' $\sigma_u\sigma_T$	w'u'>0 T'>0	w'u'>0 T'<0	w'u'<0 T'>0	w'u'<0 T'<0
1.5	2.78	2.35	---	1.95	---	.1549	---	+0.75	.0782	-.0008	-.0034	.0808
3.0	ND	ND	4.30	2.30	-.0049	ND	-.09	ND	.0092	-.0062	-.0115	.0037
6.0	2.48	2.23	---	3.12	---	.1028	---	+0.59	.0474	-.0063	-.0050	.0665
9.0	ND	ND	4.30	3.56	-.0043	ND	-.08	ND	.0062	-.0066	-.0100	.0060

*Single point estimate

ND = No Data



z	C	i	C _{pk}
4.0	0.93	6.24	28.21
3.0	3.12	4.76	85.14
2.5	4.62	4.26	110.13
2.0	7.13	3.50	140.14
1.5	10.13	3.25	171.14
1.0	11.80	3.10	189.64
0.5	12.79	3.02	201.96
0.25	12.68	2.80	178.83

Trial: P020720

Micrometeorological and Concentration Data Summary

Date: 21 July 1995

Source Distance: 50 m Source Height: 1.0 m Peak Concentration Ratio: 16.8

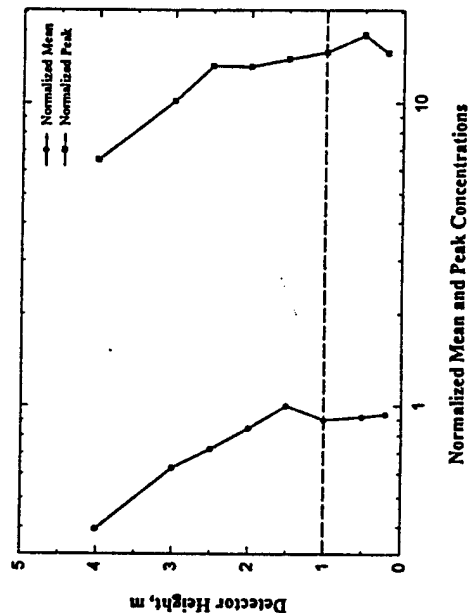
Time (UTC): 1325 to 1400 Obukhov Length (m): -8. Temperature (°C) 0-m: 23.1* 0.5-m: 20.5* 2.0-m: 20.2*

Means				Variances					Skewness			
Height (m)	WS (m/s)	HD (Deg)	$\sigma\theta$ (Deg)	w (m/s)	$u'u'$ (m ² /s ²)	$v'v'$ (m ² /s ²)	$w'w'$ (m ² /s ²)	$T'T'$ (Deg K) ²	S_u	S_v	S_w	S_θ
1.5	1.0	203	39.5	---	0.263	0.352	---	0.260	0.10	-0.01	---	-0.19
3.0	ND	ND	ND	-0.02	ND	ND	0.024	0.193	ND	ND	0.21	-0.16
6.0	1.1	211	39.1	---	0.305	0.478	---	0.205	0.19	0.33	---	-0.74
9.0	ND	ND	ND	0.20	ND	ND	0.037	ND	ND	ND	0.33	ND

Kurtosis				Covariances Correlations				Covariance Quadrants				
Height (m)	K_u	K_v	K_w	K_θ	$w'T'$	$u'T'$	$w'w'$ $\sigma_u\sigma_T$	$u'T'$ $\sigma_u\sigma_T$	$w'u' > 0$ $T' > 0$	$w'u' > 0$ $T' < 0$	$w'u' < 0$ $T' > 0$	$w'u' < 0$ $T' < 0$
1.5	2.24	2.33	---	3.29	---	-1.005	---	-0.38	.0320	-0.0694	-0.0666	.0034
3.0	ND	ND	4.02	3.71	.0150	ND	+0.22	ND	.0176	-0.0069	-0.0056	.0099
6.0	2.05	2.47	---	2.86	---	-0.0873	---	-0.35	.0357	-0.0647	-0.0604	.0022
9.0	ND	ND	3.99	ND	ND	ND	ND	ND	ND	ND	ND	ND

*Single point estimate

ND = No Data



Trial: P030545 Micrometeorological and Concentration Data Summary Date: 22 July 1995
Source Distance: 50 m Source Height: 1.0 m Peak Concentration Ratio:
Time (UTC): 1146 to 1159 Obukhov Length (m): +2. Temperature (°C) 0-m: 12.9 0.5-m: 13.3 2.0-m: 13.6

Height (m)	Means				Variances				Skewness			
	WS (m/s)	HD (Deg)	$\sigma\theta$ (Deg)	w (m/s)	u'u' (m ² /s ²)	v'v' (m ² /s ²)	w'w' (m ² /s ²)	T'T' (Deg K) ²	S _u	S _v	S _w	S _e
1.5	1.0	204	15.9	---	0.043	0.062	---	0.087	-0.58	-0.67	---	+0.05
3.0	1.6	219	11.2	-0.01	ND	ND	0.005	0.098	ND	ND	+0.16	+0.38
6.0	2.1	216	6.5	---	0.051	0.057	---	0.312	-0.48	-0.95	---	-0.10
9.0	ND	ND	ND	ND	ND	ND	ND	ND	ND	ND	ND	ND

Height (m)	Kurtosis				Covariances				Correlation				Covariance Quadrants			
	K _u	K _v	K _w	K _e	w'T'	u'T'	$\frac{w'T'}{\sigma_w\sigma_T}$	$\frac{u'T'}{\sigma_u\sigma_T}$	$\frac{w'T'}{\sigma_w\sigma_T}$	$\frac{u'T'}{\sigma_u\sigma_T}$	$\frac{w'u'}{\sigma_w\sigma_T}$	$\frac{u'u'}{\sigma_u\sigma_T}$	w'u'>0 T'>0	w'u'>0 T'<0	w'u'<0 T'>0	w'u'<0 T'<0
1.5	3.98	4.71	---	3.23	---	.0402	---	+0.66	.0187	-.0029	-.0010	.0253				
3.0	ND	ND	4.42	3.86	-.0072	ND	-0.33	ND	.0017	-.0049	-.0054	.0015				
6.0	3.27	4.39	---	2.22	---	.0882	---	+0.70	.0439	-.0022	-.0040	.0505				
9.0	ND	ND	ND	ND	ND	ND	ND	ND	ND	ND	ND	ND				

ND = No Data

z	c	i	C _{pk}
4.0			
3.0			
2.5			
2.0			
1.5			
1.0			
0.5			
0.25			

(Insufficient Data)

Trial: P030646 Micrometeorological and Concentration Data Summary Date: 22 July 1995

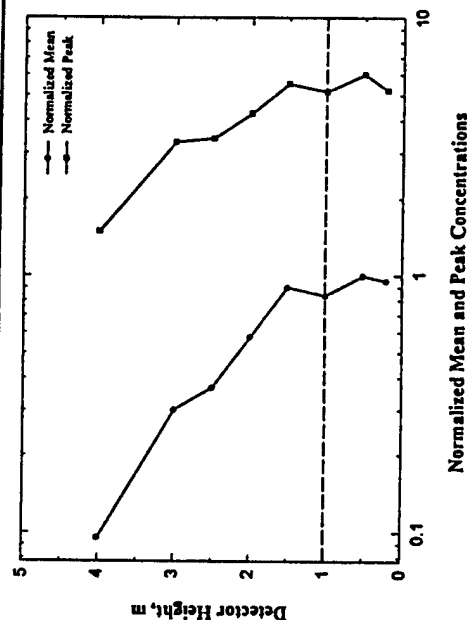
Source Distance: 50 m Source Height: 1.0 m Peak Concentration Ratio: 6.03

Time (UTC): 1245 to 1315 Obukhov Length (m): -8. Temperature (°C) 0-m: 13.2 0.5-m: 13.9 2.0-m: 13.8

Means			Variances				Skewness		
Height (m)	WS (m/s)	HD (Deg)	$\sigma\theta$ (Deg)	w (m/s)	$u'u'$ (m ² /s ²)	$v'v'$ (m ² /s ²)	$w'w'$ (m ² /s ²)	$T'T'$ (Deg K) ²	S_u S_v S_w S_t
1.5	1.3	212	21.1	---	0.173	0.160	---	0.271	-0.09 +0.62 --- +0.02
3.0	1.7	221	20.4	-0.02	ND	ND	0.028	0.236	ND ND -0.02 -0.10
6.0	1.8	217	15.6	---	0.344	0.136	---	0.181	-0.21 +0.49 --- -0.24
9.0	ND	ND	ND	ND	ND	ND	ND	ND	ND ND ND ND

Kurtosis			Covariances Correlations				Covariance Quadrants			
Height (m)	K_u	K_v	K_w	K_c	$w'T'$	$u'T'$	$w'w'$ $\sigma_w\sigma_T$	$u'T'$ $\sigma_u\sigma_T$	$w'u' > 0$ $T' > 0$	$w'u' < 0$ $T' < 0$
1.5	3.26	2.75	---	1.62	---	.0876	---	+0.40	.0741 -0.080	-.0315 .0529
3.0	ND	ND	4.83	1.58	.0183	ND	+0.23	ND	.0320 -.0064	-.0126 .0052
6.0	2.63	2.68	---	1.70	---	.0574	---	+0.23	.0759 -.0126	-.0536 .0478
9.0	ND	ND	ND	ND	ND	ND	ND	ND	ND ND	ND ND

ND = No Data

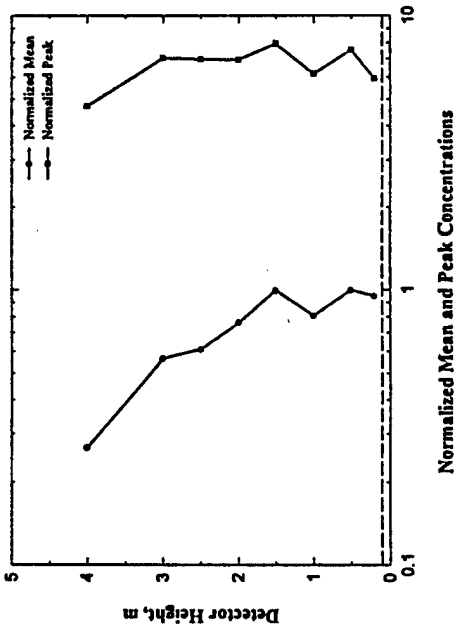


z	C	i	C _{pk}
4.0	1.61	2.98	25.26
3.0	5.08	2.29	55.90
2.5	6.21	2.02	57.55
2.0	9.74	1.78	71.89
1.5	15.24	1.64	93.86
1.0	14.12	1.57	87.42
0.5	16.89	1.57	101.93
0.25	16.11	1.46	88.33

Trial: P030745 Micrometeorological and Concentration Data Summary Date: 22 July 1995
 Source Distance: 50 m Source Height: 0.05 m Peak Concentration Ratio: 7.94
 Time (UTC): 1343 to 1413 Obukhov Length (m): -9. Temperature (°C) 0-m: 17.9 0.5-m: 20.2 2.0-m: 19.2

Height (m)	Means				Variances				Skewness			
	WS (m/s)	HD (Deg)	$\sigma\theta$ (Deg)	w (m/s)	u'u' (m ² /s ²)	v'v' (m ² /s ²)	w'w' (m ² /s ²)	T'T' (Deg K) ²	S _u	S _v	S _w	S _{ϵ}
1.5	2.3	210	13.1	---	0.355	0.228	---	0.718	-0.26	-0.20	---	+0.21
3.0	2.5	213	13.1	-0.01	ND	ND	0.042	0.767	ND	ND	+0.36	+0.19
6.0	2.7	213	11.8	---	0.664	0.468	---	0.873	-0.56	-0.24	---	+0.27
9.0	ND	ND	ND	ND	ND	ND	ND	ND	ND	ND	ND	ND

Height (m)	Kurtosis				Covariances Correlations				Covariance Quadrants			
	K _u	K _v	K _w	K _{ϵ}	w'T'	u'T'	w'w' $\sigma_w\sigma_T$	u'T' $\sigma_u\sigma_T$	w'u'>0 T'>0	w'u'>0 T'<0	w'u'<0 T'>0	w'u'<0 T'<0
1.5	2.35	2.52	---	1.86	---	.2289	---	+0.45	.1064	-.0323	-.0389	.1938
3.0	ND	ND	3.41	1.83	.0327	ND	+0.18	ND	.0481	-.0180	-.0280	.0305
6.0	2.50	2.46	---	1.86	---	.3198	---	+0.55	.1257	-.0235	-.0283	.2460
9.0	ND	ND	ND	ND	ND	ND	ND	ND	ND	ND	ND	ND



ND = No Data

Trial: P030845

Micrometeorological and Concentration Data Summary

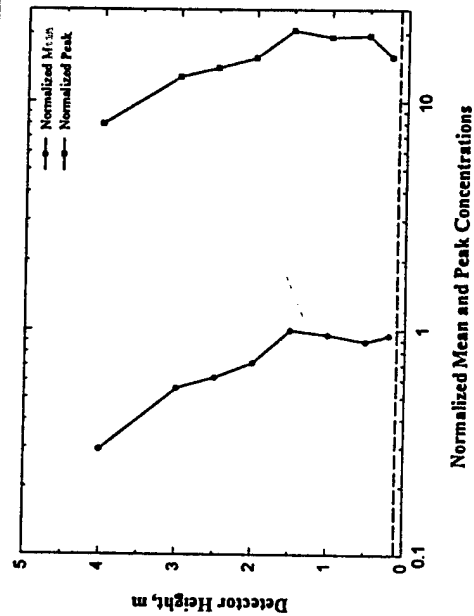
Date: 22 July 1995

Source Distance: 25 m Source Height: 0.05 m Peak Concentration Ratio: 20.66

Time (UTC): 1445 to 1518 Obukhov Length (m): -6. Temperature (°C) 0-m: 33.6 0.5-m: 25.5 2.0-m: 24.0

Height (m)	Means				Variances				Skewness			
	WS (m/s)	HD (Deg)	σ_θ (Deg)	w (m/s)	u'u' (m ² /s ²)	v'v' (m ² /s ²)	w'w' (m ² /s ²)	T'T' (Deg K) ²	S _u	S _v	S _w	S _{ϵ}
1.5	1.0	198	52.7	---	0.407	0.299	---	0.476	-0.14	-0.20	---	+0.42
3.0	1.0	199	53.0	0.00	ND	ND	0.053	0.269	ND	ND	+0.12	+0.62
6.0	1.0	212	52.9	---	0.433	0.348	---	0.361	-0.06	+0.12	---	+0.13
9.0	ND	ND	ND	ND	ND	ND	ND	ND	ND	ND	ND	ND
Height (m)	Kurtosis				Covariances Correlations				Covariance Quadrants			
	K _u	K _v	K _w	K _{ϵ}	w'T'	u'T'	w'w' $\sigma_u\sigma_T$	u'T' $\sigma_u\sigma_T$	w'u'>0 T'>0	w'u'>0 T'<0	w'u'<0 T'>0	w'u'<0 T'<0
1.5	2.74	2.75	---	2.82	---	-0.831	---	-0.19	.0496	-0.1075	-0.0719	.0467
3.0	ND	ND	3.12	3.31	.0686	ND	0.51	ND	.0466	-0.0065	-0.0066	.0280
6.0	2.55	2.43	---	2.48	---	-0.662	---	-0.18	.0470	-0.1084	-0.0728	.0458
9.0	ND	ND	ND	ND	ND	ND	ND	ND	ND	ND	ND	ND

ND = No Data



z	C	i	C _{pk}
4.0	1.59	5.72	42.68
3.0	2.97	4.46	69.30
2.5	3.31	4.02	75.68
2.0	3.86	4.19	84.10
1.5	5.37	4.28	110.90
1.0	5.13	4.14	103.57
0.5	4.79	3.97	105.24
0.25	5.10	3.13	84.81

Trial: P060530 Micrometeorological and Concentration Data Summary Date: 25 July 1995

Source Distance: 25 m Source Height: 0.05 m Peak Concentration Ratio: ND
 Time (UTC): 1128 to 1143 Obukhov Length (m): +0.1 Temperature (°C) 0-m: 10.8 0.5-m: 10.9 2.0-m: 11.8

Height (m)	Means				Variances				Skewness			
	WS (m/s)	HD (Deg)	$\sigma\theta$ (Deg)	w (m/s)	u'u' (m ² /s ²)	v'v' (m ² /s ²)	w'w' (m ² /s ²)	T'T' (Deg K) ²	S _u	S _v	S _w	S _{θ}
1.5	1.7	167	12.8	---	.180	.134	---	0.746	-.03	-.09	---	0.75
3.0	ND	ND	ND	-0.02	ND	ND	.002	2.163	ND	ND	0.29	-0.78
6.0	2.6	175	7.5	---	.119	.113	---	0.123	-.07	-.08	---	-0.04
9.0	ND	ND	ND	ND	ND	ND	ND	0.049	ND	ND	ND	-0.47

Height (m)	Kurtosis				Covariances Correlations				Covariance Quadrants			
	K _u	K _v	K _w	K _{θ}	w'T'	u'T'	w'w' $\sigma_w\sigma_T$	u'T' $\sigma_u\sigma_T$	w'u'>0 T'>0	w'u'>0 T'<0	w'u'<0 T'>0	w'u'<0 T'<0
1.5	2.10	1.95	---	4.05	---	.3080	---	0.84	.1699	-.0054	-.0014	.1450
3.0	ND	ND	6.09	2.61	-.0210	ND	-.34	ND	.0016	-.0147	-.0087	.0034
6.0	2.16	2.33	---	2.39	---	.0042	---	-0.04	.0192	-.0247	-.0166	.0263
9.0	ND	ND	ND	2.75	ND	ND	ND	ND	ND	ND	ND	ND

ND = No Data

z	C	i	C _{pk}
4.0			
3.0			
2.5			
2.0			
1.5			
1.0			
0.5			
0.25			

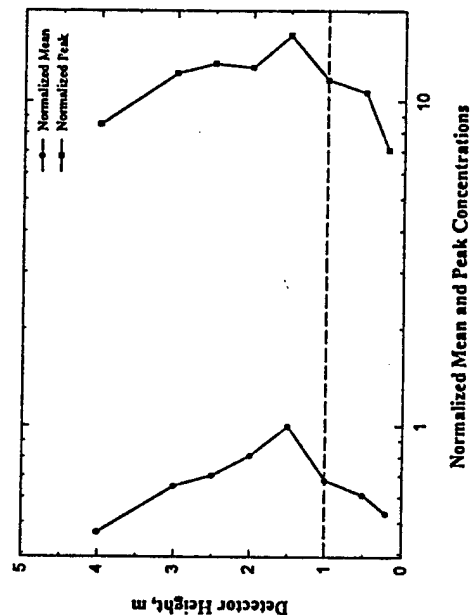
(Insufficient Data)

Trial: P060805 Micrometeorological and Concentration Data Summary Date: 25 July 1995
Source Distance: 25 m Source Height: 1.0 m Peak Concentration Ratio: 16.08
Time (UTC): 1408 to 1426 Obukhov Length (m): -7. Temperature (°C) 0-m: 21.9 0.5-m: 23.1 2.0-m: 21.9

Means				Variances				Skewness				
Height (m)	WS (m/s)	HD (Deg)	$\sigma\theta$ (Deg)	w (m/s)	$u'u'$ (m ² /s ²)	$v'v'$ (m ² /s ²)	$w'w'$ (m ² /s ²)	$T'T'$ (Deg K) ²	S_u	S_v	S_w	S_ϵ
1.5	0.8	139	24.9	---	0.064	0.097	---	0.130	0.29	0.48	---	0.42
3.0	ND	ND	ND	-0.01	ND	ND	0.031	0.098	ND	ND	0.13	0.42
6.0	0.7	135	30.4	---	0.075	0.108	---	0.098	-0.01	0.65	---	0.26
9.0	ND	ND	ND	ND	ND	ND	ND	0.115	ND	ND	ND	0.20

Kurtosis				Covariances Correlations				Covariance Quadrants				
Height (m)	K_u	K_v	K_w	K_ϵ	$w'T'$	$u'T'$	$w'w'$ $\sigma_u\sigma_T$	$u'T'$	$w'u'>0$ $T'>0$	$w'u'>0$ $T'<0$	$w'u'<0$ $T'>0$	$w'u'<0$ $T'<0$
1.5	3.21	3.27	---	2.90	---	-0.272	---	-0.30	.0110	-0.0207	-0.0230	.0055
3.0	ND	ND	2.80	3.24	.0221	ND	0.40	ND	.0193	-0.0032	-0.0038	.0097
6.0	2.82	3.18	---	3.05	---	-0.301	---	-0.35	.0101	-0.0226	-0.0215	.0039
9.0	ND	ND	ND	2.87	ND	ND	ND	ND	ND	ND	ND	ND

ND = No Data

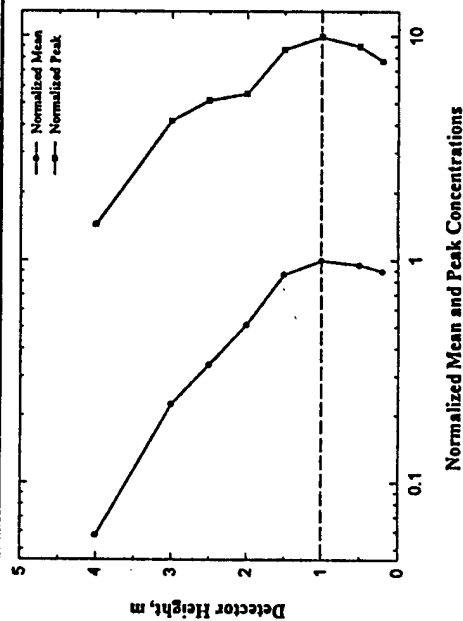


z	C	i	C _{pk}
4.0	3.42	3.59	62.28
3.0	4.76	4.29	89.43
2.5	5.14	4.12	95.93
2.0	5.92	3.62	93.27
1.5	7.33	3.28	117.88
1.0	4.97	3.35	85.39
0.5	4.47	3.63	77.92
0.25	3.91	3.14	51.88

Trial: P070435 Micrometeorological and Concentration Data Summary Date: 26 July 1995
 Source Distance: 25 m Source Height: 1.0 m Peak Concentration Ratio: 9.94
 Time (UTC): 1032 to 1107 Obukhov Length (m): 12. Temperature (°C) 0-m: 16.4 0.5-m: 19.8 2.0-m: 20.5

Means					Variances				Skewness				
Height (m)	WS (m/s)	HD (Deg)	$\sigma\theta$ (Deg)	w (m/s)	$u'u'$ (m ² /s ²)	$v'v'$ (m ² /s ²)	$w'w'$ (m ² /s ²)	$T'T'$ (Deg K) ²	S_u	S_v	S_w	S_ϵ	
1.5	1.8	207	21.0	---	0.349	0.404	---	0.331	0.53	0.43	---	-0.68	
3.0	ND	ND	ND	-0.04	ND	ND	0.039	0.244	ND	ND	-0.31	-0.60	
6.0	2.6	223	18.0	---	0.496	0.354	---	0.166	0.40	0.48	---	-0.39	
9.0	ND	ND	ND	0.05	ND	ND	0.061	0.134	ND	ND	-0.12	-0.11	
Covariance Quadrants													
Height (m)	K_u	K_v	K_w	K_ϵ	$w'T'$	$u'T'$	$w'w'$ ($\sigma_w \sigma_T$)	$u'T'$ ($\sigma_u \sigma_T$)	$w'u' > 0$ $T' > 0$	$w'u' > 0$ $T' < 0$	$w'u' < 0$ $T' > 0$	$w'u' < 0$ $T' < 0$	
1.5	3.15	3.59	---	3.98	---	.1522	---	0.45	.1136	-0.145	-0.175	.0706	
3.0	ND	ND	5.92	4.07	-.0225	ND	-0.22	ND	.0110	-0.170	-.0248	.0083	
6.0	2.57	4.60	---	3.85	---	.1425	---	0.50	.0946	-0.122	-0.137	.0737	
9.0	ND	ND	3.76	3.47	-.0226	ND	-0.26	ND	.0078	-0.171	-.0212	.0079	

ND = No Data



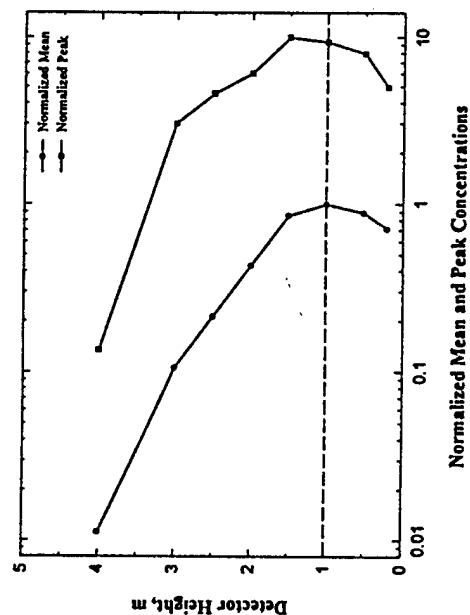
z	C	i	C_{pk}
4.0	1.09	5.86	27.09
3.0	4.21	3.67	78.35
2.5	6.37	3.03	96.98
2.0	9.62	2.43	103.89
1.5	16.24	2.18	163.08
1.0	18.78	2.08	186.61
0.5	17.94	2.01	169.51
0.25	16.81	1.78	145.51

Trial: P070515 Micrometeorological and Concentration Data Summary Date: 26 July 1995
 Source Distance: 12.5 m Source Height: 1.0 m Peak Concentration Ratio: 10.00
 Time (UTC): 1123 to 1158 Obukhov Length (m): 16. Temperature (°C) 0-m: 15.7 0.5-m: 20.0 2.0-m: 20.6

Height (m)	Means				Variances				Skewness			
	WS (m/s)	HD (Deg)	$\sigma\theta$ (Deg)	w (m/s)	u'u' (m ² /s ²)	v'v' (m ² /s ²)	w'w' (m ² /s ²)	T'T' (Deg K) ²	S _u	S _v	S _w	S _t
1.5	2.7	239	9.6	---	0.500	0.169	---	0.253	0.07	-0.04	---	-0.08
3.0	ND	ND	ND	-0.05	ND	ND	0.076	0.268	ND	ND	-0.14	-0.14
6.0	3.7	242	8.3	---	0.688	0.233	---	0.176	-0.08	0.01	---	-0.24
9.0	ND	ND	ND	0.09	ND	ND	0.116	0.180	ND	ND	0.02	-0.13

Height (m)	Kurtosis				Covariances Correlations				Covariance Quadrants			
	K _u	K _v	K _w	K _c	w'T'	u'T'	w'T' $\sigma_w\sigma_T$	u'T' $\sigma_u\sigma_T$	w'u'>0 T'>0	w'u'>0 T'<0	w'u'<0 T'>0	w'u'<0 T'<0
1.5	2.77	3.47	---	2.91	---	.2235	---	0.63	.1272	-0.114	-0.112	.1189
3.0	ND	ND	3.91	3.03	-.0427	ND	-0.30	ND	.0148	-0.023	-0.0361	.0110
6.0	2.69	3.20	---	3.10	---	.1898	---	0.55	.1070	-0.148	-0.142	.1117
9.0	ND	ND	3.63	3.23	-.0427	ND	-0.30	ND	.0123	-0.0318	-0.0354	.0122

ND = No Data



z	C	i	C _{pk}
4.0	0.20	13.73	2.41
3.0	1.90	5.81	53.67
2.5	3.80	4.11	81.16
2.0	7.74	2.93	107.53
1.5	15.29	2.38	178.64
1.0	17.86	1.96	167.52
0.5	15.86	1.89	142.11
0.25	12.77	1.56	88.86

Trial: P070605 Micrometeorological and Concentration Data Summary Date: 26 July 1995
 Source Distance: 20 m Source Height: 0.05 m Peak Concentration Ratio: ND*
 Time (UTC): 1200 to 1235 Obukhov Length (m): +10. Temperature (°C) 0-m: 13.9 0.5-m: 15.7 2.0-m: 17.6

Height (m)	Means				Variances				Skewness			
	WS (m/s)	HD (Deg)	$\sigma\theta$ (Deg)	w (m/s)	u'u' (m ² /s ²)	v'v' (m ² /s ²)	w'w' (m ² /s ²)	T'T' (Deg K) ²	S _u	S _v	S _w	S _e
1.5	1.3	190	34.5	---	0.15	0.65	---	0.460	1.01	-0.42	---	0.14
3.0	ND	ND	ND	-0.04	ND	ND	0.012	0.379	ND	ND	-0.15	0.52
6.0	1.7	226	31.4	---	0.77	0.68	---	0.427	0.70	-0.13	---	0.46
9.0	ND	ND	ND	+0.04	ND	ND	0.025	0.688	ND	ND	-0.28	0.18

Height (m)	Kurtosis				Covariances Correlations				Covariance Quadrants			
	K _u	K _v	K _w	K _e	w'T'	u'T'	w'T' $\sigma_w\sigma_T$	u'T' $\sigma_u\sigma_T$	w'u'>0 T'>0	w'u'>0 T'<0	w'u'<0 T'>0	w'u'<0 T'<0
1.5	2.93	2.40	---	3.11	---	.1617	---	0.62	.1031	-.0046	-.0029	.0659
3.0	ND	ND	6.22	2.18	-.0049	ND	-.07	ND	.0131	-.0071	-.0169	.0061
6.0	2.44	2.30	---	2.28	---	.3573	---	0.62	.2564	-.0143	-.0525	.1676
9.0	ND	ND	4.91	2.42	-.0078	ND	-.06	ND	.0208	-.0152	-.0289	.0156

ND = No Data

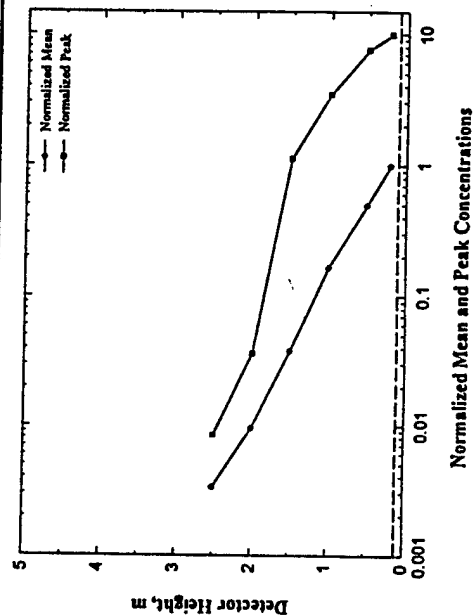
z	C	i	C _{pk}
4.0			
3.0			
2.5			
2.0			(Insufficient Data)
1.5			
1.0			
0.5			
0.25			

Trial: P070640 Micrometeorological and Concentration Data Summary Date: 26 July 1995
Source Distance: 12.5 m Source Height: 0.05 m Peak Concentration Ratio: 9.95
Time (UTC): 1254 to 1324 Obukhov Length (m): +3. Temperature (°C) 0-m: 13.7 0.5-m: 17.7 2.0-m: 18.9

Means				Variances				Skewness				
Height (m)	WS (m/s)	HD (Deg)	$\sigma\theta$ (Deg)	w (m/s)	$u'u'$ (m ² /s ²)	$v'v'$ (m ² /s ²)	$w'w'$ (m ² /s ²)	$T'T'$ (Deg K) ²	S_u	S_v	S_w	S_ϵ
1.5	1.8	151	6.5	---	0.119	0.038	---	0.442	-0.06	-0.24	---	-0.10
3.0	ND	ND	ND	-0.01	ND	ND	0.008	0.330	ND	ND	-0.08	-0.32
6.0	2.1	166	9.9	---	0.142	0.118	---	0.164	0.40	-0.42	---	-0.07
9.0	ND	ND	ND	-0.01	ND	ND	0.028	0.177	ND	ND	-0.45	0.12

Kurtosis				Covariances Correlations				Covariance Quadrants			
Height (m)	K_u	K_v	K_w	K_ϵ	$w'T'$	$u'T'$	$w'v'$ $\sigma_u\sigma_v$	$w'u'>0$ $T'>0$	$w'u'>0$ $T'<0$	$w'u'<0$ $T'>0$	$w'u'<0$ $T'<0$
1.5	2.77	2.45	---	3.16	---	.0137	---	.0533	-0.333	-0.337	.0274
3.0	ND	ND	6.41	3.03	-0.068	ND	-0.13	.0061	-0.091	-0.091	.0054
6.0	3.23	2.52	---	2.93	---	.0733	---	.0303	-0.074	-0.079	.0583
9.0	ND	ND	5.46	2.15	-0.056	ND	-0.08	.0087	-0.127	-0.118	.0102

ND = No Data



z	C	i	C_{pk}
4.0	---	---	---
3.0	---	---	---
2.5	0.09	12.13	0.23
2.0	0.26	8.54	0.99
1.5	1.04	8.16	30.79
1.0	4.56	4.02	94.51
0.5	13.59	2.95	208.17
0.25	27.32	2.09	271.81

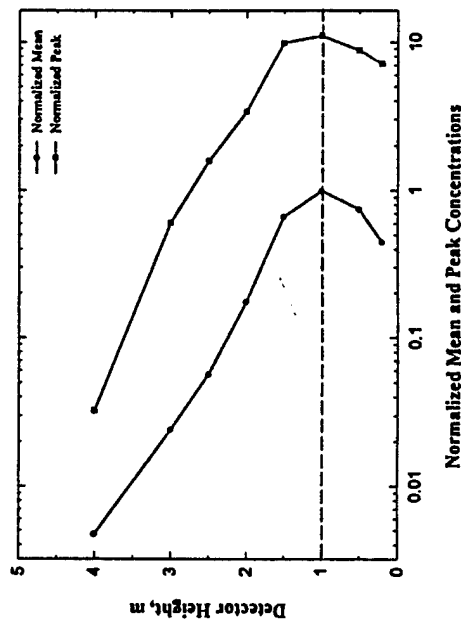
Trial: P100405 Micrometeorological and Concentration Data Summary Date: 29 July 1995

Source Distance: 25 m Source Height: 1.0 m Peak Concentration Ratio: 11.12

Time (UTC): 1027 to 1041 Obukhov Length (m): +3. Temperature (°C) 0-m: 16.4 0.5-m: 18.5 2.0-m: 19.8

Means					Variances				Skewness			
Height (m)	WS (m/s)	HD (Deg)	$\sigma\theta$ (Deg)	w (m/s)	$u'u'$ (m ² /s ²)	$v'v'$ (m ² /s ²)	$w'w'$ (m ² /s ²)	$T'T'$ (Deg K) ²	S_u	S_v	S_w	S_e
1.5	1.2	206	15.7	---	0.154	0.105	---	0.609	1.02	0.57	---	-0.19
3.0	ND	ND	ND	-0.03	ND	ND	0.008	0.466	ND	ND	1.11	-0.46
6.0	1.8	207	10.5	---	0.180	0.115	---	0.323	0.92	0.32	---	-0.05
9.0	ND	ND	ND	0.00	ND	ND	0.016	0.237	ND	ND	0.07	0.24

Kurtosis					Covariances Correlations				Covariance Quadrants			
Height (m)	K_u	K_v	K_w	K_e	$w'T'$	$u'T'$	$w'T'$ $\sigma_u\sigma_T$	$u'T'$ $\sigma_u\sigma_T$	$w'u'>0$ $T'>0$	$w'u'>0$ $T'<0$	$w'u'<0$ $T'>0$	$w'u'<0$ $T'<0$
1.5	3.55	2.66	---	2.87	---	0.2075	---	0.68	.1285	-.0050	-.0105	.0946
3.0	ND	ND	12.71	3.84	-0.0078	ND	-0.13	ND	.0064	-.0121	-.0083	.0064
6.0	3.58	2.32	---	3.48	---	0.1745	---	0.72	.1178	-.0069	-.0039	.0674
9.0	ND	ND	5.12	1.80	-0.0051	ND	-0.08	ND	.0102	-.0086	-.0136	.0071



ND = No Data

z	C	i	C_{pk}
4.0	0.13	14.92	0.87
3.0	0.65	8.87	16.30
2.5	1.52	6.75	42.25
2.0	4.68	4.35	90.82
1.5	17.87	2.86	263.94
1.0	26.69	2.39	296.70
0.5	20.08	2.49	236.43
0.25	12.00	2.70	191.43

Trial: P100550

Micrometeorological and Concentration Data Summary

Date: 29 July 1995

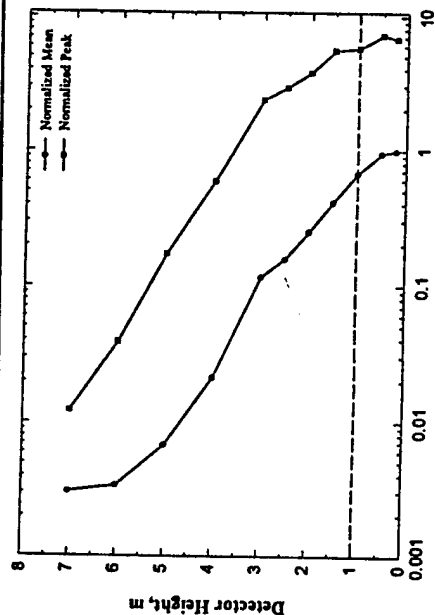
Source Distance: 75 m Source Height: 1.0 m Peak Concentration Ratio: 7.29

Time (UTC): 1149 to 1224 Obukhov Length (m): 1.0 Temperature (°C) 0-m: 14.1 0.5-m: 14.2 2.0-m: 15.0

Height (m)	Means				Variances				Skewness			
	WS (m/s)	HD (Deg)	$\sigma\theta$ (Deg)	w (m/s)	u'u' (m ² /s ²)	v'v' (m ² /s ²)	w'w' (m ² /s ²)	T'T' (Deg K) ²	S _u	S _v	S _w	S _{θ}
1.5	1.4	169	17.3	---	0.257	0.149	---	0.661	-0.11	+0.33	---	-0.59
3.0	ND	ND	ND	-0.03	ND	ND	0.005	0.557	ND	ND	+0.03	-0.62
6.0	2.0	195	18.7	---	0.585	0.466	---	0.781	-0.35	+0.44	---	-0.43
9.0	ND	ND	ND	0.04	ND	ND	0.012	---	ND	ND	+0.15	+0.12

Height (m)	Kurtosis				Covariances Correlations				Covariance Quadrants			
	K _u	K _v	K _w	K _{θ}	w'T'	u'T'	w'w' $\sigma_w\sigma_T$	u'T' $\sigma_u\sigma_T$	w'u'>0 T'>0	w'u'>0 T'<0	w'u'<0 T'>0	w'u'<0 T'<0
1.5	2.13	3.34	---	3.35	---	.0187	---	0.05	.0989	-.0724	-.0564	.0486
3.0	ND	ND	4.85	4.68	-.0109	ND	-.022	ND	.0051	-.01	-.01	.00
6.0	1.75	2.92	---	3.88	---	.4762	---	0.71	.2479	-.0205	-.0096	.2584
9.0	ND	ND	4.56	2.29	-.0181	ND	-.011	ND	.0175	-.03	-.02	.02

ND = No Data



z	C	i	C _{pk}
4.0	0.67	5.60	18.46
3.0	3.67	4.14	73.96
2.5	4.95	3.70	91.59
2.0	7.90	3.21	118.72
1.5	13.00	2.76	174.66
1.0	21.18	1.86	181.44
0.5	29.92	1.62	227.72
0.25	31.25	1.36	213.56

Trial: P100630 Micrometeorological and Concentration Data Summary Date: 29 July 1995

Source Distance: 75 m Source Height: 0.05 m Peak Concentration Ratio: ND*

Time (UTC): 1226 to 1302 Obukhov Length (m): Temperature (°C) 0-m: 14.5 0.5-m: 15.6 2.0-m: 16.5

Height (m)	Means				Variances				Skewness			
	WS (m/s)	HD (Deg)	$\sigma\theta$ (Deg)	w (m/s)	u'u' (m ² /s ²)	v'v' (m ² /s ²)	w'w' (m ² /s ²)	T'T' (Deg K) ²	S _u	S _v	S _w	S _e
1.5	1.8	179	11.9	---	0.233	0.137	---	0.357	+0.23	+0.08	---	-0.51
3.0	ND	ND	ND	-0.05	ND	ND	0.003	0.400	ND	ND	-0.27	-0.36
6.0	2.9	189	14.5	---	0.397	0.444	---	0.722	-0.23	-0.34	---	-0.69
9.0	ND	ND	ND	-0.01	ND	ND	0.005	0.548	ND	ND	-0.60	-0.74
Kurtosis												
Covariances Correlations					Covariance Quadrants							
Height (m)	K _u	K _v	K _w	K _e	w'T'	u'T'	w'T' $\sigma_w\sigma_T$	u'T' $\sigma_u\sigma_T$	w',u'>0 T'>0	w',u'>0 T'<0	w',u'<0 T'>0	w',u'<0 T'<0
1.5	2.30	2.47	---	2.68	---	-.1427	---	-0.50	.0258	-.0852	-.0908	.0075
3.0	ND	ND	6.59	3.15	-.0046	ND	-.13	ND	.0020	-.0073	-.0043	.0054
6.0	1.88	2.46	---	2.65	---	-.0284	---	-0.05	.1024	-.1008	-.0970	.0670
9.0	ND	ND	7.21	2.97	-.0019	ND	-.04	ND	.0058	-.0086	-.0066	.0073

*ND = No Data

z	C	i	C _{pk}
4.0			
3.0			
2.5			
2.0			
1.5			
1.0			
0.5			
0.25			

(insufficient data)

Trial: P100705

Micrometeorological and Concentration Data Summary

Date: 29 July 1995

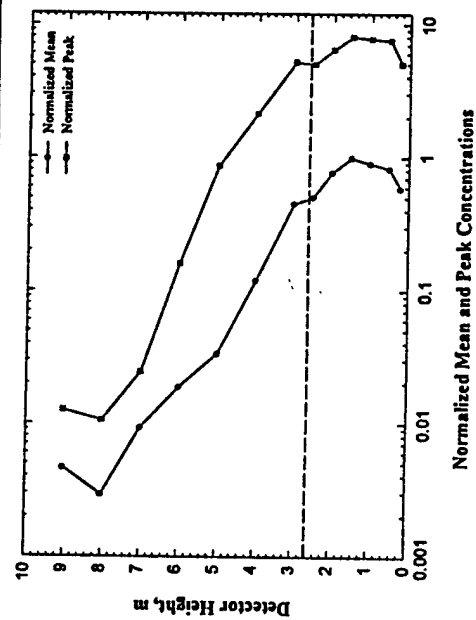
Source Distance: 75 m Source Height: 2.5 m Peak Concentration Ratio: 8.05

Time (UTC): 1308 to 1343 Obukhov Length (m): -1. Temperature (°C) 0-m: 16.8 0.5-m: 19.5 2.0-m: 19.3

Height (m)	Means				Variances				Skewness			
	WS (m/s)	HD (Deg)	$\sigma\theta$ (Deg)	w (m/s)	u'u' (m ² /s ²)	v'v' (m ² /s ²)	w'w' (m ² /s ²)	T'T' (Deg K) ²	S _u	S _v	S _w	S _{ϵ}
1.5	1.7	169	11.5	---	0.120	0.100	---	2.888	0.05	-0.01	---	0.00
3.0	ND	ND	ND	-0.03	ND	ND	0.005	1.871	ND	ND	0.09	-0.35
6.0	2.4	179	8.4	---	0.287	0.107	---	0.608	-1.10	0.22	---	-1.18
9.0	ND	ND	ND	-0.02	ND	ND	0.006	0.114	ND	ND	-0.09	-0.86

Height (m)	Kurtosis				Covariances Correlations				Covariance Quadrants			
	K _u	K _v	K _w	K _{ϵ}	w'T' $\sigma_w\sigma_T$	u'T' $\sigma_u\sigma_T$	w'v' $\sigma_w\sigma_v$	T'T' $\sigma_T\sigma_T$	w'u'>0 T'>0	w'u'>0 T'<0	w'u'<0 T'>0	w'u'<0 T'<0
1.5	2.55	2.57	---	1.50	---	-0.0884	---	-0.15	.0903	-.1307	-.1392	.0912
3.0	ND	ND	5.18	1.77	.0049	ND	0.05	ND	.0154	-.0100	-.0148	.0141
6.0	19.69	2.43	---	7.05	---	-.2365	---	-0.56	.0308	-.1699	-.1075	.0102
9.0	ND	ND	4.81	4.80	-.0018	ND	-0.07	ND	.0020	-.0038	-.0030	.0032

ND = No Data



z	C	i	C _{pk}
4.0	3.19	3.48	57.05
3.0	12.11	2.45	138.78
2.5	13.54	2.15	133.52
2.0	20.83	1.93	172.05
1.5	26.78	1.87	215.64
1.0	24.33	1.92	208.41
0.5	22.23	1.95	202.66
0.25	15.79	1.85	134.31

Trial: P122325 Micrometeorological and Concentration Data Summary Date: 31 Jul/01 Aug 1995

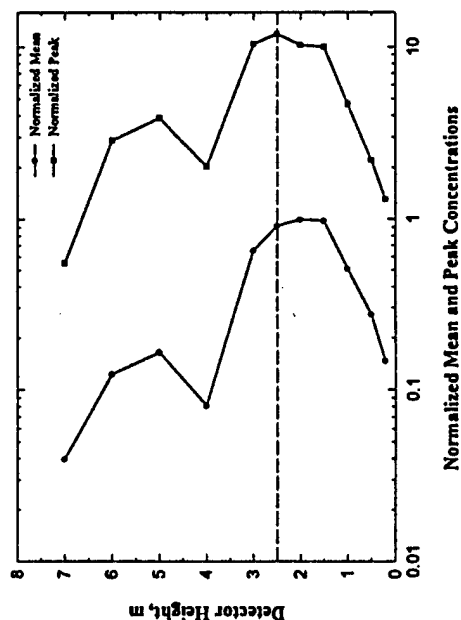
Source Distance: 75 m Source Height: 2.5 m Peak Concentration Ratio: 12.01

Time (UTC): 0521 to 0538 Obukhov Length (m): -1. Temperature (°C) 0-m: 14.2* 0.5-m: 15.4* 2.0-m: 16.4*

Height (m)	Means				Variances				Skewness			
	WS (m/s)	HD (Deg)	$\sigma\theta$ (Deg)	w (m/s)	u'u' (m ² /s ²)	v'v' (m ² /s ²)	w'w' (m ² /s ²)	T'T' (Deg K) ²	S _u	S _v	S _w	S _{θ}
1.5	1.3	193	6.5	---	0.048	0.018	---	0.957	-0.58	0.64	---	-0.63
3.0	ND	ND	ND	-0.03	ND	ND	0.003	0.442	ND	ND	0.13	-0.01
6.0	1.9	197	5.5	---	0.084	0.029	---	0.485	-0.53	-0.22	---	0.11
9.0	ND	ND	ND	+0.02	ND	ND	0.009	0.157	ND	ND	0.05	-1.64

Height (m)	Kurtosis				Covariances Correlations				Covariance Quadrants			
	K _u	K _v	K _w	K _{θ}	w'T'	u'T'	w'w' $\sigma_w\sigma_T$	u'T' $\sigma_u\sigma_T$	w'u'>0 T'>0	w'u'>0 T'<0	w'u'<0 T'>0	w'u'<0 T'<0
1.5	2.96	3.57	---	3.22	---	0.1749	---	+0.81	.0709	-.0027	-.0021	.1088
3.0	ND	ND	6.50	2.62	.0043	ND	+0.12	ND	.0045	-.0035	-.0030	.0058
6.0	2.38	2.42	---	1.83	---	-0.1197	---	-0.59	.0102	-.0425	-.0936	.0062
9.0	ND	ND	4.93	6.87	-.0021	ND	-0.06	ND	.0041	-.0063	-.0057	.0059

*Single point estimate
ND = No Data



z	C	i	C _{pk}
4.0	0.19	7.09	4.83
3.0	0.68	5.68	15.62
2.5	1.40	4.31	25.85
2.0	3.31	3.51	60.87
1.5	7.78	2.93	116.14
1.0	13.41	2.72	171.62
0.5	13.94	2.57	163.58
0.25	10.96	2.27	109.30

Trial: P132250 Micrometeorological and Concentration Data Summary Date: 02 Aug 1995
Source Distance: 100 m Source Height: 2.5 m Peak Concentration Ratio: ND*
Time (UTC): 0446 to 0521 Obukhov Length (m): Temperature (°C) 0-m: 21.5 0.5-m: 22.6 2.0-m: 23.6

Height (m)	Means				Variances				Skewness			
	WS (m/s)	HD (Deg)	$\sigma\theta$ (Deg)	w (m/s)	u'u' (m ² /s ²)	v'v' (m ² /s ²)	w'w' (m ² /s ²)	T'T' (Deg K) ²	S _u	S _v	S _w	S _c
1.5	2.0	217	22.2	---	0.140	0.537	---	1.617	0.00	-0.23	---	1.29
3.0	ND	ND	ND	-0.07	ND	ND	0.005	2.199	ND	ND	1.41	0.27
6.0	2.9	219	18.8	---	0.158	0.847	---	1.200	0.54	-0.24	---	-1.15
9.0	ND	ND	ND	ND	ND	ND	ND	0.837	ND	ND	ND	-1.71
Height (m)	Kurtosis				Covariances Correlations				Covariance Quadrants			
	K _u	K _v	K _w	K _c	w'T'	u'T'	w'T' $\sigma_w\sigma_T$	u'T' $\sigma_u\sigma_T$	w',u'>0 T'>0	w',u'>0 T'<0	w',u'<0 T'>0	w',u'<0 T'<0
1.5	2.43	1.91	---	4.50	---	.1886	---	0.40	.1944	-.0826	-.0092	.0859
3.0	ND	ND	18.98	2.65	-.0220	ND	-0.20	ND	.0080	-.0266	-.0125	.0100
6.0	2.26	2.11	---	5.08	---	.1394	---	0.32	.0420	-.0165	-.0311	.1451
9.0	ND	ND	30.32	9.25	-.0363	ND	-0.14	ND	.0238	-.0475	-.0276	.0149

*ND = No Data

z	C	i	C _{pk}
4.0			
3.0			
2.5			
2.0			
1.5			
1.0			
0.5			
0.25			

(Insufficient Data)

Trial: P132340 Micrometeorological and Concentration Data Summary Date: 02 Aug 1995
 Source Distance: 100 m Source Height: 2.5 m Peak Concentration Ratio: ND*
 Time (UTC): 0534 to 0609 Obukhov Length (m): +1. Temperature (°C) 0-m: 21.3 0.5-m: 22.0 2.0-m: 22.6

Height (m)	Means				Variances				Skewness			
	WS (m/s)	HD (Deg)	$\sigma\theta$ (Deg)	w (m/s)	u'u' (m ² /s ²)	v'v' (m ² /s ²)	w'w' (m ² /s ²)	T'T' (Deg K) ²	S _u	S _v	S _w	S _e
1.5	1.6	188	24.1	---	0.315	0.326	---	0.562	-0.00	-0.17	---	-0.37
3.0	ND	ND	ND	-0.04	ND	ND	0.005	0.841	ND	ND	-0.03	-0.23
6.0	2.8	193	13.8	---	0.278	0.457	---	1.754	0.15	0.50	---	-1.63
9.0	ND	ND	ND	-0.01	ND	ND	0.006	0.343	ND	ND	0.54	-4.75

Height (m)	Kurtosis				Covariances Correlations				Covariance Quadrants			
	K _u	K _v	K _w	K _e	w'T'	u'T'	w'w' $\sigma_w\sigma_T$	u'T' $\sigma_u\sigma_T$	w'u'>0 T'>0	w'u'>0 T'<0	w'u'<0 T'>0	w'u'<0 T'<0
1.5	2.70	2.93	---	2.79	---	.2862	---	0.68	.1169	-.0043	-.0034	.1769
3.0	ND	ND	5.01	2.51	-.0205	ND	-0.31	ND	.0039	-.0153	-.0129	.046
6.0	2.42	4.56	---	4.84	---	.3682	---	0.52	.0705	-.0595	-.0268	.3839
9.0	ND	ND	14.86	33.10	-.0015	ND	-0.03	ND	.0026	-.0084	-.0020	.0064

*ND = No Data

z	C	i	C _{pk}
4.0			
3.0			
2.5			
2.0			
1.5			
1.0			
0.5			
0.25			

(Insufficient Data)

Trial: P140030

Micrometeorological and Concentration Data Summary

Date: 02 Aug 1995

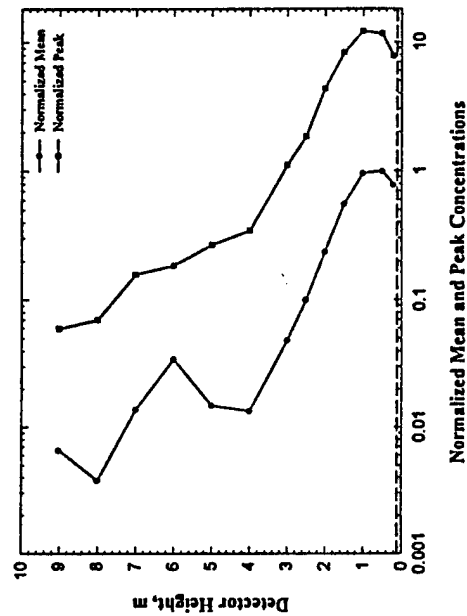
Source Distance: 100 m Source Height: 0.05 m Peak Concentration Ratio: 12.31

Time (UTC): 0625 to 0700 Obukhov Length (m): +3. Temperature (°C) 0-m: 19.5 0.5-m: 20.0 2.0-m: 20.5

Height (m)	Means				Variances				Skewness			
	WS (m/s)	HD (Deg)	$\sigma\theta$ (Deg)	w (m/s)	u'u' (m ² /s ²)	v'v' (m ² /s ²)	w'w' (m ² /s ²)	T'T' (Deg K) ²	S _u	S _v	S _w	S _e
1.5	1.7	212	21.7	---	0.145	0.511	---	0.172	-0.12	1.03	---	0.21
3.0	ND	ND	ND	-0.04	ND	ND	0.010	0.302	ND	ND	0.28	0.37
6.0	2.6	210	17.3	---	0.271	0.677	---	0.560	0.15	0.61	---	0.30
9.0	ND	ND	ND	0.00	ND	ND	0.013	0.552	ND	ND	0.07	0.07

Height (m)	Kurtosis				Covariances Correlations				Covariance Quadrants			
	K _u	K _v	K _w	K _e	w'T'	u'T'	w'w' $\sigma_u\sigma_T$	u'T' $\sigma_u\sigma_T$	w'u'>0 T'>0	w'u'>0 T'<0	w'u'<0 T'>0	w'u'<0 T'<0
1.5	3.29	3.53	---	2.72	---	0.0197	---	0.12	.0329	-.0090	-.0340	.0298
3.0	ND	ND	5.64	3.32	-.0127	ND	-.23	ND	.0026	-.0109	-.0091	.0052
6.0	2.44	2.73	---	2.44	---	0.0512	---	0.13	.0545	-.0460	-.0603	.1029
9.0	ND	ND	4.94	2.16	-.0112	ND	-.13	ND	.0094	-.0173	-.0138	.0107

ND - No Data



z	C	i	C _{pk}
4.0	0.19	7.09	4.83
3.0	0.68	5.68	15.62
2.5	1.40	4.31	25.85
2.0	3.31	3.51	60.87
1.5	7.78	2.93	116.14
1.0	13.41	2.72	171.62
0.5	13.94	2.57	163.58
0.25	10.96	2.27	109.30

Trial: P142154 Micrometeorological and Concentration Data Summary Date: 03 Aug 1995

Source Distance: 100 m Source Height: 2.5 m Peak Concentration Ratio:

Time (UTC): 03:55 to 04:30 Obukhov Length (m): +5. Temperature (°C) 0-m: 23.5 0.5-m: 24.5 2.0-m: 25.2

Height (m)	Means				Variances				Skewness			
	WS (m/s)	HD (Deg)	$\sigma\theta$ (Deg)	w (m/s)	u'u' (m ² /s ²)	v'v' (m ² /s ²)	w'w' (m ² /s ²)	T'T' (Deg K) ²	S _u	S _v	S _w	S _e
1.5	1.7	171	24.7	---	0.590	0.185	---	0.956	-0.75	0.04	---	0.88
3.0	ND	ND	ND	-0.02	ND	ND	0.011	1.128	ND	ND	1.20	0.51
6.0	2.0	175	25.3	---	0.657	0.290	---	0.481	-0.88	0.63	---	-0.65
9.0	ND	ND	ND	-0.01	ND	ND	0.026	0.327	ND	ND	0.31	-0.48

Height (m)	Kurtosis				Covariances Correlations				Covariance Quadrants			
	K _u	K _v	K _w	K _c	w'T'	u'T'	w'T' $\sigma_w\sigma_T$	u'T' $\sigma_u\sigma_T$	w'u'>0 T'>0	w'u'>0 T'<0	w'u'<0 T'>0	w'u'<0 T'<0
1.5	3.69	2.62	---	3.95	---	-0.0163	---	-0.02	.1213	-0.785	-0.1597	.1006
3.0	ND	ND	8.47	3.24	-0.044	ND	-0.04	ND	.0171	-0.0200	-0.0144	.0121
6.0	2.99	2.24	---	4.79	---	0.0446	---	0.08	.0605	-0.0809	-0.0753	.1403
9.0	ND	ND	9.02	4.32	-0.160	ND	-0.18	ND	.0130	-0.0217	-0.0151	.0079

ND = No Data

z	C	i	C _{pk}
4.0			
3.0			
2.5			
2.0			
1.5			
1.0			
0.5			
0.25			

(Insufficient Data)

Trial: PL42245 Micrometeorological and Concentration Data Summary Date: 2/3 August 1995

Source Distance: 100 m Source Heights: 0.05 m Peak Concentration Ratio: ND*

Time (UTC): 0458 to 0533 Obukhov Length (m): 8. Temperature (°C) 0-m: 22.2 0.5-m: 22.0 2.0-m: 22.4

Height (m)	Means				Variances				Skewness			
	WS (m/s)	HD (Deg)	$\sigma\theta$ (Deg)	w (m/s)	u'u' (m ² /s ²)	v'v' (m ² /s ²)	w'w' (m ² /s ²)	T'T' (Deg K) ²	S _u	S _v	S _w	S _t
1.5	1.6	115	20.2	---	0.145	0.324	---	2.245	0.68	0.82	---	1.70
3.0	ND	ND	ND	-0.01	ND	ND	0.006	4.907	ND	ND	0.33	1.05
6.0	2.1	100	15.7	---	0.203	0.311	---	2.095	0.18	0.11	---	-1.35
9.0	ND	ND	ND	-0.04	ND	ND	0.009	0.349	ND	ND	-0.12	-1.02

Height (m)	Kurtosis				Covariances Correlations				Covariance Quadrants			
	K _u	K _v	K _w	K _c	w'T'	u'T'	w'v'	u'T'	w'u'>0 T'>0	w'u'>0 T'<0	w'u'<0 T'>0	w'u'<0 T'<0
1.5	3.27	2.75	---	5.88	---	.2899	---	0.51	.2594	-.0523	-.0194	.1023
3.0	ND	ND	14.32	2.91	.0111	ND	---	ND	.0326	-.0138	-.0276	.0215
6.0	3.37	2.56	---	4.03	---	-.0682	---	-0.16	.1114	-.1017	-.1263	.0483
9.0	ND	ND	4.26	3.67	.0079	ND	-.174	ND	.0099	-.0049	-.0068	.0094

*ND = No Data

z	C	i	C _{pk}
4.0			
3.0			
2.5			
2.0			
1.5			
1.0			
0.5			
0.25			

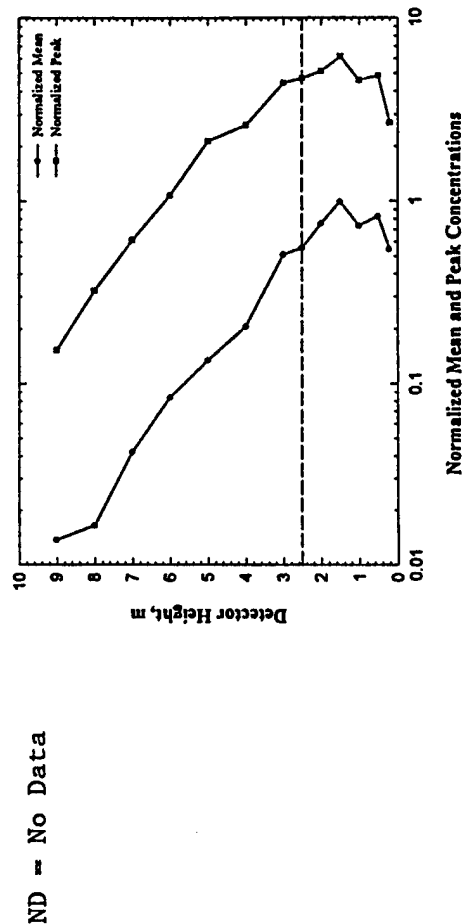
(Insufficient Data)

Trial: P150010 Micrometeorological and Concentration Data Summary Date: 03 August 1995

Source Distance: 100 m Source Height: 2.5 m Peak Concentration Ratio: 6.18

Time (UTC): 1208 to 1233 Obukhov Length (m): +6. Temperature (°C) 0-m: 21.5 0.5-m: 22.3 2.0-m: 22.5

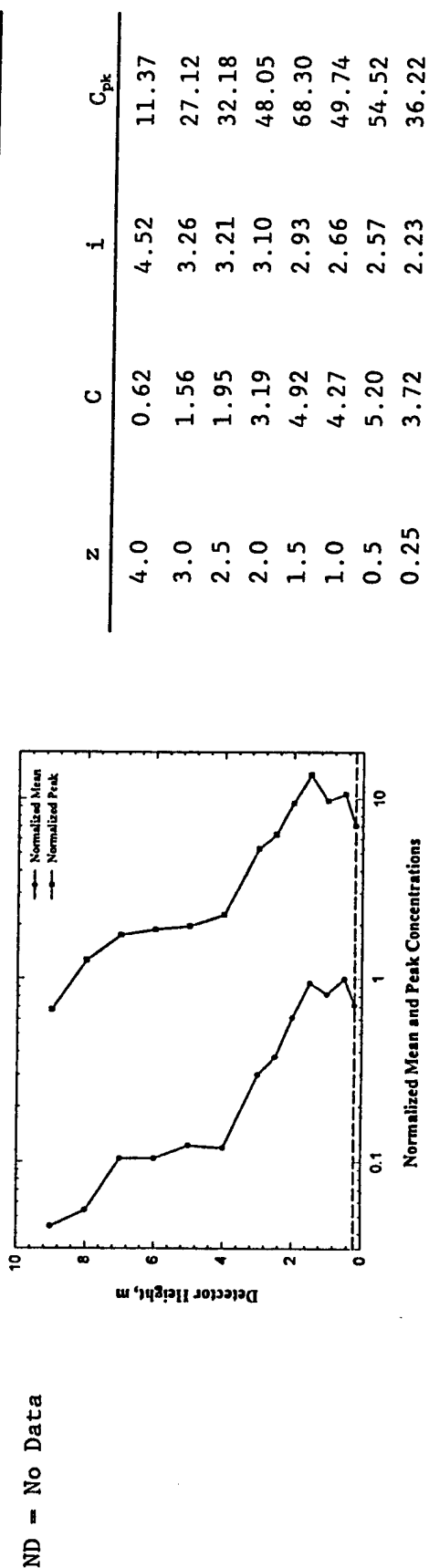
Height (m)	Means				Variances				Skewness			
	WS (m/s)	HD (Deg)	$\sigma\theta$ (Deg)	w (m/s)	u'u' (m ² /s ²)	v'v' (m ² /s ²)	w'w' (m ² /s ²)	T'T' (Deg K) ²	S _u	S _v	S _w	S _c
1.5	2.3	212	15.8	---	0.302	0.544	---	1.985	0.61	-1.32	---	0.85
3.0	ND	ND	ND	-0.05	ND	ND	0.039	1.662	ND	ND	-0.16	0.81
6.0	3.2	213	1.61	---	0.269	0.977	---	2.188	0.41	-1.07	---	0.56
9.0	ND	ND	ND	+0.01	ND	ND	0.076	3.081	ND	ND	-0.40	0.19
Kurtosis												
Covariances Correlations												
Height (m)	K _u	K _v	K _w	K _c	w'T'	u'T'	w'T' $\sigma_w\sigma_t$	u'T' $\sigma_u\sigma_t$	w'u'>0 T'>0	w'u'>0 T'<0	w'u'<0 T'>0	w'u'<0 T'<0
1.5	3.42	5.35	---	2.34	---	0.4336	---	0.56	.3091	-.0403	-.0369	.2016
3.0	ND	ND	4.57	2.31	-0.0287	ND	-.13	ND	.0312	-.0478	-.0445	.0324
6.0	3.66	4.56	---	2.03	---	0.3325	---	0.43	.2566	-.0518	-.0610	.1888
9.0	ND	ND	8.52	1.96	-0.0410	ND	-.10	ND	.0427	-.0763	-.0586	.0513
Covariance Quadrants												



Trial: P150050 Micrometeorological and Concentration Data Summary Date: 03 Aug 1995
Source Distance: 100 m Source Height: 0.05 m Peak Concentration Ratio: 13.14
Time (UTC): 0649 to 0704 Obukhov Length (m): +6. Temperature (°C) 0-m: 21.5 0.5-m: 22.7 2.0-m: 23.0

Means				Variances				Skewness			
Height (m)	WS (m/s)	HD (Deg)	$\sigma\theta$ (Deg)	w (m/s)	$u'u'$ (m^2/s^2)	$v'v'$ (m^2/s^2)	$w'w'$ (m^2/s^2)	$T'T'$ (Deg K) ²	S_u	S_v	S_w
1.5	2.4	174	11.4	---	0.123	0.217	---	0.222	0.31	-1.13	---
3.0	ND	ND	ND	-0.05	ND	ND	0.020	0.243	ND	ND	0.02
6.0	3.3	182	12.7	---	0.147	0.492	---	0.500	0.12	-1.24	---
9.0	ND	ND	ND	-0.03	ND	ND	0.026	0.680	ND	ND	-0.04

Kurtosis				Covariances Correlations				Covariance Quadrants			
Height (m)	K_u	K_v	K_w	K_c	$w'T'$	$u'T'$	$w'w'$ (m^2/s^2)	$u'u'$ (m^2/s^2)	$w'u' > 0$ $T' > 0$	$w'u' > 0$ $T' < 0$	$w'u' < 0$ $T' < 0$
1.5	3.06	4.38	---	2.86	---	0.0531	---	+0.32	.0387	-.0083	-.0174
3.0	ND	ND	3.41	3.39	-.0169	ND	-0.24	ND	.0050	-.0137	-.0146
6.0	2.56	4.18	---	3.45	---	0.0825	---	+0.30	.0516	-.0179	-.0176
9.0	ND	ND	5.05	3.41	-.0115	ND	-0.09	ND	.0310	-.0181	-.0335



APPENDIX B. REFERENCES

- Biltoft, C. A., 1993: Concentration fluctuation modeling of chemical hazards (assess vulnerability). Report No. DPG/JOD-93-001, U.S. Army Dugway Proving Ground, Dugway, UT.
- Biltoft, C. A., 1995: Surface effects on concentration fluctuation profiles. Report No. DPG/JCP-95/019, U.S. Army Dugway Proving Ground, Dugway, UT.
- Biltoft, C. A., 1997: Phase I of Defense Special Weapons Agency transport and dispersion model validation. Report No. DPG-FR-97-058, U.S. Army Dugway Proving Ground, Dugway, UT.
- Blackwelder, R. F. and J. H. Haritonidis, 1983: Scaling of the bursting frequency in turbulent boundary layers. J. Fluid Mech., 132, 87-103.
- Briggs, G. A., 1988: Analysis of diffusion field experiments. In Lectures on Air Pollution Modeling, A. Venkatram and J. C. Wyngaard (Eds.), Amer. Meteor. Soc., Boston, 63-117.
- Busch, N. E. and H. A. Panofsky, 1968: Recent spectra of atmospheric turbulence. Quart. J. Roy. Meteor. Soc., 94, 132-148.
- Businger, J. A., 1973: Turbulent transfer in the atmospheric surface layer. Workshop in Micrometeorology, D. A. Haugen (Ed.), Amer. Meteor. Soc., Boston, MA, 67-100.
- Chatwin, P. C. 1985: Towards a box model of all stages of heavy gas cloud dispersion. Turbulence and Diffusion In Stable Environments, J. C. R. Hunt (Ed.), Clarendon Press, Oxford, UK, 259-291.
- Deardorff, J. W., 1972: Numerical investigation of neutral and unstable planetary boundary layers. J. Atmos. Sci., 29, 91-115.
- Deardorff, J. W., 1985: Laboratory experiments in diffusion: The use of convective mixed-layer scaling. J. Clim. and Appl. Meteor., 24, 1143-1151.
- Fackrell, J.E., 1984: Parameters characterizing dispersion in the near wake of buildings. J. Wind Eng. Ind. Aero., 16, 97-118.
- Falco, R. E., 1991: A coherent structure model of the turbulent boundary layer and its ability to predict Reynolds number dependence. Phil. Trans. R2 Soc. Lond. A, 336, 103-129.
- Folz, A. B., 1997: An experimental study of the near-surface turbulence in the atmospheric surface layer. Ph.D. Thesis, University of Maryland, College Park, MD.
- Garratt, J.R., 1992: The Atmospheric Boundary Layer. Cambridge University Press, UK, 316 pp.

- Haugen, D.A. and J.C. Kaimal, 1969: Some errors in the measurement of Reynolds stress. J. Appl. Meteor., 8, 460-462.
- Holtstag, A.A.M. and F.T.M. Nieustadt, 1986: Scaling the atmospheric boundary layer. Boundary-Layer Meteor., 36, 201-209.
- Hunt, A. and J.P. Castro, 1984: Scalar dispersion in model building wakes. J. Wind Eng. Ind. Aero., 17, 89-115.
- Kaimal, J.C. and J.E. Gaynor, 1983: The Boulder Observatory. J. Climate & Appl. Meteor., 22, 863-880.
- Kaimal, J. C. and J. J. Finnigan, 1994: Atmospheric Boundary Layer Flows. Oxford University Press, NY, 304 pp.
- Kim, J., P. Moin, and R. Moses, 1987: Turbulence statistics in a fully developed channel flow at low Reynolds number. J. Fluid Mech., 177, 133-166.
- Klewicki, J. C., 1989: On the interactions between the inner and outer region motions in turbulent layers. Ph.D. dissertation, Michigan State University, East Lansing, MI.
- Klewicki, J. C. and R. E. Falco, 1990: On accurately measuring statistics associated with small scale structure in turbulent boundary layers using hot-wire probes. J. Fluid Mech., 219, 119-142.
- Klewicki, J. C., M. M. Metzger, E. Kelner, and E. M. Thurlow, 1995: Viscous sublayer flow visualizations at $Re \approx 1500000$. Phys. Fluids, 7, 857-863.
- Kline, S. J., W. C. Reynolds, F. A. Schraub, and P. W. Runstadler, 1967: The structure of turbulent boundary layers. J. Fluid Mech., 30, 741-773.
- Long, R. R. and T. C. Chen, 1981: Experimental evidence for the existence of the "mesoscale" in turbulent systems. J. Fluid Mech., 105, 19-59.
- Mavroidis, I., 1996: Field experiments on secondary source generation by obstacle wake entrainment. Report No. C2044/015/CBDE, University of Manchester Institute of Science and Technology, Environmental Technology Centre, Manchester, England.
- Mavroidis, I., 1997: Atmospheric dispersion around buildings. PhD thesis (draft), University of Manchester Institute of Science and Technology, Manchester, England.
- Metzger, M. and J.C. Klewicki, 1996: Statistics of velocity and pressure in the surface layer over the Salt Flats of Utah's West Desert. Report No. PFD 96-01, University of Utah Department of Mechanical Engineering, Physical Fluid Dynamics Laboratory, Salt Lake City, UT.
- Murlis, J., H. M. Tsai, and P. Bradshaw, 1982: The structure of turbulent boundary layers at low Reynolds numbers. J. Fluid Mech., 122, 13-56.

- Raupach, M.R., 1981: Conditional statistics of Reynolds stress in rough-wall and smooth-wall turbulent boundary layers. J. Fluid Mech., 108, 363-382.
- Raupach, M. R., 1983: Near-field dispersion from instantaneous sources in the surface layer. Boundary-Layer Meteor., 27, 105-113.
- Roberts, I., 1994: Droplet evaporation from porous surfaces. CBDE Report 2044-022-CBDE. Environmental Technology Centre, Department of Chemical Engineering, University of Manchester Institute of Science and Technology, Manchester, England.
- Roberts, I., 1996: The evaporation of neat/thickened agent simulants from porous surfaces. CBDE Report 2044-013-CBDE (in preparation).
- Robinson, S., 1991: Coherent motions in the turbulent boundary layer. Ann. Rev. Fluid Mech., 23, 601-639.
- Schlichting, H., 1979: Boundary Layer Theory, (trans. J. Kestin) 7th ed., McGraw-Hill, Hamburg, 817 pp.
- Smith, C.R. and S.P. Metzler, 1983: The characteristics of low-speed streaks in the near-wall region of a turbulent boundary layer. J. Fluid Mech., 129, 27-54.
- Stull, R. B., 1988: An Introduction to Boundary Layer Meteorology, Kluwer, Dordrecht NL, 666 pp.
- Tavoularis, S. and S. Corrsin, 1981: Experiments in nearly homogeneous turbulent shear flow with a uniform mean temperature gradient. Part 1. J. Fluid Mech., 104, 311-347.
- Venkatram, A., 1988: Dispersion in the stable boundary layer. In Lectures on Air Pollution Modeling, A. Venkatram and J. C. Wyngaard (Eds.), Amer. Meteor. Soc., Boston, MA, 267-324.
- Willmarth, W. W. and S. S. Lu, 1972: Structure of Reynolds stress near the wall. J. Fluid Mech., 55, 65-92.
- Wyngaard, J. C., O. R. Cote', and Y. Izumi, 1971: Local free convection, similarity, and the budgets of shear stress and heat flux. J. Atmos. Sci., 28, 1171-1182.
- Wyngaard, J. C., 1973: On surface-layer turbulence. In Workshop on Micro-meteorology, D. A. Haugen (Ed.), Amer. Meteor. Soc., Boston, MA, 100-149.
- Wyngaard, J.C. and J.C. Weil, 1991: Transport asymmetry in skewed turbulence. Phys. Fluids, 3, 155-162.
- Yee, E., P. R. Kosteniuk, G. M. Chandler, C. A. Biltoft, and J. F. Bowers, 1993: Statistical characteristics of concentration fluctuations in dispersing plumes in the atmospheric surface layer. Boundary-Layer Meteor., 65, 69-109.

Yee, E., R. Chan, P. R. Kosteniuk, G. M. Chandler, C. A. Biltoft, and J. F. Bowers, 1994: Incorporation of internal fluctuations in a meandering plume model of concentration fluctuations. Boundary-Layer Meteor., 67, 11-39.

APPENDIX C. LIST OF SYMBOLS

c	Speed of sound
C	Mean measured concentration
C_{uw}	Correlation between horizontal and vertical velocity fluctuations
C_{wT}	Correlation between temperature and vertical velocity fluctuations
C_{uT}	Correlation between temperature and horizontal velocity fluctuations
C_p	Specific heat at constant pressure
C_{pk}	Peak (99th percentile) measured concentration
d	Droplet diameter
D_{21}	Horizontal component of turbulent thermal diffusivity
D_{22}	Vertical component of turbulent thermal diffusivity
g	Gravitational acceleration
H	Heat Flux, $\rho C_p \overline{wT'}$
h	Cube face length
h'	Wake width
h_a	Momentum deficit thickness
h_r	Surface texture or grain size
i	Concentration fluctuation intensity (ratio of the concentration standard deviation to the mean concentration)
K	Kurtosis of the concentration field measured at a detector
k	von Karman constant (nondimensional parameter with a magnitude of 0.4)
L	Obukhov length ($L = \rho C_p u_*^3 / \rho g H$)
n	Sample size
P/M	Ratio of plume profile peak concentration to plume centroid mean concentration
q^2	Turbulent kinetic energy

LIST OF SYMBOLS
(CONTINUED)

R_f	Flux Richardson number
R_p	Plume Richardson Number
R_θ	Momentum deficit thickness Reynolds number
S	Skewness of the concentration distribution measured at a detector
T	Temperature, degrees Kelvin
T'^2	Temperature variance
t	Averaging time
t_d	Residence time
t_r	Nondimensional residence time
u	Wind speed
U	Mean wind speed at plume centroid
u_τ	Surface shear stress
u_*	Friction velocity, the square root of the vertical momentum flux $(-\overline{u'w'})^{1/2}$
u'	Axial velocity root-mean square (rms)
u'^2	Alongwind velocity variance
U_∞	Free stream velocity above the boundary layer
u^+	Inner-normalized mean axial velocity (u/u_τ)
u'^+	Inner-normalized axial velocity rms (u'/u_τ)
v'^2	Crosswind velocity variance
w	Vertical velocity
w'^2	Vertical velocity variance
w_F	Free convection scale
w_*	Convective velocity scale
x	Downwind distance from dissemination point to detector array

LIST OF SYMBOLS
(CONTINUED)

X	Dimensionless downwind distance in a convective boundary layer $\left(\frac{X w_*}{U z_i} \right)$
y*	Spanwise pocket scale (y_{u_r}/v)
z _c	Height of the plume centroid
z _i	Mixed Layer depth, height of the atmospheric boundary layer
z _o	Aerodynamic roughness parameter
z _p	Height of the plume peak concentration
z _r	Height of detector above ground
z _s	Height of source above ground
z*	Nondimensional height
ε	Turbulent kinetic energy dissipation rate
λ _i	Inertial scale
λ _T	Taylor microscale
θ	Potential temperature, degrees Kelvin
τ	Plume travel time normalized by the Lagrangian timescale
ρ	Density of air
v	Tracer particle vertical drift velocity
ν	Viscosity of air
ν _r	Eddy viscosity
χ	Instantaneous concentration
ϑ	Mean tracer particle drift velocity

Blank Page

APPENDIX D DO49 DISTRIBUTION LIST

STATE DEPARTMENT
ATTN: INR (MR. CROCKER)
WASHINGTON, DC 20520

OFFICE OF THE SECRETARY OF DEFENSE
ATTN: ATSD-AE-C/B M
ROOM 3C124
WASHINGTON, DC 20301-3050

WEAPONS TECHNOLOGY CONTROL DIVISION
DIRECTOR FOR STRATEGIC PLANS & POLICY
J 5, 5115 JOINT STAFF, THE PENTAGON
WASHINGTON, DC 20318-5116

DIRECTOR
DEFENSE NUCLEAR AGENCY
ATTN: OPAC J FOX.
6801 TELEGRAPH RD
ALEXANDRIA, VA 22310-3398

DIRECTOR
CENTRAL INTELLIGENCE AGENCY
ATTN: OWTP
WASHINGTON, DC 20506

DIN PAX-4
FORT DETRICK, FREDERICK, MD 21701-5004

HQ USEUCOM
UNIT 30400, BOX 1000
ATTN: ECJ5-P
APO AE 09128-4209

USCINCPAC
ATTN: J543
BOX 64015
CAMP H.M. SMITH, HI 96861-4015

COMMANDER IN CHIEF
U.S. ATLANTIC COMMAND
ATTN: J33CW
1562 MITSCHER AVE, STE 200
NORFOLK, VA 23551-2488

HEADQUARTERS
USSOUTHCOM
ATTN: SCSG
UNIT 1175
APO AA 34003-5000

COMMANDER IN CHIEF
U.S. SPACE COMMAND
ATTN: SPJ33Z (LTC SPOEHR)
PETERSON AFB, CO 80914-5000

COMMANDER
JSOC
P.O. BOX 70239
ATTN: J3-NBC
FORT BRAGG, NC 28307-5000

JOINT PROGRAM FOR BIOLOGICAL DEFENSE
ATTN: GEN DOESBURG
5201 LEESBURG PIKE, SUITE 1200, SKYLINE 3
FALLS CHURCH, VA 22041-3203

USTRANSCOM
TCJ3 OPWA
508 SCOTT DRIVE
SCOTT AFB, IL 62225-5357

HQDA (DAMO-FDB)
PENTAGON, RM 3C549
WASHINGTON, DC 20310-0430

HQDA (DALO-SMG)
ATTN: COL AHERN
PENTAGON, RM 1C570
WASHINGTON, DC 20310-0550

HQDA (DASG-HO)
ATTN: LTC CURLING
5109 LEESBURG PIKE
FALLS CHURCH, VA 22041-3258

COMMANDER
U.S. ARMY TRAINING AND DOCTRINE COMMAND
ATTN: ATCD-GB (MR. HASKINS)
FORT MONROE, VA 23651

COMMANDER
U.S. ARMY MATERIEL COMMAND
ATTN: AMCCB (MR. KOGER)
ATTN: AMCCB (MR. HARBS)
5001 EISENHOWER AVE
ALEXANDRIA, VA 22333-0001

COMMANDER
U.S. FORCES KOREA
ATTN: FKJ 3-PL-C
APO AP 96205-0010

COMMANDER
U.S. ARMY PACIFIC COMMAND
ATTN: APOP-NC
APLG-MU
FORT SHAFTER, HI 96858

COMMANDER
U.S. ARMY SOUTH
UNIT 7107
ATTN: SOOP-T
APO AA 34004-5000

U.S. ARMY TEST AND EVALUATION COMMAND
 ATTN: AMSTE-TA-S (CHAN)
 AMSTE-TA-G
 AMSTE-ST
 ABERDEEN PROVING GROUND,
 MD 21005-5055

DIRECTOR
 U.S. ARMY RESEARCH LABORATORY
 ATTN: AMSRL-SL-C
 ABERDEEN PROVING GROUND,
 MD 21005-5001

DIRECTOR
 U.S. ARMY RESEARCH LABORATORY
 HUMAN RESEARCH ENGINEERING DIRECTORATE
 ATTN: AMSRL-HR-MM (D. HARRAH)
 ABERDEEN PROVING GROUND, MD 21005-5001

COMMANDER
 USA SOC
 ATTN: AOOP TRU NBC MAJ WALL
 FORT BRAGG, NC 28307-5204

COMMANDER
 U.S. ARMY EDGEWOOD RESEARCH, DEVELOPMENT
 AND ENGINEERING CENTER
 ATTN: SCBRD-RT
 SCBRD-EN
 ABERDEEN PROVING GROUND,
 MD 21010-5423

HEADQUARTERS
 U.S. ARMY TRANSPORTATION CENTER
 ATTN: ATZF-PTT-N, NBC BRANCH CHIEF
 FORT EUSTIS, VA 20604

COMMANDER
 U.S. ARMY AVIATION CENTER
 ATTN: ATZQ-CDM-S
 FORT RUCKER, AL 36362

COMMANDER
 U.S. ARMY INTELLIGENCE AND THREAT ANALYSIS
 CENTER
 ATTN: IAITAC-RXW
 BLDG 213, WASHINGTON NAVY YARD
 WASHINGTON, DC 20374-5085

COMMANDER
 U.S. ARMY NATICK RESEARCH,
 DEVELOPMENT AND ENGINEERING CENTER
 ATTN: SATNC-AA 5015
 SATNC-IPS (MR. ROLL) (5019)
 SATNC-U (MR. CLOVER)
 SATNC-YSA (DR. ROBERTSON)
 KANSAS STREET
 NATICK, MA 01760-5020

COMMANDER USAJFKSWC
 ATTN: ATSU-CD-CS
 FORT BRAGG, NC 28307-5000

COMMANDER
 U.S. ARMY NUCLEAR AND CHEMICAL AGENCY
 ATTN: MONA-NU (COL FORD)
 MONA-CM (COL SKELLY)
 MONA-ZA (DR DAVIDSON)
 7150 HELLER LOOP SUITE 101
 SPRINGFIELD, VA 22150-3198

COMMANDER
 U.S. ARMY OPERATIONS EVALUATION
 COMMAND
 ATTN: CSTE-ECS (CPT WHITEHURST)
 4501 FORD AVE #780
 ALEXANDRIA, VA 22302-1458

COMMANDER
 U.S. ARMY MEDICAL RESEARCH INSTITUTE
 OF CHEMICAL DEFENSE
 ATTN: SGRD-UV-RO 3100 RICKETS POINT ROAD
 ABERDEEN PROVING GROUND, MD 21010-5425

COMMANDER
 U.S. ARMY MEDICAL RESEARCH INSTITUTE
 OF INFECTIOUS DISEASES
 FORT DETRICK, FREDERICK, MD 21701-5011

COMMANDER
 FIFTH U.S. ARMY
 ATTN: AFKB-TR-UN
 FORT SAM HOUSTON,
 SAN ANTONIO, TX 78234-7000

COMDT USACMLS
 ATTN: ATZN-CM R A (3 Copies)
 5TH AVE BLDG 1081
 ROOM 2024 SIEBERT HALL
 FORT MCCLELLAN, AL 36205-5020

COMMANDANT
 U.S. ARMY FIELD ARTILLERY SCHOOL
 ATTN: ATSF-TA-SS
 FORT SILL, OK 73503-5600

COMMANDER
 U.S. ARMY INFANTRY SCHOOL
 ATTN: ATSH-CDM-F
 ATZB-CDI
 FORT BENNING, GA 31905-5400

COMMANDER
 U.S. ARMY COMBAT SYSTEMS TEST ACTIVITY
 ATTN: STECS-AA-LS
 ABERDEEN PROVING GROUND, MD 21005

COMMANDER
 CHEMICAL BIOLOGICAL DEFENSE AGENCY
 ATTN: AMSCB-BD
 ABERDEEN PROVING GROUND
 MD 21010-5423

COMMANDER
 U.S. ARMY TRAINING AND DOCTRINE COMMAND
 ATTN: ATCD-SL
 FORT MONROE, VA 23651

TEX COM ABNSOTD
CSTE TAB T
FORT BRAGG, NC 28307-0179

HEADQUARTERS
5TH SPECIAL FORCES GROUP (ABN)
ATTN: ASOF-SFA-SC(NBC)
FORT CAMPBELL, KY 42223-6207

HEADQUARTERS
U.S. ARMY ELEMENT, SHAPE
ATTN: CHEMICAL OFFICER
APO AE 09705

COMMANDER
III CORPS AND FORT HOOD
ATTN: AFZF-CML
FORT HOOD, TX 76544-5056

COMMANDER
HQS V CORPS UNIT 29355
ATTN: NBC
APO AE 09014

OFFICE OF THE I CORP CHEMICAL
ATTN: AFZH-CCMS-#09
BOX 339500
FORT LEWIS, WA 98433-9500

COMMANDER,
4ID (M) AND FORT CARSON
ATTN: AFZC-CC
FORT CARSON, CO 80913

COMMANDER
3D INFANTRY DIV (MECHANIZED)
ATTN: AFZF-CW (CHEMICAL OFFICER)
FORT STEWART, GA 31314-5000

COMMANDER, 3D INF DIV
ATTN: AETV-BG-CC, CHEMICAL OFFICER
APO AE 09036

COMMANDER
DIVISION CHEMICAL,
4TH INFANTRY DIV (M)
FORT HOOD, TEXAS 76546-5200

COMMANDER
82D AIRBORNE DIVISION
ATTN: AFVC-CM
FORT BRAGG, NC 28307-5100

COMMANDER, 1ST ARMD DIV
ATTN: AETV-THC-N
CMR 441
APO AE 09111-2108

COMMANDER
101ST AIRBORNE DIV (AASLT)
ATTN: AFZB-PTM-C
FORT CAMPBELL, KY 42223-5000

COMMANDER
2D CML BATTALION
ATTN: CHEMICAL OFFICER
FORT HOOD, TX 76544

COMMANDER
10TH MOUNTAIN DIVISION
ATTN: AFZS-CML
FORT DRUM, NY 13602-5023

COMMANDER
HHC, 2d INFANTRY DIVISION
UNIT # 15041, DIVISION CHEM
APO AP 96258-0289

COMMANDER, 25TH INFANTRY DIVISION (LIGHT)
ATTN: APVG-PT-CM
SCHOFIELD BARRACKS, HI 96857-6005

COMMANDER, 1ST CAVALRY DIVISION
ATTN: AFVA-CML
FORT HOOD, TX 76545-5101

PEASE AIR NATIONAL GUARD BASE
ATTN: SGT ZIELINSKI
157TH CEX
302 NEW MARKET STREET
PEASE, NEW HAMPSHIRE 03803-0157

DET 5 366 TS
BLDG 2781
BLDG 2281
GALLOWAY GATE ROAD
FT MCCLELLAN, AL 36205-5600

COMMANDANT
US ARMY CHEMICAL SCHOOL
ATTN: ATZN CMR A JOINT
DOCTRINE CELL
FORT MCCLELLAN AL 36205-5020

COMMANDER
U.S. ARMY FORCES COMMAND
ATTN: AFOP-TSN
FORT MCPHERSON GA 30330-6000

COMMANDER
TECHNICAL ESCORT UNIT
ATTN MAJ PAUL SCHIELE EXECUTIVE OFFICER
SCBTE CO
ABERDEEN PROVING GROUND MD 21010-5423

COMMANDER
U.S. ARMY AVIATION CENTER
ATTN: ATZQ-BDE-O (COB)
FORT RUCKER, AL 36362

COMMANDER
ATTN AFZA GT N (F 3/NBC)
XVIII AIRBORNE CORPS
FORT BRAGG, NC 28307-5000

FISHER LIBRARY
US ARMY CHEMICAL SCHOOL
FT MCCLELLAN, AL 36205-5020

HQ 497 1G/1NOT
5113 LEESBURG PIKE, SUITE 600
FALLS CHURCH, VA 22041-3230

HQ AIA/CEP
ATTN: TECH SGT DEYO 68IS
SAN ANTONIO, TX 78243-5000

LOGISTIC SUPPORT ACTIVITY
ATTN: AMXLS-AE (SUSAN RUHLMAN)
REDSTONE ARSENAL, AL 35898-7466

PROGRAM MANAGER
ARMORED SYSTEMS INTEGRATION
ATTN SFAE ASM AS LTC DELLA SILVA
WARREN MI 48397-5000

U.S. ARMY MEDICAL RESEARCH AND
MATERIAL COMMAND
ATTN: SGRD-PLD
FORT DETRICK, FREDERICK, MD 21702-5012

CBIAC
ATTN: BARBARA HOFFMAN
P.O. BOX 196
GUNPOWDER BRANCH APG, MD 21010-0196

HQ USAFE/CEX
UNIT 3050, BOX 10
APO AE 09094-5001

HQ PACAF/CEOO
25 E ST, SUITE D306
HICKHAM AFB, HI 96853-5412

HQ AFIS/INKTC
WASHINGTON, DC 20330-5110

HQDA AMC/CEOO
507 A STREET
SCOTT AFB, IL 62225-5022

HQ ACC/CEXO
129 ANDREWS STREET, STE 102
LANGLEY AFB, VA 23665-2729

HQ AFRES/CEXP
155 2ND STREET
ROBINS AFB, GA 31098-1635

HQ AFMC/CEOO
4225 LOGISTICS AVE, SUITE 7
WRIGHT-PATTERSON AFB, OH 45433-5746

HQ AFSOC/CEX
100 BARTLEY STREET, SUITE 218E
HURLBURT FIELD FL 32544-5273

HQ ALASKAN NORAD REGION
ATTN: ANR/DOYN
ELMENDORF AFB, AK 99506-5000

ANGRC/CEOE
3500 FETCHET AVENUE
ANDREWS AFB MD 20331-5157

HQ AETC/CEO
266 F STREET WEST
RANDOLPH AFB, TX 78150-4321

USAFAWC
28/TS TXCO
203 W. D AVE, SUITE 400
EGLIN AFB, FL 32542-6867

ASC/YOX
102 WEST D AVENUE, SUITE 300
EGLIN AFB, FL 32542-6808

HQ AFCESA/DX
139 BARNES DR.
TYNDALL AFB, FL 32403-5319

HSC/YAC
2701 WEST ROAD
BROOKS AFB, TX 78235-5000

HSC/IN
8104 CHENNAULT RD
BROOKS AFB, TX 78235-5317

HQ AMC/XPQS
402 SCOTT DR., UNIT 3L3
SCOTT AFB, ILL 62225-5307

HQ AFCECEX
139 BARNES DRIVE SUITE 1
TYNDALL AFB, FL 32403-5319

149 CES/CEX
ATTN: SMSGT TERRY MACHGAN
1413 BILLY MITCHELL ROAD
KELLY AFB TX 78241-5538

22 CES/CEX (2COPIES)
52942 HUTCHINSON CT., BLDG 683
MCCONNELL AFB, KS 67221-3619

AL/CFDE
ATTN: DR. CLYDE R. REPLOGLE
2245 MORAHAN WAY BLDG. 29
WRIGHT PATTERSON, AFB, OH 4533-7008

HQ AFSPC/CEPX
150 VANDERBERG ST
SUITE 1105
PETERSON AFB, CO 80914-4150

DR. NGAI WONG
AMSCB-AL (USAF AL/CFDB) BLDG E3234
ABERDEEN PROVING GROUND, MD 21010-5423

HQ NAIC/TATH
4180 WATSON WAY
ATTN: MARK EIMER
WRIGHT PATTERSON AFB, OH 45433-5648

HQ NORAD/J30B
125 S. PETERSON BLDG, STE 116
PETERSON AFB, CO 80914-3260

SAF/AQP
CAPTAIN WES MARCHESSEAU
1060 AIR FORCE PENTAGON
WASHINGTON, D.C. 20330-1060

HEADQUARTERS
AFSOC/CEX
100 BARTLEY STREET, SUTIE 218-E
ATTN: MR. TOM GRAHAM
HULBERT AFB, FL 32544-5273

HQ USCENCOM
CCJ3-OG
ATTN: MAJ RAY VAN PELT
MACDILL AFB, FL 33594

COMMANDER NAVAL AIR FORCE
U.S. PACIFIC FLEET
BOX 357051
SAN DIEGO, CA 92135-7051

COMMANDER, NAVAL SURFACE FORCE
U.S. PACIFIC FLEET (ATTN: N66)
NAVAL AMPHIBIOUS BASE, CORONADO
SAN DIEGO, CA 92155-5035

COMMANDER SEVENTH FLEET
FPO AP 96601

COMMANDER THIRD FLEET
FPO AP 96601-6001

COMMANDER TRAINING COMMAND
U.S. PACIFIC FLEET
SAN DIEGO, CA 92147

COMMANDER TRAINING COMMAND
U.S. ATLANTIC FLEET
ATTN: N32
NORFOLK, VA 23511

COMMANDER
U.S. ATLANTIC FLEET (N7)
1562 MITSCHER AVE, SUITE 250
NORFOLK, VA 23551-2487

DEPARTMENT OF THE NAVY
FLEET TRAINING GROUP
DETACHMENT NORFOLK
1310 8TH ST.
NORFOLK, VA. 23521-5150

COMMANDER NAVAL SURFACE FORCE
US ATLANTIC FLEET N541A
1430 MITSCHER AVE
NORFOLK, VA 23551-2494

COMMANDER
NAVAL SEA SYSTEMS COMMAND
ATTN: (MR S. ENATSKY)
SEA 0566 (MR P. JUNG)
2531 JEFFERSON DAVIS HWY
WASHINGTON, DC 22242-5160

COMMANDER
NAVAL SPECIAL WARFARE COMMAND
2000 TRIDENT WAY
SAN DIEGO, CA 92155-5000

NAVAL SURFACE WARFARE CENTER
CODE B-50 (MR. J. HORTON)
CODE B-53 (MR. BYRNE)
CODE B-51 (MR. YENCHA)
CODE B-53 (MR. POMPEII)
DAHLGREN, VA 22448-5000

COMMANDING OFFICER
NAVAL TRAINING SYSTEMS CENTER
CODE 4972 (T. FRANZ)
12350 RESEARCH PARKWAY
ORLANDO, FL 32826-3224

DIRECTOR, ONI
ATTN: ONI 2323
4251 SUITLAND ROAD
WASHINGTON D.C. 20395-5720

COMMANDER
NAVAL HEALTH RESEARCH CENTER
ATTN: DR ROBERT PAZOS
BOX 85122
SAN DIEGO CA 92138

OFFICER IN CHARGE
NAVAL RESEARCH LAB DETACHMENT
CBD COM
ABERDEEN PROVING GROUND, MD 21010-5323

BUREAU OF MEDICINE AND SURGERY
ATTN: MED-OZC
2300 E STREET, NW
WASHINGTON, DC 20372-5300

COMMANDING OFFICER
NAVAL RESEARCH LABORATORY
CODE 6116 R A LAMONTAGNE
WASHINGTON, DC 20375-5320

NAVAL AIR WARFARE CENTER-AIRCRAFT DIVISION
ATTN: GAITHER M PUGH 4.1.8
UNIT 5 BLDG 2187 SUITE 1180
48110 SHAW ROAD
PATUXENT RIVER MD 20670-1906

SURFACE WARFARE DIVISION
ATTN: CODE N862, RM 4D537
WASHINGTON, D.C. 20350-2000

UTC (SCW) ECKHOFF
5510 CBC 8TH STREET
GULFPORT, MS 39501-5003

COMMANDANT
U.S. MARINE CORPS
ATTN: APW R-P
WASHINGTON, DC 20380

COMMANDING OFFICER
MARINE AIRCRAFT GROUP 31 (S-3/NBC)
2D MARINE AIRCRAFT WING, FMF, ATLANTIC
BEAUFORT, SC 29904-6120

COMMANDING OFFICER
MARINE AIR CONTROL GROUP 28 (S-3/NBC)
2D MARINE AIRCRAFT WING, FMF ATLANTIC
P.O. BOX 8069
CHERRY POINT, NC 28533

COMMANDING OFFICER
MARINE WING SUPPORT GROUP 27 (S-3/NBC)
2D MARINE AIRCRAFT WING, FMF ATLANTIC
CHERRY POINT, NC 28533

COMMANDING OFFICER
MARINE AIR WING HEADQUARTERS
SQUADRON 2 (S-3/NBC)
2D MARINE AIRCRAFT WING, FMF, ATLANTIC
CHERRY POINT, NC 28533

COMMANDING GENERAL
MARINE CORPS COMBAT DEVELOPMENT COMMAND
ATTN: (CWO TURVILLE) C 443
2042 BROADWAY ST, SUITE 17
QUANTICO, VA 22134-5021

COMMANDING GENERAL
FLEET MARINE FORCES PACIFIC
ATTN: G3/NBC
CAMP H.M. SMITH, HI 96861

COMMANDING GENERAL
FLEET MARINE FORCES ATLANTIC
ATTN: G3/NBC
1468 INGRAM STREET
NORFOLK, VA 23551-2596

USMC LIAISON OFFICER TO TECOM
ATTN: AMSTE-ML
ABERDEEN PROVING GROUND, MD 21005

COMMANDER
MARCORSYSCOM
ATTN: AW
2033 BARNETT AVENUE, SUITE 315
QUANTICO, VA 22134-5010

COMMANDING GENERAL
II MARINE EXPEDITIONARY FORCE
ATTN: G-3/NBC, PSC BOX 20080
CAMP LE JEUNE, NC 28542-5401

COMMANDING GENERAL
2D MARINE DIV FMF
PSC BOX 20003
CAMP LE JEUNE, NC 28540

COMMANDING OFFICER
MARINE WING SUPPORT SQUADRON 271 (S-3/NBC)
2D MARINE AIRCRAFT WING, FMF, ATLANTIC
MCAS CHERRY POINT, NC 28533

COMMANDING OFFICER
MARINE WING SUPPORT SQUADRON 274 (S-3/NBC)
2D MARINE AIRCRAFT WING, FMF, ATLANTIC
MCAS CHERRY POINT, NC 28533

COMMANDING OFFICER
MARINE WING SUPPORT SQUADRON 273 (S-3/NBC)
2D MARINE AIRCRAFT WING, FMF, ATLANTIC
MCAS BEAUFORT, SC 29904-6035

COMMANDING OFFICER
HQ, MAG-26, (NBC)
PSC BOX 21010
JACKSONVILLE, NC 28545-1010

COMMANDING GENERAL
ATTN NBC DEFENSE OFFICER
III MARINE EXPEDITIONARY ORCE
UNIT 35601
FPO AP 96606-5601

COMMANDING OFFICER
31ST MARINE EXPEDITIONARY UNIT FMF
ATTN NBCO CW03 TERRY MURPHY
UNIT 35621
FPO AP 96606-5621

UNITED STATES MARINE CORPS
2ND MARINE AIRCRAFT WING (G3/NBC)
U.S. MARINE CORPS FORCES, ATLANTIC
POSTAL SERVICES BOX 8050
CHERRY POINT, NC 28533-0050

UNITED STATES MARINE CORPS
MARFORLANT NBC
CAMP LEJEUNE, NC 28542-5701

NBC OFFICER
MWHS-1 1ST MAW
UNIT 37121 (G-3/NBC)
FPO AP 96603-7121

ADMINISTRATOR, DEFENSE TECHNICAL
INFORMATION CENTER (2 copies)
CAMERON STATION
8725 JOHN J. KINGMAN RD SUITE 0944
FORT BELVOIR, VA 22060-6218

DIRECTOR
CENTERS FOR DISEASE CONTROL
ATTN: LOGGING CONTROL OFFICER - 1/B413
(for ASST DIR, EDWIN K. GRAY)
ATLANTA, GA 30333